ABSTRACT

Title of Dissertation:	REACTION MECHANISMS AND INTERFACE CHARACTERISTICS OF ELECTRODE AND ELECTROLYTE MATERIALS FOR MAGNESIUM BATTERIES
	Emily Sahadeo, Doctor of Philosophy, 2020
Dissertation directed by:	Professor Sang Bok Lee, Department of Chemistry and Biochemistry

Rechargeable magnesium (Mg) batteries are an emerging electrical energy storage technology proposed as an alternative to current Lithium-ion (Li-ion) batteries. Mg batteries have the potential to provide more energy than current Li-ion systems due to the high volumetric capacity and low reduction potential of Mg metal, in addition to higher abundance and cheaper cost of Mg compared to Li metal. However, there are many challenges regarding Mg battery chemistry and materials that must be resolved before they can be successfully commercialized. The work in this dissertation addresses a few of these challenges, including poor Mg^{2+} diffusion in MnO_2 cathodes, interfacial limitations at the Mg anode and MnO_2 cathode surfaces, and the development of solid-state electrolytes as an alternative to liquid electrolytes that passivate the Mg anode interface. These issues are investigated from a fundamental chemical and electrochemical standpoint to help improve future design of rechargeable Mg batteries.

In the first study, the electrochemical reactions and charge storage mechanism of electrodeposited MnO_2 cathodes in water-containing organic electrolyte are

explored using X-ray photoelectron spectroscopy. These results demonstrate the key role that water plays in enabling the reversible insertion/extraction of Mg^{2+} from the MnO_2. Second, a heterogeneous electrode structure, PEDOT/MnO_2 coaxial nanowires, is utilized to study the effect of conductive polymer surface layers on the MnO_2, specifically regarding the effect on the cathode's cyclability and power performance as well as the overall charge storage mechanism. Additionally, to investigate the potential for anode protection on Mg metal, ALD Al_2O_3 is deposited on different Mg metal substrates to determine whether it can improve Mg deposition and stripping at the Mg anode and prevent electrolyte degradation on the Mg surface. While it does not demonstrate the ability to effectively protect the anode during cycling, the results herein can help inform further protection layer development. Finally, the catalytic ability of Mg^{2+} salts is reported for the ring-opening polymerization of 1,3-dioxolane, moving toward exploring this polymer's potential to be utilized as a solid-state electrolyte. The findings here give fundamental insights into materials' properties that can be further utilized to design Mg batteries with high-voltage cathodes.

REACTION MECHANISMS AND INTERFACE CHARACTERISTICS OF ELECTRODE AND ELECTROLYTE MATERIALS FOR MAGNESIUM BATTERIES

by

Emily Sahadeo

Dissertation submitted to the Faculty of the Graduate School of the
University of Maryland, College Park, in partial fulfillment
of the requirements for the degree of
Doctor of Philosophy
2020

Advisory Committee:
Professor Sang Bok Lee, Chair
Professor Neil Blough
Professor Leah Dodson
Professor Gary Rubloff
Professor Yuhuang Wang

Dedication

To Mom and Olivia.

Acknowledgements

I would like to first and foremost thank my advisor, Sang Bok Lee. He has been an amazing mentor throughout this graduate school experience, not only due to his expansive knowledge of electrochemistry and beyond, but also because of his support for every opportunity that I have tried to take advantage of during my Ph.D., even those that have taken me outside of the lab. I would also like to thank my committee, Prof. Neil Blough, Prof. Yuhuang Wang, and Prof. Gary Rubloff for their support throughout the years and for their time, and special thanks to Prof. Leah Dodson for agreeing to be on my committee on short notice.

I am also immensely grateful to all my lab mates in the Lee group, both past and present. Nam, you taught us all everything we needed to get started in lab, and I would not have been successful without your friendship and openness to discussing projects and results at any time. Hakeem, you have been a great partner in our foray into Magnesium batteries and all the challenges that come with it. Yang, you have been a great collaborator on whom I could always rely for interesting conversation related to research or not. Darrin, your insightful questions always kept me on my toes, and I was glad to have another coffee-dependent companion.

To Prof. Gary Rubloff and his group I also owe immense thanks. Their incredible knowledge in ALD and discussions in group meetings have been incredibly instrumental in my development as a scientist. I am especially thankful to Dr. Chuan-fu Lin and his advice on all things related to anode interfaces and his willingness to help me navigate the Mg anode challenges. I would also like to thank Dr. Alex Kozen and Dr. David Stewart for their willingness to help me XPS. Dr. Keith Gregorczyk and

Dr. Angelique Jarry have also been incredible sources of support, and I am thankful for their many chats related to job searches and advice for the future.

I would not have been able to complete half of my research without the guidance and experience of some of the facility and Nanocenter staff. Dr. Karen Gaskell was an incredible help in learning XPS and was always open to questions on all things surface-science. Dr. Sz-Chian Liou has been an immense support in microscopy, helping with all the TEM for my final project and deciphering small issues with the SEM whenever they would crop up. I have also had the best teaching experience in working with Natalia White in the Instrumental Methods of Analysis lab, and I learned a great deal from her about teaching and managing a lab class.

I lastly would like to acknowledge my incredible friends and family. I would not have made it this far in my PhD without the support of my classmates in the graduate program. Sarah, Leila, and Sam this experience would not have been the same without you and your support. Our friendship is one of the best things I will take with me from this whole journey. Zoey, I am incredibly thankful the EFRC brought us together, and I am grateful to you for always being there to talk or go on Vigilante coffee breaks. Ellie, Megan, Ali, Shannon, and Jocelyn, thank you for making me take time off to get out of lab and socialize and for always being there. Trisha, it was great to have someone able to relate to me while finishing my dissertation and talk about everything going on at the end of this process.

Most of all, I came to UMD to be close to my family so I could be of help to them, but they have also been the best support and source of encouragement. To my mom, dad, and stepdad, thank you for always being there for me (especially for the

dinner invites, after which the whole fridge ended up going home with me and Olivia). To my sister, Olivia, thank you for living with me for all 6 years of my PhD, providing comradery and sanity, making sure I ate real food instead of junk, and generally being my best friend. I would not be here without you.

Table of Contents

List of Tables

List of Figures

List of Abbreviations

AAO – Anodized aluminum oxide
ACC - Activated carbon cloth
CA - Chronoamperometry
CV - Cyclic voltammetry (voltammogram)
EDS – Energy-dispersive X-ray spectroscopy
GV – Galvanostatic cycling
ICP-AES – Inductively-coupled plasma atomic emission spectroscopy
LCO – Lithium cobalt oxide
MnO_2 – Manganese dioxide
NW – Nanowire
OTf - Triflate
PEDOT – Poly(3,4-ethylenedioxythiophene)
PC – Propylene carbonate
RMB – Rechargeable magnesium battery
SEI – Solid electrolyte interphase
SEM – Scanning electron microscopy
TEM – Transmission electron microscopy
TFSI – Bis(trifluoromethanesulfonylimide)
XPS – X-ray Photoelectron Spectroscopy

Chapter 1: Understanding Challenges for Cathodes and Anodes in Rechargeable Magnesium Batteries

Parts of this chapter in Section 1.4 were published in Wang, Y., Sahadeo, E. et al., High-capacity lithium sulfur battery and beyond: a review of metal anode protection layers and perspective of solid-state electrolytes. *J. Mater. Sci.* ***2018****, 54, 3671-3693, reprinted by permission from Springer Nature Customer Service Centre GmbH.*

1.1. Introduction to Rechargeable Mg batteries

Finding ways to efficiently store and provide energy is critically important in a multitude of parts of everyday life. Whether it is in large scale grid storage for intermittent renewable sources or small scale rechargeable batteries, electrochemical technologies are a versatile way to store energy. The most ubiquitous and well-studied electrochemical energy storage technology today is the Lithium-ion (Li-ion) battery. Most widely composed of a layered graphite anode[1] and metal oxide cathode (typically layered $LiCoO_2$)[2] with a liquid electrolyte, Li-ion batteries are the most commercialized system in use today. However, the amount of energy that can be stored is limited and will soon reach the maximum energy density that can be stored based on the chosen materials.[3] As demand for low cost and energy dense technologies is on the rise, different systems are being investigated to replace Li-ion. Some of these include chemistries based on Li^+ but with different anode or cathode materials, such as Li metal systems, lithium-sulfur, and lithium-oxygen. Other chemistries proposed for replacing Li^+ include sodium, aluminum, zinc, calcium, and magnesium based rechargeable batteries.[4]

Among the several energy storage systems being investigated as alternatives to current Li-ion technology, rechargeable Mg batteries (RMB) have sparked interest because Mg is a more abundant element than Li and with the right electrolytes it does not form harmful dendrites which are an issue for Li metal anodes.[5] It has a low reduction potential (-2.37 V vs. SHE), and although it is not as low as Li (-3.04 V vs. SHE) the higher potential compared to Li means it is less reactive, a positive regarding safety concerns. Additionally, Mg metal has a larger volumetric capacity (3,832 mAh/cm^3) compared to Li metal (2,054 mAh/cm^3) and graphite (777 mAh/cm^3). Another advantage for Mg batteries is that for one cation that is inserted, there is a potential for a two-electron transfer, whereas two Li^+ ions need to insert to compensate for the storage of two electrons. Despite these many positives, there are challenges in all parts of the RMB that need to be addressed. Some issues that will be discussed in this dissertation include poor Mg^{2+} insertion kinetics into metal oxide cathode materials and passivation of the Mg metal anode in non-compatible electrolytes, addressed in detail in Sections 1.4 and 1.5. To better understand the advantages of RMB, the fundamental principles for understanding battery chemistry will be further elucidated in the next section.

1.2. Metrics for battery performance

There are many metrics used to quantify the performance of batteries and help identify the best systems. Foremost are the energy and power density – how much energy can be stored, and how fast can that energy be delivered for the desired application. Before investigating a battery chemistry, it is important to perform initial

calculations based on theoretical values to determine the battery's threshold for storing energy. One of the fundamental theoretical values that can be calculated for both cathodes and anodes is the theoretical capacity, either gravimetric or volumetric. Equation 1.1 is used to calculate the theoretical specific capacity, where *n* is the number of electrons transferred per mole of material, *F* is the Faraday constant, and *M* is the molecular weight of the active material.

$$C_{spec} = \frac{nF}{M} \qquad \text{Equation 1.1}$$

The calculation for the energy density is shown in Equation 1.2, where V_{cell} is the cell voltage and q is the charge (Ah), also referred to as the capacity. This energy is then reported as specific (Wh/g) or a volumetric energy density (Wh/L) when normalized to the battery's mass or volume, respectively.

$$Energy = V_{cell} \times q \qquad \text{Equation 1.2}$$

The cell voltage is determined by the difference in potential between the anode and cathode materials. This metric is why the potentials for the electrodes is critical – in moving from Li to Mg, there is an increase in the reduction potential of ~0.7 V. This inherently gives RMB a disadvantage regarding the voltage window. For instance, if two batteries have the same cathode material, and one has a Mg anode and the other has a Li anode, the battery with Mg will have an overall smaller cell voltage. However, this loss can be compensated for by choosing cathode materials with sufficiently high capacities. The power of a system in units of Watts (W) is calculated using Equation 1.3, where i is the current.

$$Power = i \times V_{cell} \qquad \text{Equation 1.3}$$

As mentioned previously, the power describes how fast a battery can be charged and discharged due to its dependence on the current. When assessing batteries, power performance evaluations at varied current densities is usually coupled with testing the cycle life or cyclability of the battery. Cyclability tests the battery over a long period and large number of charge/discharge cycles to see how long the battery can be cycled without losing capacity. The above mentioned calculations will be used throughout this dissertation to convey the properties and performance of different electrode configurations and battery systems.

1.3. Materials for Magnesium batteries

There are three main components of rechargeable batteries – two electrodes, the anode and the cathode, and the electrolyte which isolates them from one another. Regardless of the electrode or electrolyte materials chosen, the underlying electrochemical processes at each electrode during charge and discharge can be described in a similar manner. The convention for batteries is that the cathode is the electrode which undergoes reduction accompanied by cation movement into the electrode (either via insertion or conversion, further discussed in the next section) when the battery is used to provide energy, or discharged. The discharge process is demonstrated by the red arrows in Figure 1.1. The anode is the electrode which undergoes oxidation upon discharge, and releases cations into the electrolyte. The discharge process causes electrons to flow through the external circuit to provide usable energy, while ions migrate from the anode to the cathode. The opposite process, charging, requires that external current be applied to reverse the reactions,

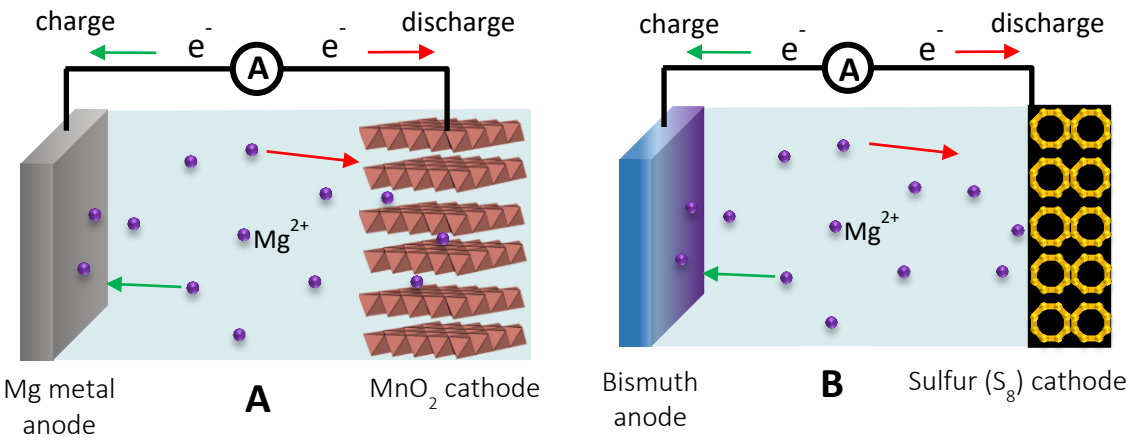

Figure 1.1 Different battery configurations demonstrating the 4 major types of electrodes, a) metal anode paired with metal oxide intercalation cathode and b) alloying anode paired with a sulfur conversion cathode. The blue colored space separating the electrodes represents the electrolyte.

demonstrated by the green arrows in Figure 1.1. In the following sections, the four major types of cathode and anode materials, as well as important characteristics of each, will be discussed.

1.3.1. Cathodes

A variety of battery materials exist which can be utilized as cathodes and anodes, each with a different type of electrochemical reaction that provides energy. The first group of materials widely utilized in energy storage are intercalation materials. The most well know Li-ion battery, graphite and $LiCoO_2$, contains intercalation materials as both the cathode and anode. Graphite and LCO are both layered materials, but other compounds, including metal oxides and sulfides, can also be composed of tunnel structures where the cations are able to insert in open sites within the crystal lattice.[6] The electrochemical oxidation and reduction reactions occur at the metal centers of the compounds, such as Co in LCO, and the Li^+ (or Mg^{2+} in the case of RMB)

ions are retracted or inserted depending on the reaction occurring at the electrode to maintain charge neutrality. Common intercalation materials of interest for Mg battery chemistries, particularly metal oxides, will be discussed more thoroughly in Section 1.5. Further, the most relevant material for this dissertation, MnO_2, will be addressed in detail in Section 2.1.

Another important reaction utilized in battery systems are conversion reactions. Different than intercalation electrode materials, these reactions involve a chemical conversion upon the elemental cathode material's reaction with the ion in solution. Prominent conversion materials include sulfur[7, 8] and oxygen,[9] while halides such as bromine[10] and iodine[11] have also been studied as potential materials to utilize in RMBs. An example of the solid-state cathode reduction reaction for Mg-S batteries is in Equation 1.4, demonstrating the reduction of sulfur and subsequent reaction with Mg^{2+} to form a new product. This chemical equation is a simplified description of the reaction occurring at the S cathode upon a full two-electron transfer reaction, as the exact electrochemical reaction mechanism and species formed during the reaction is currently a significant focus in the Mg-S battery community.[8] The mechanism is suggested to be a complex combination of the solid-state mechanism in Equation 1.4 and a multi-step solution-mediated mechanism involving dissolved Mg polysulfide species in the electrolyte.[12-15]

$$Mg^{2+} + \frac{1}{8}S_8 + 2e^- \rightarrow MgS \qquad \text{Equation 1.4}$$

Conversion cathodes are favorable for RMBs due to their high theoretical specific capacity, which for a sulfur cathode is 1672 mAh/g.[3] Although the voltage for this chemistry is limited, a theoretical voltage of 1.77 V vs. Mg which in experiments

is generally lower, the theoretical energy densities for this chemistry are 1700 Wh/kg and 3200 Wh/L.[3] Despite the high theoretical energy density values, there are a few critical issues for sulfur battery systems. One such problem is polysulfide dissolution into the electrolyte, which can cause material loss at the cathode and thus capacity loss as well as degradation products formed at the Mg metal anode.[16] Additionally, the electronically insulating nature of sulfur means it must be paired with an electronically conductive scaffold, traditionally an activated carbon material, to provide electronic pathways, which adds material weight that does not significantly contribute to the capacity of the cathode. While solutions to these problems are under investigation, intercalation materials are a favorable choice due their higher voltage and intrinsically higher electronic conductivity.

1.3.2. Anodes

While insertion materials can also be anodes, such as graphite, charge storage reactions at the anode beyond insertion predominantly involve metals that form alloys upon ion insertion and pure metal electrodes for the chemistry of interest, such as Li or Mg metal. The metals that have been most consistently studied as alloy anodes in the literature for RMB are bismuth[17-19] and tin,[20-22] as well as mixed phases of these materials[23, 24] and others,[25] while computational studies have looked into the possibility of using germanium and silicon.[26] These alloy anodes are attractive because they still have a relatively low potential vs. Mg (measured ~0.15 V for Sn, ~0.23 V for Bi),[27] which means there will not be a significant sacrifice in the voltage of the battery. Further, these metals are more stable in conventional electrolytes and therefore

passivation layers do not hinder Mg^{2+} insertion, which is major problem for Mg metal electrodes. These alloying materials also have the potential to contribute high capacities, with tin and bismuth having theoretical capacities of 903 mAh/g and 385 mAh/g, respectively, although they are less than the theoretical specific capacity of Mg metal, which is 2206 mAh/g. Another drawback of these anodes is that they can have a significant volume change upon Mg^{2+} insertion,[26] which means their cyclability is very low due to significant breakdown of these anodes over time. Additionally, Mg^{2+} still needs to intercalate into the metal structure for the alloy to form, which also can be plagued by slow insertion kinetics of Mg^{2+}. These drawbacks are why most researchers are still focusing on finding ways to utilize Mg metal anodes.

Mg metal anodes are the most promising anode for RMB, with high theoretical specific (2206 mAh/g) and volumetric capacities (3833 mAh/g), and they are not hindered by slow Mg^{2+} insertion kinetics. The redox reactions that occur at the Mg metal anode are simply the oxidation of Mg metal to Mg^{2+} upon discharging, called Mg dissolution or stripping. Upon charging of the battery, Mg^{2+} ions migrate from the cathode to the Mg anode where they are reduced back to Mg metal, referred to as Mg deposition. Mg metal is also well-known to deposit in non-dendritic morphologies,[28-31] though a few recently published papers have demonstrated Mg may have the capability to form dendrites under certain conditions.[32, 33] However, Mg largely deposits in a non-dendritic manner which is a major advantage over Li metal anodes, which are notorious for the formation of dangerous Li-metal dendrites.[5] Dendrites are hazardous because they can grow from the anode through the separator and electrolyte and make contact with the cathode, shorting the battery.

The most critical issue for Mg metal anodes is that they are easily passivated through reactions with conventional electrolytes[34, 35] and contaminants such as water.[36] The term "passivation layer" is most commonly used regarding these layers formed on the Mg anode interface because it is different from the solid electrolyte interphase, or SEI, which forms in Li metal anodes due to the fact that Mg^{2+} ions cannot diffuse through this layer to be oxidized or reduced at the Mg metal surface. These passivation layers inhibit the electrochemistry on the anode side, whereas the SEI in Li-ion batteries is not passivating because Li^{+} ions can move through the SEI layer and electrochemical reactions can still occur. This issue will be discussed further in Section 1.4 and Chapter 4, which will discuss possible solutions for passivation.

The electrodes discussed are only 4 types of materials, though others exist such as organic molecule based cathodes and anodes,[37-39] and new materials are synthesized and investigated all the time. The work in this dissertation will include studies specifically focused on the insertion-based material MnO_2 as well as Mg metal anodes. While the electrodes are critical for battery performance, the last part of this chapter will briefly address the final part of the battery, the electrolyte solution.

1.3.3. Mg electrolytes

As discussed in the previous section, the passivation layer that forms on Mg metal when using conventional carbonate electrolytes is a layer through which Mg ions cannot pass, thus no electrochemical reactions occur after it forms. Due to this issue, research has focused on developing new electrolytes to circumvent the issue of a passivation layer forming on Mg metal anodes.[14, 40] This research has been successful

in the development of electrolytes and complex Mg salts that can be paired with a Mg metal anode, however their synthesis is often time-consuming.[4] The field of electrolyte development for RMB has been prolific, and a detailed history and analysis of these discoveries is beyond the scope of this dissertation. However, we have published a perspective paper on this topic,[41] and a brief overview of the important issues and properties related to electrolytes and some recent findings will be included here.

For RMB, there are different properties and metrics that are used to characterize the effectiveness and utility of an electrolyte. The first thing an electrolyte must be able to do is reversibly deposit and strip Mg metal with a high coulombic efficiency. Coulombic efficiency is the ratio of charge stripped during oxidation to charge deposited during reduction to Mg metal, shown in Equation 1.5. This metric is a measure of the reversibility of the deposition and stripping reactions. Low coulombic efficiency indicates that not all the Mg being deposited can be removed, which is often an indicator that passivation or some other process is hindering the reaction. High coulombic efficiency is a good indicator that an electrolyte is compatible with the Mg metal interface.

$$\mathrm{CE} = \frac{\text{charge stripped}}{\text{charge deposited}} \text{ X } 100\% \qquad \text{Equation 1.5}$$

Another important property for electrolytes is their oxidative or anodic stability. The anodic stability determines the upper end of the voltage limit of the electrolyte before it begins to oxidatively degrade at the cathode surface. This upper voltage limit determines what cathodes can be utilized with different electrolytes. Recently synthesized electrolytes generally have a low anodic stability window, < 3 V vs.

Mg/Mg^{2+}, which is below what is needed for most high voltage cathodes (3 V or greater).[41] While anodic stability influences what cathodes can be used, so does the reactivity of the electrolyte salts themselves. Many of the state-of-the-art electrolytes are nucleophilic, which is an issue for cathodes such as sulfur which is electrophilic, meaning the electrolyte would react with the cathode instead of the electrochemical reactions needed for energy storage.

Recently, many studies of electrolytes have focused on Mg salts containing weakly coordinating anions, hoping to decrease the reactivity of the anions in the electrolyte at the Mg anode surface. It was demonstrated by some computational work that some contact ion pairs, such as $[MgTFSI]^+$ have decreased reductive stability which enables degradation on the anode interface.[42] By decreasing the ion pair ability, the goal is to increase the reductive stability of the anion. Further, many of these electrolytes have demonstrated higher oxidative stability, including carborane anions, such as $Mg(CB_{11}H_{12})_2$[43, 44] and $Mg(CB_9H_{10})_2$,[45] and fluorinated alkoxyaluminates.[46, 47] Another promising discovery is that electrolyte additives have improved reversibility and coulombic efficiency in some well-studied systems such as Magnesium aluminum chloride complex (MACC)[48] and $Mg(TFSI)_2/MgCl_2$.[49] While these properties are great strides forward, many of them have not been demonstrated with high voltage cathodes, due in part to a lack of sufficient materials with good Mg^{2+} insertion kinetics.

One of the goals of this dissertation is to work towards finding a route to utilize a high voltage cathode in a RMB with a conventional electrolyte through the use of creative strategies to increase Mg^{2+} insertion, the focus of Chapters 2 and 3. This approach would bypass the need for complex electrolytes, but would then require a

different solution for the incompatibility of conventional carbonate solvents and simple Mg salts with the Mg anode, discussed in Chapter 4. An alternate strategy to completely remove the incompatibilities of liquid electrolytes is to move to a solid-state electrolyte system, which will be further elucidated in Chapter 5. In order to understand the possibility for utilizing electrolytes that are not completely compatible with the Mg anode, meaning they traditionally form passivation layers, it is important to analyze the current knowledge of the Mg anode interface in conjunction with the different available electrolytes present in the literature.

1.4. Progress in Understanding the Mg Metal Interface

With conventional electrolytes that contain carbonate or acetonitrile solvents with simple salts such as $Mg(ClO_4)_2$, these components are easily reduced on the Mg anode surface which forms a passivating film that blocks Mg deposition and dissolution.[34] Upon this discovery, the focus of much research became the synthesis of electrolytes that did not degrade on the Mg anode surface because it was believed Mg needed to be pristine for reversible deposition and stripping. However, over the past few years electrolytes such as those based on $Mg(TFSI)_2$ and $Mg(BH_4)_2$ in ether solvents have demonstrated reversible electrochemistry at the Mg anode with some degree of electrolyte degradation on the Mg surface, although the overpotentials for Mg deposition and stripping are much higher than compatible electrolytes.[50-53] These observations draw attention to the importance of understanding the types of different interfacial phenomena that may be occurring and discerning what properties make a layer truly passivating. Other interface layers may act similar to an SEI layer that does

not block Mg^{2+} ions, and layers of adsorbed species have been observed that are removed from the surface under a bias.[54]

Multiple studies have demonstrated the sensitivity of Mg interfaces to trace impurities, especially water. Water can create MgO and $Mg(OH)_2$ compounds at the Mg surface.[36] Additionally, water can alter the intrinsic solvation of Mg with the anions in the electrolyte or disturb the distributions of ions in the double layer formed at the Mg surface.[55] Water can also enable both solvent and salt decomposition by introducing OH^- species which can act as a nucleophile, and in one study OH- was shown to attack both diglyme and the $[MgTFSI]^+$ contact ion pair.[56] It has been demonstrated that Cl^- can help prevent some level of Mg anode surface passivation, but Cl corrodes common cell components such as stainless steel, which make electrolytes containing chloride less than ideal.[36, 57, 58] Specifically regarding Mg-S batteries, reports of chemistries using HMDS-Cl and $Mg(TFSI)_2$/DME electrolytes have demonstrated the feasibility of the system despite a visible presence of reduced sulfur and other species on the magnesium anode.[13, 59] The ability of Mg to deposit and strip reversibly and for Mg-S batteries to function even with SEI layers on the surface gives promise to the idea of protection layers, and indicates that a completely pristine Mg surface may not be necessary for Mg batteries. These results provide evidence that if a layer with favorable properties for Mg diffusion, and therefore deposition and stripping, is present at the Mg anode interface then purposeful surface engineering of the Mg anode may be possible with an artificial SEI layer or protection layer.

1.4.1. Prospects for Protection in Mg batteries

Not only have studies of the Mg interface indicated promise for Mg protection efforts, but there have also been a few studies demonstrating the success of ion-conducting layers at the Mg surface. It has been demonstrated that by adding iodine as an additive in an $Mg(TFSI)_2$/DME electrolyte, a functional SEI forms containing MgI_2 which can conduct Mg ions.[60] This layer enabled a significant decrease in the overpotential for Mg deposition and stripping demonstrated in Mg-Mg symmetrical cells, and a decreased charge/discharge voltage hysteresis observed in a Mg-S full cell. Further, protection using a cyclized polyacrylonitrile polymer with $Mg(CF_3SO_3)_2$ enabled use of $Mg(TFSI)_2$/PC electrolyte containing water in a full cell with a V_2O_5 cathode[61] Unlike monovalent Na and Li-based energy storage systems, physical deposition methods have not been demonstrated in any RMB technology thus far. Methods such as ALD are promising for Mg protection due to the ability to precisely control the thickness of the artificial SEI layer down to angstrom scale, although the lack of materials with high Mg mobility available using ALD or other deposition methods is an important issue. There is a great amount of room for investigation and development of both old and new materials for Mg batteries, especially in the application of protection layers.

For future protection efforts, some of the ideal properties of a functional SEI or protection layer should include Mg ion conductivity while also being electronically insulating. Further, due to the potential for break-down of the SEI or protection layer if it is rigid, it may be favorable to use flexible layers like polymers to accommodate any volume change. The use of electrolyte additives to form an SEI is also promising

because if Mg metal is exposed due to SEI degradation during cycling, the layer can be re-formed by the additives instead of having the newly exposed or deposited Mg be immediately passivated. Interfacial properties of Mg anodes and the potential for Mg protection is an open field for examination of different materials, chemistries, and electrolyte systems with a goal to try and solve the issue of Mg anode passivation, thus enabling a wider range of electrolytes to be utilized. This dissertation will discuss the potential for ALD Al_2O_3 as a protective layer for Mg anodes in Chapter 4.

1.5. Status of intercalation cathodes for Magnesium batteries

Utilizing intercalation cathodes in RMB is a major goal for many researchers, although these materials have challenges associated with them. There are a variety of structures that could be utilized in batteries, many of which have been extensively studied in Li-ion batteries. However, moving from Li-ion to magnesium based batteries is not as simple as changing the ion in the electrolyte and changing graphite to Mg metal. Part of the difficulty was discussed in the previous chapter – the Mg interface is passivated by the layers formed upon reactions with conventional electrolytes because Mg^{2+} ions cannot diffuse through the interphase layer. A related issue underlies the difficulty with intercalation cathodes – Mg^{2+} ions have strong electrostatic interactions with the ions in the metal oxide lattices due to its large charge density, and therefore high diffusion barriers in many well-studied materials.[62] Mg^{2+} is similar in size to the Li^+ ion,[63] but it has twice the positive charge. The following sections will introduce some common cathode materials for RMB, as well as some strategies to overcome the limitations for intercalation cathodes in magnesium-based systems.

1.5.1. Overview of common intercalation cathodes

In addition to synthesizing electrolytes compatible with Mg anodes, research in the RMB field has focused on finding and developing cathodes that reversibly (de)insert Mg^{2+} ions, especially those with high voltage and high capacity. Most potential intercalation materials fall under two categories: chalcogenide materials and oxides. The goal is to make a full-cell RMB that contains a cathode, electrolyte compatible with Mg metal, and a Mg metal anode. Full-cell batteries containing intercalation cathodes have not been frequently demonstrated, and none with metal oxides to our knowledge. The first cathode utilized in a proof-of-concept RMB was a chevrel phase material, Mo_6T_8 (T = S, Se) in 2000.[64] Mo_6S_8 is the standard cathode used to demonstrate viability of almost all new electrolytes synthesized in the literature, as it has the best Mg^{2+} insertion and reversibility to date, despite the 20 year period of time since it was first introduced. However, this cathode has a relatively low capacity of 120 mAh/g with a low voltage of 1.2 V vs. Mg.[65]

In addition to the high Mg^{2+} mobility, the chevrel phase cathodes have a unique ability to aid the dissociation of ions from complex electrolyte salts common in electrolytes compatible with the Mg anode.[66] The difficulty of desolvation from the electrolyte and dissociation of Mg^{2+} from complex anions is the other reason why metal oxide cathodes have not been successful in full-cells. The under-coordinated Mo in Mo_6S_8 can aid in the dissociation of Mg^{2+} from anions to which it is ion-paired, but most other metal oxides do not have this catalytic ability meaning complex electrolytes do not enable reversible Mg^{2+} insertion and extraction. For example, MoO_3, while also containing a Mo metal center, is not under-coordinated and has relatively high

calculated activation energy barriers of 1.1 eV and 0.9 eV for dissociation of Mg^{2+} from both Mg—Cl and Mg—TFSI ion pairs, respectively.[67]

The other insertion cathodes demonstrated in a full-cell RMB thus far are other chalcogenide materials, such as layered TiS_2 and spinel Ti_2S_4.[68, 69] These studies utilized a slightly elevated temperature of 60 °C and reported performance at low current densities, but it is important to demonstrate that other cathodes beside the chevrel phase show promise. Other materials being investigated include MoS_2,[70] $Mg_xZr_2S_4$,[71] and MX_2 (M = Ti, V; X = O, S, Se),[72] and others.[65, 73] While chalcogenide materials generally have lower barriers for Mg diffusion, they have lower voltages which means decreased overall energy density of these systems compared to metal oxides. The prospect of higher energy density is one of the main driving forces behind the continued study of metal oxides for RMB.

The most abundantly studied metal oxides thus far are those that are also common in Li-ion battery studies, such as V_2O_5 and MnO_2. As MnO_2 is the structure of interest for this dissertation, a more in-depth analysis of its background and properties will be given in Section 2.1. There has been a significant amount of research in investigating how to make metal oxides viable in RMB, and the work on V_2O_5 gives a good overview of how scientists are approaching the issue. Early on, V_2O_5 was first demonstrated as a potential cathode material by demonstrating that Mg^{2+} insertion was possible in an electrolyte that contained water.[74] The addition of water was proposed to create a solvation shell around the Mg^{2+} ion that helped shield the positive charge and decrease its interaction with the V_2O_5 lattice. This strategy has been further explored in other materials such as manganese oxides[75-77] and $VOPO_4$,[78, 79] and

others,[80] and extended to include the investigation of hydrated materials.[81, 82] While this is one solution to the insertion kinetics issue, having water in the electrolyte or even in the cathode structure may cause water to leach into the electrolyte and react with the Mg anode and passivate the surface. Work is also on-going to investigate some of the desolvation issues at the V_2O_5 interface[83, 84] to determine compatible electrolytes and favorable properties for Mg^{2+} insertion. Computational studies have been done to help determine the best phase of V_2O_5 for Mg insertion,[85, 86] as well as to calculation some of the diffusion barriers to help illustrate the material's properties.[87] While V_2O_5, or any other metal oxide, has yet to been demonstrated in a full-cell RMB, the collective efforts by scientists in the literature are moving the field closer to the answer. An alternate route to a full-cell RMB with a metal oxide cathode, MnO_2 specifically, will be addressed through the research reported in this dissertation.

1.5.2. Effect of nanostructures and thin films

While the intrinsic properties of many cathode materials are the cause for poor performance in RMB, this can in part be mitigated by altering structural parameters of the cathode. Different common electrode structures are illustrated in Figure 1.2. In all these electrodes, the critical transport properties to take into consideration are the ion and electron pathways. In all cases, the electrons will be supplied or removed through the current collector, while the ions will be coming from the electrolyte and interacting with the cathode material shown in grey in each image. In the bulk electrode, both ions and electrons would need to travel a longer distance for the material to be fully utilized. In materials with good electronic conductivity, such as LCO, the ion diffusivity often

becomes the limiting process if the bulk electrode is too thick.[88] In many Mg cathodes, the poor Mg^{2+} diffusion kinetics are worse than Li^{+},[62] meaning bulk electrodes often show little to no electrochemical activity so other structures are needed to study the materials' properties.[75, 89]

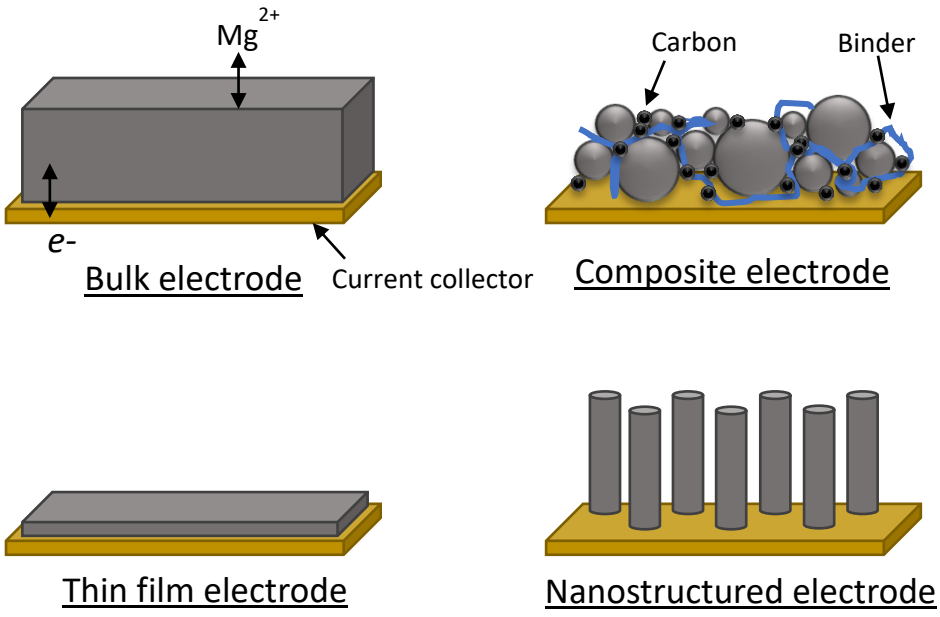

Figure 1.2 Schematic illustrating different types of electrodes utilized in battery studies and their varied structures.

The alternatives to bulk electrodes include composite, thin film, and nanostructured electrodes. Composite electrodes are the most widely used for commercial applications, and the particle sizes are smaller than bulk electrodes. This decreased particle size means ion diffusion into the materials is better than the bulk electrode, and there is also more surface area exposed. The composite electrodes are good for testing overall battery material performance, however trying to determine specific limitations of ion or electron transport may be difficult if the particles are not of uniform size. Further, the distance ions need to travel between particles or electrons from the current collector to the particles vary widely within the electrode, meaning

their contributions to performance cannot easily be deconvoluted. Additionally, these composite electrodes contain both conductive additives and polymer binders whose properties may obfuscate what properties of the material itself may be enhancing or limiting performance.

Thin film and nanostructured materials are controllable structures which can be used to study the inherent ion and electron transport properties of energy storage materials. In thin films, the thickness of the film itself is the only variable to change, assuming it is a system where the ionic or electronic properties are known. The downside to thin films is they are not generally practical from an energy density standpoint, as they do not have much active material from which to derive usable electrical energy. However, they are useful to study fundamental transport properties.

Another way to shorten ion and electron diffusion pathways is by nanostructuring the material. The schematic in Figure 1.2 only illustrates an array of one-dimensional (1D) nanowires, which will be studied in this dissertation. However, there are other 1D, 2D, and 3D materials that have been investigated,[90] although going through the properties of each is beyond the scope of this dissertation. Using the nanowires as an example, the ions can diffuse through any point along the length of the nanowire, meaning the diffusion path length into the bulk of the material at the core of the nanowire is much shorter than a thick bulk electrode. However, there is much more material in the same area when compared to the thin film electrode, meaning more energy can be stored than a thin film while still having the improvement of decreased ion diffusion length. Having this type of controllable structure means properties like

the length of the nanowire can be changed to selectively study the effect of electron transport or the diameter of the nanowire could be changed to study ion transport.

1.6. Overview of Dissertation

The work included in this dissertation focuses on fundamental properties of both anode and cathode materials for RMB, specifically investigating the importance of surface properties of these electrodes. In particular, the effects of engineering surface layers and precision nanostructures are systematically utilized to shed light on important properties of these interfaces and how both mesostructure and surface chemistry can affect the charge storage mechanisms.

- Chapter 2 will present in-depth XPS analysis of the surface of MnO_2 thin film cathodes to demonstrate the effect of adding water into organic electrolyte and elucidate the charge storage mechanism.
- Chapter 3 will introduce PEDOT/MnO_2 coaxial nanowires as a test-bed structure to investigate the effect of electronic conductivity and physical conductive polymer layers on the surface of MnO_2 nanowires and how it affects the diffusion and surface-dominated reaction processes.
- Chapter 4 will discuss the potential for ALD Al_2O_3 as a protective layer for Mg metal and present methods for testing the effectiveness of these layers in a RMB system.
- Chapter 5 will present results on the polymerization of a common battery solvent, 1,3-dioxolane, via the addition of an Mg^{2+} salt catalyst and some electrochemical properties and applications of this polymer.

Chapter 2: Determination of MnO_2 charge storage mechanism in water-containing electrolyte using X-ray Photoelectron Spectroscopy

Portions of this chapter have been published in Sahadeo et al., Investigation of the water-stimulated Mg^{2+} insertion mechanism in an electrodeposited MnO_2 cathode using X-ray photoelectron spectroscopy. *Phys. Chem. Chem. Phys.* ***2018****, 20, 4, 2517-2526., reproduced with permission from the Royal Society of Chemistry.* (https://doi.org/10.1039/C7CP06312A) *Some of the work was started by Dr. Jaehee Song and included in her dissertation.*[91] *Additional experiments and results were completed as a part of this dissertation, including repeating Dr. Song's studies, designing experiments for depth profiling and angle-resolved XPS, air exposure experiments, and electrochemical and SEM analysis.*

2.1. Introduction

Manganese oxides come in a variety of crystal structures that have been studied as cathodes in different energy storage technologies, although arguably they have been most thoroughly studied for Li-ion batteries.[92] Manganese oxides are attractive due to their low toxicity and wide abundance, in addition to the array of structures from which to choose. The utility of these materials has led to their application in beyond-lithium-ion systems, including both Zn[93, 94] and Mg[6] chemistries, to name a few. While different stoichiometric compositions of manganese oxides are available, manganese dioxide (MnO_2) is one of the prevalent materials in energy storage applications. MnO_2 can be synthesized using different methods, including sol-gel,[95, 96] hydrothermal synthesis,[97] and electrodeposition,[96, 98] and different phases can be synthesized using these methods with alterations to the synthesis conditions. Some common polymorphs studied in RMBs include tunnel structures such as hollandite (α), the layered birnessite structure (δ), pyrolusite (β), and spinel (λ).[99] While each of these structures is composed of the same MnO_6 octahedral unit in different crystallographic corner and edge-sharing

arrangements, they do not all support reversible insertion of multivalent ions and can have different charge storage mechanisms.[100]

Of the synthesis methods mentioned above, electrodeposition provides many advantages for studying the fundamental chemistry of MnO_2. Electrodeposition is versatile in that it can be performed either potentiostatically (constant voltage), galvanostatically (constant current), or using CV. Further, since it requires a conductive current collector for the deposition, the structure of the material can be modified based on the structure of the current collector to study different morphologies and mesostructures.[101] Controllable nanostructures can also be synthesized using templates such as porous anodized aluminum oxide (AAO). AAO consists of vertically aligned pores, and in order to deposit within the pores the current collector is deposited on the bottom of the pores and 1D nanowire arrays are formed as the electrodeposited material grows inside the well-defined pores.[102] AAO has been widely used by our group for many different studies of structural effects on electrochemistry, as the pore size and nanostructure length can be systematically controlled to study different aspects of the material properties, ion transport, and electron transport.[103-105] Electrodeposition also removes the need for any conductive additives or binders common in composite electrodes, making them ideal for studying the true material properties of MnO_2.

The electrochemical reaction that will be used to deposit MnO_2 in this work is anodic electrodeposition. It is a one-step deposition process where the Mn species in an aqueous solution is oxidized to form MnO_2, demonstrated in Equation 2.1.

$$Mn^{2+}(aq) + 2H_2O(l) \rightarrow MnO_2(s) + 4H^+(aq) + 2e^- \qquad \text{Equation 2.1}$$

This electrodeposition reaction provides amorphous MnO_2 which does not possess long-range crystallographic order; however, it may contain smaller crystal domains. When examined using Raman spectroscopy, the electrodeposited MnO_2 studied in this dissertation contains peaks which possess vibrational modes indicative of δ-MnO_2.[75] Amorphous materials can be beneficial due to less rigid interstitial spacing and sites for ions to insert, where well-defined crystal structures may be limited by strict tunnel sizes and inter-layer spacings.[100, 106] If the sites in these structures are not favorable for Mg^{2+} insertion, then some structures are not viable as cathodes without further structural modification or other strategies to help aid ion insertion. Structural influences and strategies will be further addressed in Chapter 3.

The work in this chapter is a follow-up to previous work published by our group.[75] It was demonstrated that electrodeposited MnO_2 was only able to reversibly insert/retract Mg^{2+} ions when water was present in an organic propylene carbonate electrolyte and the MnO_2 was in a nanostructure morphology. The capacity and cyclability of this electrode in water-containing electrolyte was the highest reported at the time, and an interesting effect was observed that the MnO_2 could be cycled in water-containing electrolyte and then transferred into dry electrolyte and still demonstrate reversible Mg (de)insertion, which we call a "water-activation" process.

Other reports of MnO_2 polymorphs and their electrochemistry are important to consider when evaluating possible cathode materials. Although a different structure than the electrodeposited MnO_2, computational studies of α-MnO_2 indicated that conversion reactions forming MgO and MnO upon insertion of Mg^{2+} into the metal oxide structure were thermodynamically favorable, and while Mg^{2+} insertion was

determined to be kinetically possible in small nanostructures, conversion could still occur above a critical Mg concentration of 0.125Mg per MnO_2 unit.[107] This result was supported by experiments showing that K^+-stabilized α-MnO_2 formed a shell of conversion products upon Mg^{2+} insertion.[108] With these works in mind, it was important to determine what the charge storage mechanism was in our electrodeposited MnO_2 cathode, especially due to its cyclability in dry electrolyte. A study published within a few months of our own also confirmed that crystal water and water-containing organic electrolytes for δ-MnO_2 indeed help to improve Mg^{2+} insertion, and their cathode demonstrated over 60% capacity retention over 10,000 cycles in an aqueous electrolyte.[109] Another study demonstrated that the charge storage mechanism for δ-MnO_2 was more insertion-based in aqueous electrolytes, while in organic electrolytes conversion was favored.[76]

To follow-up on our previous study, the work in this chapter utilized XPS to investigate the charge storage mechanism of Mg^{2+} insertion in a water-containing $Mg(ClO_4)_2$/PC electrolyte. As MnO_2 electrodes in the literature demonstrated different mechanisms depending on either organic or aqueous electrolyte, it was critical to determine what the charge storage mechanism was in the mixed electrolyte system. Further, we wanted to confirm the origin of the water-activation effect to help determine the feasibility of using this cathode in a full-cell RMB. The work herein utilizes different XPS capabilities, such as angle-resolved XPS and depth profiling XPS, to investigate the charge storage mechanism of electrodeposited MnO_2 in water-containing organic electrolyte.

2.2.Experimental Methods

2.2.1. Synthesis of Thin Film MnO_2 Electrodes

To perform XPS analysis on the electrodeposited MnO_2, a thin-film structure was necessary as opposed to a nanowire morphology. The thin film MnO_2 electrode was prepared using an electrodeposition method. First, 150 nm thick platinum (Pt) was sputtered on the branched side of a Whatman anodized aluminum oxide (AAO) template as a current collector using a Denton Desk III sputter coater. Copper tape with conductive adhesive (3M) was then attached to the Pt sputtered side of the AAO as a contact for electrodeposition. The electrode was sealed between two layers of parafilm with an exposed circular area punched out to define the electroactive area (0.32 cm^2) and sealed using a heat gun. The electrodeposition was performed in a three-electrode cell, with Ag/AgCl as the reference electrode, Pt foil as the counter electrode, and the AAO as the working electrode. The deposition solution was 100 mM manganese acetate tetrahydrate in Millipore water, and the oxidative electrodeposition was done at a constant voltage of 0.60 V vs. Ag/AgCl. Varying the amount of charge passed enabled the thickness of the MnO_2 layer to be precisely controlled. The as-prepared MnO_2 working electrode was carefully rinsed with Millipore water, dried, and then soaked in the electrolyte solution prior to testing.

2.2.2. Electrochemical Measurement

For electrochemical studies, both dry and water-containing electrolytes were made. The water-containing electrolyte was 0.1 M $Mg(ClO_4)_2 \cdot 6H_2O$ in propylene

carbonate (PC), while the dry electrolyte was 0.1 M $Mg(ClO_4)_2$ (anhydrous) in PC. All electrolytes were purged using Ar gas before measurement. Three-electrode cells were employed with MnO_2 on AAO as the working electrode, Pt foil as the counter electrode, and Ag/AgCl as the reference. All voltages reported are vs. Ag/AgCl unless otherwise indicated. The MnO_2 samples were electrochemically tested using a few different techniques. Chronoamperometric (CA) experiments were employed to discharge electrodes by holding potential at -0.4 V for 5 minutes, and charged electrodes were held at 1 V for 5 minutes following an initial discharge. The cyclic voltammetry (CV) technique was used with a potential window of -0.4 to 1.2 V, and the CV was stopped in either charged (de-magnesiated) or discharged (magnesiated) state by ending the scans at either end of the potential window. To further drive reactions to completion, the CV was followed by a CA potential hold (either -0.4V or 1V) until a negligible current was observed, driving the reaction at the electrode nearer to a fully charged or discharged state. The treatment of specific electrodes will be identified in the text.

To determine the effect of pre-activating electrodes by cycling in water-containing electrolyte, MnO_2 thin films were activated using cyclic voltammetry and left at different stages of magnesium insertion and de-insertion. The first type of electrode was cycled and left in the discharged, or Mg inserted, state referred to as AD-MnO_2. The second electrode was cycled and left in the charged, Mg retracted, state referred to as AC-MnO_2. The pre-cycling of MnO_2 electrodes was done by cycling the electrodes for 10 cycles between -0.4 and 1.2 V in 0.1 M of $Mg(ClO_4)_2 \cdot 6H_2O$/PC. To assess the electrodes in dry electrolyte after activation, the electrodes were rinsed with dry PC and moved into a cell with dry 0.1 M $Mg(ClO_4)_2$/PC. For XPS analysis of the

activated electrodes, both AD-MnO_2 and AC-MnO_2 electrodes were cycled in dry electrolyte for 3 CV cycles then the potential was held at -0.4 V for 5 minutes.

2.2.3. X-ray Photoelectron Spectroscopy (XPS)

Ex-situ XPS analysis was performed by using a Kratos AXIS 165 spectrometer operating in hybrid mode using monochromatic aluminum x-rays. Survey spectra and high resolution spectra were collected with pass energies of 160 eV and 40 eV respectively. Charge neutralization was required for all samples. A differentially pumped monoatomic argon ion sputter source operating at 4 KV and 20 mA, with a beam diameter of ~1 mm and beam current of ~3.1 µA (measured at the sample holder) was employed for depth profiling. The sputter gun was calibrated using a standard Ta sample with 1000 Å of Ta_2O_5, and the beam current of 3.1 µA used in our sputter depth profiles is equivalent to a sputter rate of 1.7 nm/min on Ta_2O_5. The sputter source was rastered resulting in a crater of ~7 x 7 mm. For angle resolved measurements the iris was reduced to 5 mm to improve angular resolution. All peaks were calibrated to the hydrocarbon peak at 284.8 eV, except for the depth profiling studies which were calibrated to Cl 2p at 198.8 eV upon disappearance of adventitious carbon after ion etching. The curves were fitted using CasaXPS software. Spectra were processed using a 70%-30% Gaussian-Lorentzian product function and a Shirley-type background[110].

While samples were analyzed ex-situ, steps were taken to ensure minimal air exposure. Samples were electrochemically treated so that they were fresh before XPS analysis, and not allowed to sit in air for extended time. They were kept wet with PC after rinsing, and then transferred directly into a vacuum desiccator that was vacuumed

and then purged with Ar gas three times to minimize contact with the atmosphere. Samples were only exposed to air for about 5 minutes during transfer into the XPS vacuum chamber.

2.3. Results and Discussion

2.3.1. Characterization of MnO_2 thin films

For this study, a thin film morphology was essential to make clear observations using XPS. The high aspect-ratio nature of nanowires does not give a uniform surface upon which small changes in surface chemistry can be easily identified. However, very thick (>1-2 μm) electrodeposited films cannot be magnesiated.[75] Conversely, when films are very thin, e.g. tens of nanometers, and deposited on planar substrates, they cannot be cycled extensively before degradation occurs. To get enough nanostructure to extend the cyclability while keeping the films thin, a nanostructured substrate was chosen that also was uniform and flat enough for the surface-sensitive XPS technique. On the back side of Whatman AAO, when Pt or other metals are sputtered small nanometer grains form on the walls of the AAO as seen in Figure 2.1a. When MnO_2 is electrodeposited, it conforms to the Pt grains as illustrated in Figure 2.1b. The thickness can be altered based on the amount of charge passed, with a 15 mC deposition giving a thickness of ~50 nm in Figure 2.1b. Also, it is important to note that the electrodeposited MnO_2 is amorphous, although it has vibrational modes characteristic of delta-phase, layered MnO_2 as indicated by the Raman spectrum in Figure 2.2a.

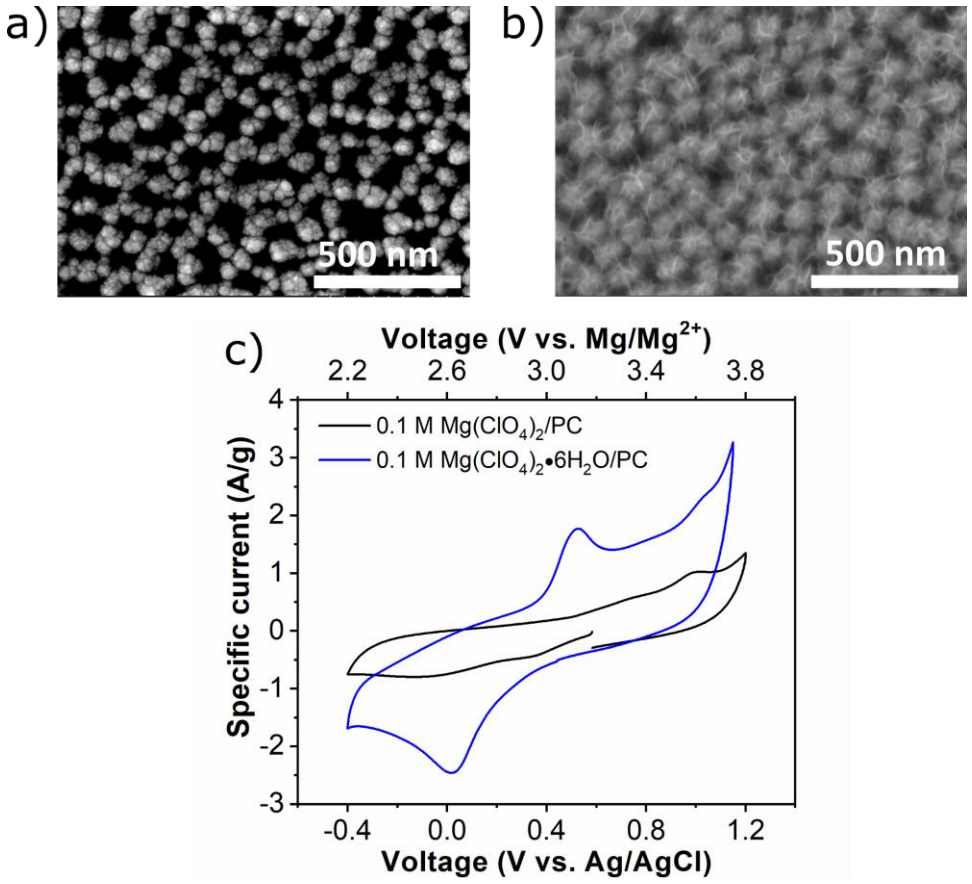

Figure 2.1 SEM images of a Pt sputtered AAO electrode (a) prior to electrodeposition and (b) after 15 mC of MnO_2 was electrodeposited. (c) Cyclic voltammogram of MnO_2 cycled at 0.5 mV s^{-1} in 0.1 M $Mg(ClO_4)_2 \cdot 6H_2O$ in propylene carbonate electrolyte, and dry 0.1 M $Mg(ClO_4)_2$/PC electrolyte.

2.3.2. Confirmation of water-activation in MnO_2 film

To confirm the water-activation effect from our previous study[75] in the thin film MnO_2, MnO_2 cathodes were electrodeposited until 15 mC of charge was passed. One electrode was cycled using CV in dry 0.1 M $Mg(ClO_4)_2$/PC electrolyte as a control, while a second was cycled in electrolyte containing 0.1 M $Mg(ClO_4)_2 \cdot 6H_2O$ in PC, which was the optimal ratio determined previously.[75] Representative CV curves can be seen in Figure 2.1c. There is increased capacity observed in the CV of MnO_2 in wet electrolyte as compared to the dry electrolyte, indicating the positive effect resulting

from the addition of water previously observed in MnO_2 NWs is also observed in the nanostructured film. Two peaks are present, one at 0.5 V in the anodic scan, and about 0.1 V in the cathodic scan, which we assign as indicative for the oxidation of Mn^{3+} to Mn^{4+} and reduction of Mn^{4+} to Mn^{3+}, respectively.[111] However, the exact valence states of Mn during the discharge and charge process were not able to be further confirmed via XPS in the current study due to the fact that there are likely multiple manganese oxide species present throughout the sample after cycling, which severely complicates the oxidation state determination via XPS.[112] Some evidence of Mn reduction can be deduced from increased contributions at lower binding energies in the Mn $2p_{3/2}$ peak upon discharge, shown in Figure 2.2b. The contributions from lower-valent Mn^{3+} shift the peak center to lower binding energy, which then shifts back to the pristine binding energy upon charging, confirming the reversibility of the reaction.

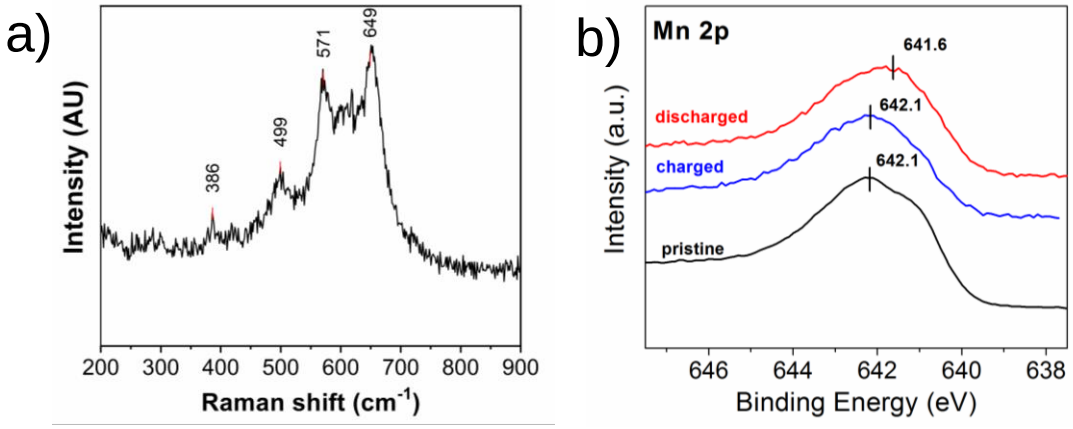

Figure 2.2 a) Raman spectrum of as-deposited MnO_2 on the Pt-sputtered AAO b) Mn 2p XPS spectra for pristine MnO_2, and electrodes charged and discharged after 10 CV cycles in 0.1 M $Mg(ClO_4)_2 \cdot 6H_2O$/PC electrolyte.

2.3.3. Surface analysis of MnO_2 cycled in water-containing electrolyte

First, the initial positive effect of water during the activation process, depicted in Figure 2.1c, was investigated to determine what chemical changes are occurring during

the cycling in water-containing PC electrolyte. A series of *ex-situ* XPS measurements with the MnO_2 electrodes was conducted to examine the evolution of chemical speciation on the electrode surface upon discharging and charging of MnO_2. For this study, electrodes were charged and discharged using the CV and CA methods described in the experimental section. It is important to note the XPS is probing solely the first few nanometers at the surface – depth profiling studies were also conducted and will be discussed later.

Figure 2.3 shows the O 1s XPS spectra of MnO_2 electrodes at varying charged and discharged states. For reference, control samples of as-electrodeposited MnO_2 and MnO_2 discharged in dry 0.1 M $Mg(ClO_4)_2$/PC are depicted in Figure 2.3a and b, respectively. For all O 1s spectra collected in this work, there were three major peaks which appeared at binding energies of 530 eV, 531.7 eV, and 533 eV, with error of

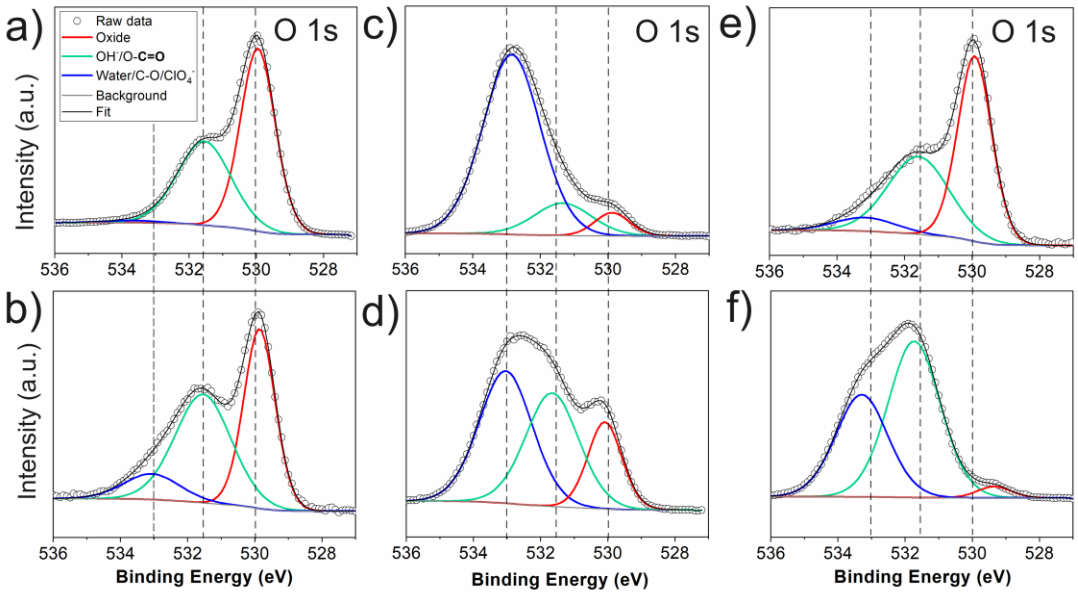

Figure 2.3 O 1s XPS spectra for MnO_2 thin film electrodes. (a) Pristine MnO_2, (b) MnO_2 discharged in dry electrolyte after 2 CV cycles (c) MnO_2 in charged state after 10 CV cycles (d) MnO_2 discharged after 10 CV cycles (e) charged using CA (f) discharged using CA.

±0.2 eV. The lowest binding energy peak at 530 eV is generally due to the O^{2-} from metal oxides,[112] which is most apparent in the pristine MnO_2 and charged electrodes in Figure 2.3a and e, respectively. The middle peak at 531.7 eV is attributed to two functional groups that tend to overlap, which are hydroxide (-OH) and carbonyl (-C=O) species.[113, 114] Examining the O 1s region of the as-deposited MnO_2 electrode in Figure 2.3a, the presence of a peak at 531.7 eV likely indicates some manganese oxyhydroxide (MnOOH) is present on the surface due to the aqueous electrodeposition, and also there may be some carbon species from adsorbed CO_2 also present in the same region. The peak at 533 eV also may have overlapping species, and in the as-deposited MnO_2 it is believed to be water adsorbed on the surface or within the metal oxide structure.[115] However, when examining cycled electrodes, the peaks at 531.7 and 533 eV have contributions from carbon species with C=O or C-O bonds that are part of carboxylic or ester functional groups, or other species resulting from decomposition of propylene carbonate electrolyte.[113] Table 2-1 contains the detailed quantitative results of the components in peak fitted O 1s and C 1s spectra of MnO_2 electrodes to emphasize important differences.

The electrodes activated using CV were examined first, as CV is the method utilized to activate the MnO_2 in both this work and the previous study. The charged and discharged samples are shown in Figure 2.3c and d, respectively. The higher Mg content in the discharged sample is shown in Table 2-1, and the Mg/Mn ratio of the discharged sample is 0.56 compared to the charged sample which is 0.20. This result confirms the insertion of Mg upon discharge, and the reversibility of the reaction is supported by the disappearance of Mg upon charging. However, there is a significant

peak around 533 eV in the O 1s region for both samples, with the charged sample having the largest contribution of 53.8%. This peak indicates that a significant amount of carbon-oxygen and perchlorate species are likely present on the surface and appear to be covering much of the signal from oxide or hydroxide species. To determine what is occurring upon Mg insertion, CA experiments were done to minimize the amount of this layer formation which is present over longer electrochemical tests.

Table 2-1. Atomic composition results determine from XPS analysis of MnO_2 electrodes in various states of charge and discharge

	% Composition							
			O 1s			C 1s		
	Mg 1s	Mn 2p	H_2O/C-O/ClO_4^-	OH/C=O	O^{2-}	C-C/C-H	COOR	C-O
Pristine	-	30.3	0.5	18.6	26.2	14.2	5.3	3.4
Discharged, dry PC (CV)	2.8	16.3	4.7	21.7	17.2	27.2	4.6	4.8
Discharged, wet PC (CV)	6.1	10.8	25.2	21.6	10.6	12.1	2.5	5.9
Charged, wet PC (CV)	1.0	4.9	53.8	9.7	4.2	12.7	2.3	5.9
Discharged, wet PC (CA)	14.4	1.3	21.0	32.0	1.5	12.2	4.3	7.3
Charged, wet PC (CA)	0.5	22.9	3.0	17.1	22.7	20.3	4.9	7.5

The O 1s spectra for MnO_2 samples charged and discharged through holding the potentials are depicted in Figure 2.3e and f, respectively. The reversibility of the Mg^{2+} insertion process in the water-containing electrolyte can again be seen by analyzing the atomic composition of Mg obtained by XPS in the discharged and charged MnO_2 electrodes (Table 2-1). The results show that about 97% of the Mg detected in the surface of the discharged MnO_2 (14.4 %) is retracted upon the charging (0.5 %) revealing highly reversible charge and discharge process of MnO_2 thin film electrode

with Mg^{2+} ions. Analysis of the high-resolution XPS spectra is presented to further elucidate the chemical changes.

When the MnO_2 is discharged in wet electrolyte, depicted in Figure 2.3f, the oxide peak at 530 eV decreases significantly while the peak at 531.7 eV increases. This middle peak indicates an increase in either OH or carbonyl species. Comparing the atomic percent carbon in Table 2-1 and the high resolution C 1s spectra in Figure 2.4e and f, there is not an increase in carbon content or a significant change in the species detected. To give a more in-depth analysis of the O 1s region of the discharged in wet electrolyte sample via CA (Figure 2.3f), we have quantitatively considered all possible contributions. If it is assumed that the entire 4.3% of C=O species in the COOR overlaps with the OH^- region, there would still be 22.5% total OH after subtraction of

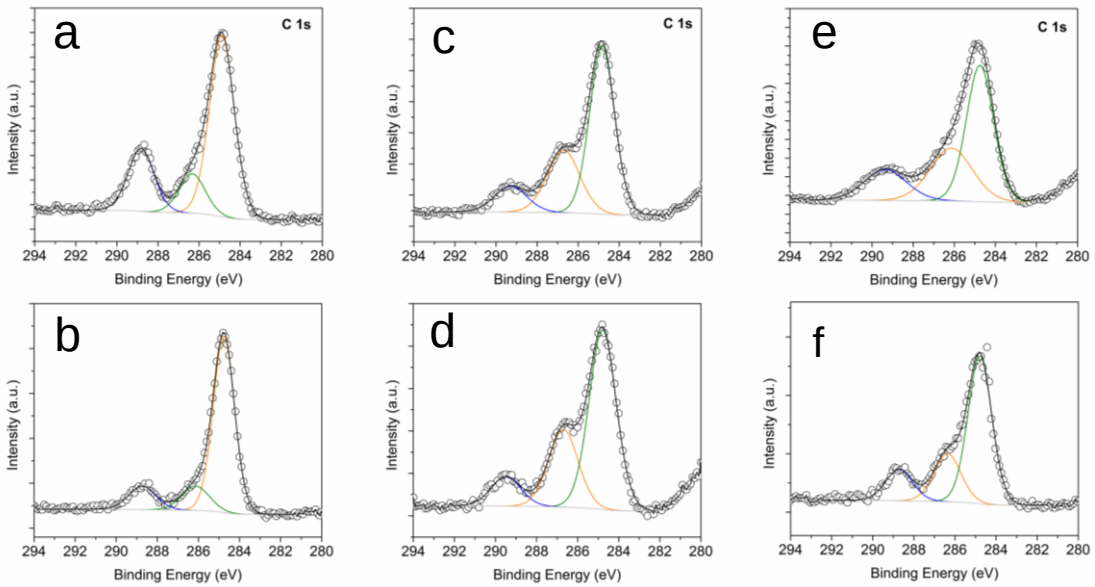

Figure 2.4 C 1s spectra for samples illustrated in Figure 2 of the main text. (a) Pristine MnO_2, (b) MnO_2 discharged in dry electrolyte (c) MnO_2 discharged using CV (d) MnO_2 in charged state after CV (e) discharged using CA (f) charged using CA. The three main components consist of C-C and C-H at 284.8 eV, C-O species at ~286.5 eV, and carboxyl species at 289 eV.

the C=O contribution. In the Mg 1s, we can attribute a further 1.9% to leftover $Mg(ClO_4)_2$ contamination, which by process of elimination leaves 12.5% Mg that can only be $Mg(OH)_2$. The ratio of Mg:OH suggested by this atomic percent (1:1.8) is close to the 1:2 Mg-to-OH ratio expected for $Mg(OH)_2$. Therefore, the increase in the peak at 531.7 eV with respect to the peak for oxide species is mostly attributed to the formation of a hydroxide species. This species forms a thick surface layer that is greater than (or at least comparable to) the sampling depth of XPS (~3-10 nm), such that the manganese oxide component presumed to exist underneath the hydroxide layer was only minimally detected.

While the observed hydroxide layer can potentially be attributed to multiple species, such as $Mg(OH)_2$, $Mn(OH)_2$, or MnOOH, it is important to note that the atomic composition of Mn (1.3%) is significantly reduced proportional to the amount of magnesium (14.4%). This evidence supports the assertion that the hydroxide species is $Mg(OH)_2$, not any manganese associated hydroxide compound. Further, this $Mg(OH)_2$ is likely covering the Mn species underneath. It is also possible that some carbon species are contributing to the signal at the same binding energy as the hydroxide species, however as shown in Table 2-1 the amount of contributions from carbonyl species (COOR component) overlapping the hydroxide is the same within 1-2% for all samples. Therefore, the change in the 531.7 peak is attributed to hydroxide species. The Mg content increases significantly upon discharge also supporting the claim of $Mg(OH)_2$ formation. In the charged MnO_2 electrode, shown in Figure 2.3e, the hydroxide component decreases, and Mn and oxide compositions are restored,

indicating reversible behavior of the $Mg(OH)_2$ formation. The reversibility is further supported by the observed decrease in the amount of Mg after charging.

It is also critical to note that water is required for the formation of the $Mg(OH)_2$, and the water can come from either water-containing PC or aqueous electrolyte. When the MnO_2 is discharged in a dry electrolyte without significant water content, there is only a small increase in the amount of hydroxide species visible in the O1s XPS in Figure 2.3b. Most of the experiments performed here were done in water-containing PC, however electrodes discharged in aqueous electrolyte show similar chemical speciation when analyzed using XPS. In Figure 2.5, MnO_2 fist discharged and then recharged can be seen in (a), while the MnO_2 discharged in aqueous electrolyte is shown in (b). The decreased oxide component is still seen in aqueous electrolyte similar to wet electrolyte, and the reaction is also reversible upon charging. However, there is more Mn still visible upon discharge in the aqueous samples (5.3%) listed in Table 2-2, compared to in the wet PC (1.3%).

While the mechanism of these reactions will be discussed in detail later, the observation of more Mn indicates that in aqueous electrolyte insertion may be more favored, while in water containing electrolyte, we see a combination of conversion and insertion reactions. While $Mg(OH)_2$ forms in aqueous electrolyte, it is to a lesser extent than in water-containing PC, therefore there is a thinner layer on the surface leaving more Mn exposed. Different mechanisms based on the type of electrolyte were observed by Nazar and coworkers[76] for birnessite MnO_2; organic electrolyte led to a conversion mechanism, while aqueous electrolyte favored insertion. Therefore, it is plausible that a mixed electrolyte system has a combination of insertion and conversion

reactions. Further, the reversibility of $Mg(OH)_2$ formation appears unique to the MnO_2 redox reactions. With aqueous electrolyte there may be some additional side reactions with water, with precipitated or electrochemically formed $Mg(OH)_2$ being one of the possible products. Precipitated $Mg(OH)_2$ formation on the surface of MnO_2 was ruled out by an electrochemical precipitation study by Jaehee Song in her dissertation.[91] It was demonstrated that cathodic electrodeposition of $Mg(OH)_2$ could not be removed from a Pt electrode upon application of an oxidative potential.

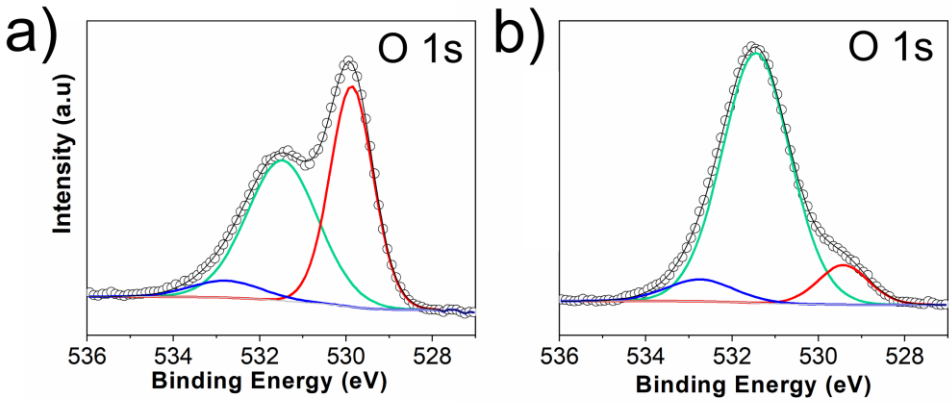

Figure 2.5 High-resolution XPS results for electrodes in aqueous $Mg(ClO_4)_2$ electrolyte. (a) Charged MnO_2 and (b) discharged MnO_2, both via CA.

Table 2-2. Atomic composition results for MnO_2 in aqueous electrolyte

	% Composition							
			O 1s			C 1s		
	Mg 1s	Mn 2p	H_2O/C-O/ClO_4^-	OH/C=O	O^{2-}	C-C/C-H	COOR	C-O
Charged MnO_2	1.3	18.0	1.0	22.5	19.0	24.6	3.9	5.8
Discharged MnO_2	7.3	5.3	4.0	47.1	5.4	18.6	3.8	2.6

2.3.4. Depth profiling of MnO_2 cycled in water-containing electrolyte

XPS depth profiles were performed in order to examine the distribution of Mg throughout the MnO_2 samples. For the depth profiles, the CV method was employed to cycle the MnO_2 electrodes to their charged and discharged states. Because the depth is examined through sputtering with the ion gun, the surface layers that were initially

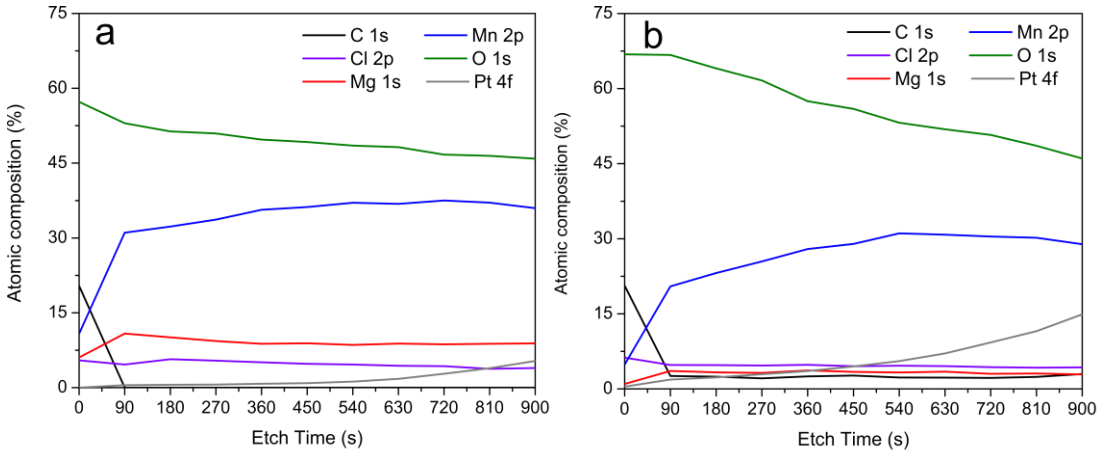

Figure 2.6 Depth profiles of all elements in the a) discharged and b) charged MnO_2 electrodes in 0.1 M $Mg(ClO_4)_2 \cdot 6H_2O$/PC electrolyte after 10 CV cycles.

problematic for surface analysis are not consequential when probing the relative amounts of elements in the samples. Each sample was cycled for 10 cycles and stopped at either -0.4 or 1.2 V, and then underwent a potential hold for 5 minutes at the respective oxidative or reductive potential prior to XPS analysis. Due to preferential sputtering of oxygen and reduction of manganese species by the Ar ion gun, the depth profiles cannot be used to accurately examine the different oxidation states of manganese oxide species throughout the sample. However, it gives insight into the relative amount of different species detected. The full depth profiles for all elements in discharged and charged MnO_2 samples are in Figure 2.6. For the discussion here, the depth profiles in Figure 2.7 depict the Mg/Mn ratios of MnO_2 samples in both the charged and discharged states.

The depth profiles show the changes in the amount of Mg and Mn throughout the sample. In the discharged MnO_2 sample there is a steady Mg content of about 10% throughout the depth of the sample, while it is only 3% in the charged sample (Figure 2.6). These results combined with the Mn data give the overall ratios of Mg to Mn as

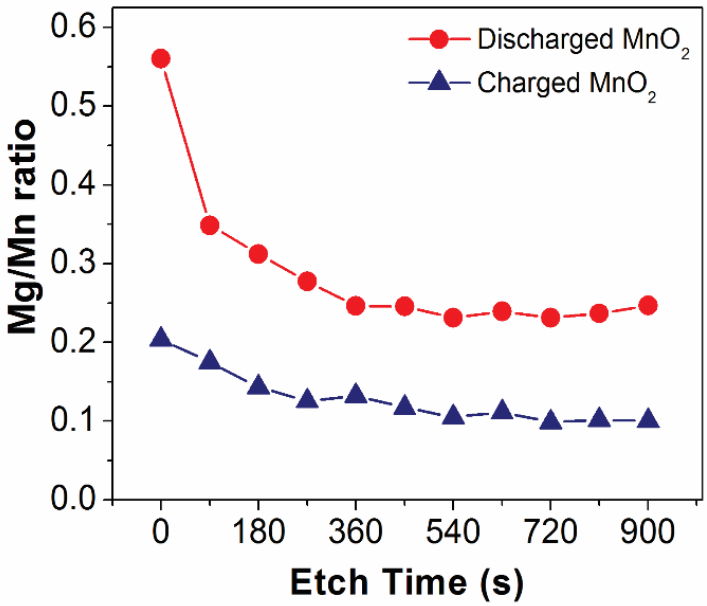

Figure 2.7 Mg/Mn ratios of AD-MnO_2 (stopped at discharged state) and AC-MnO_2 (stopped at charged state) over 10 etching steps each lasting for 90 seconds. The electrolyte used for CV cycling was 0.1 M $Mg(ClO_4)_2 \cdot 6H_2O$ in PC.

provided in Figure 2.7. There is a high concentration of Mg at the surface of the discharged sample (0.6 Mg/Mn) and a constant ratio of ~0.25 Mg/Mn underneath the surface. The charged sample has a ratio of ~0.2 Mg/Mn at the surface and 0.1 throughout the depth examined. These results support that a Mg-containing layer is more prevalent on the surface of the discharged sample, which is subsequently removed upon charging of the MnO_2. The presence of magnesium deeper within the bulk of the MnO_2 film is evidence that indicates insertion of Mg is also occurring in addition to the reactions on the surface.

Considering both the XPS depth profiling and high resolution XPS analysis, we believe there is more than just a simple insertion reaction occurring in water-containing electrolyte. There is distinct, reversible formation of $Mg(OH)_2$ on the surface of the MnO_2 indicative of a conversion process which requires the presence of water.

However, there is also Mg insertion detected throughout the film, not just on the surface where the conversion occurs. Considering these results, we propose the following charge storage mechanism of MnO_2 in the presence of water molecules:

$$x\mathrm{Mg}^{2+} + \mathrm{MnO_2} + 2x\mathrm{e}^- \longrightarrow \mathrm{Mg}_x\mathrm{MnO_2} \qquad \text{Equation 2.2}$$

$$+ \mathrm{H_2O} \quad \searrow \quad \uparrow\downarrow \quad + \mathrm{H_2O}$$

$$\mathrm{Mg(OH)_2} + \mathrm{Mg}_x\mathrm{Mn}_y\mathrm{O}_z \qquad \text{Equation 2.3}$$

The reversible oxidation and reduction of Mn in MnO_2 is apparent from the CVs collected, in addition to the shifting of the Mn 2p peak in XPS (Equation 2.1). This redox behavior is accompanied by the insertion of Mg^{2+}, which was confirmed by EQCM and ICP in a previous study.[75] While concentrations of Mg and Mn in this work were too low for ICP, an SEM cross section maps in Figure 2.8 can give support to Mg insertion into the bulk of the film. Further, the XPS depth profile results provide evidence to conclude that inserted Mg exists under the $Mg(OH)_2$ layer. In the presence of water molecules, Mg_xMnO_2 converts to an inhomogeneous composition of $Mg(OH)_2$ on the surface layer and possible reduced manganese oxide species underneath of $Mg(OH)_2$, although its precise composition is not known. Another possible discharging

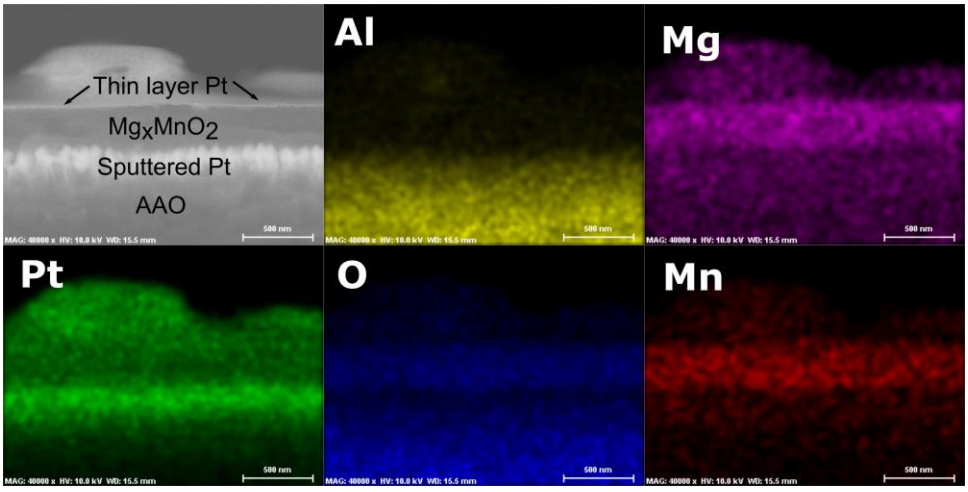

Figure 2.8 SEM-EDS maps for a 300 nm thick film of MnO_2 discharged using the CA method.

mechanism is direct conversion from MnO_2 to $Mg(OH)_2$ and reduced manganese species (Equation 2.2), simultaneous with Mg insertion. There are likely MnO, MnOOH, or $Mn(OH)_2$ species present underneath of $Mg(OH)_2$ based on the decreased Mn composition with increased hydroxide component and vice versa demonstrated in the XPS data. Upon charging, the oxidation of Mn species reverses the conversion reaction which formed $Mg(OH)_2$, which was determined to otherwise be irreversible as reported by Song.[91] The initial surface XPS studies combined with electrochemical data give a foundation for our mechanism when cycling in water-containing electrolyte. The next section will investigate the observed water-activation phenomenon where Mg^{2+} insertion is still observed when the MnO_2 electrodes are transferred to dry electrolyte.

2.3.5. Charge storage mechanism of pre-activated MnO_2

To understand the mechanism of the observed activation phenomenon of MnO_2 nanowire electrodes discussed in our previous publication[75] and to elucidate on the observations of the surface properties of the activated thin film MnO_2 electrodes in the previous section, further XPS studies were conducted. The thin films were deposited and cycled in water-containing electrolyte using CV as previously described and stopped at either their charged or discharged state. Potential holds were then applied for 5 minutes at either -0.4 V (AD-MnO_2) or 1 V (AC-MnO_2) to fully insert or remove Mg^{2+} ions. The pre-cycled electrodes were then cycled in dry electrolyte to examine the evolution of the surface species relevant to the water-activation effect. Figure 2.9a shows the CV of activated and pristine MnO_2 electrodes cycled in the dry electrolyte at a scan rate of 0.5 mVs^{-1}. The differences in the voltammograms give insight into the

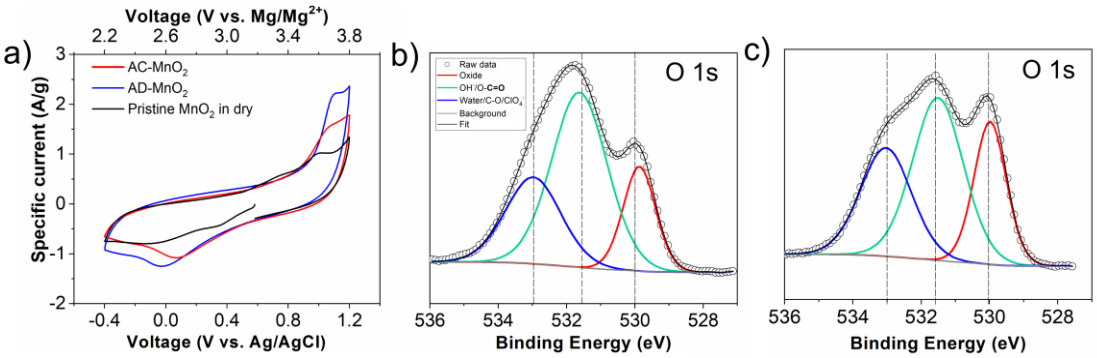

Figure 2.9 XPS spectra for pre-cycled MnO_2 electrodes cycled in dry electrolyte. (a) CVs of AC-MnO_2, AD-MnO_2, and pristine MnO_2 electrodes cycled in 0.1 M $Mg(ClO_4)_2$/PC electrolyte at 0.5 $mV \cdot s^{-1}$ and O 1s spectra for (b) AD-MnO_2 and (c) AC-MnO_2 electrodes after 2 CV cycles in dry electrolyte.

importance of the contribution of water molecules from the electrolyte.

Upon inspection of the CV curves in Figure 2.9a, the oxidation and reduction peaks are similarly separated after activation regardless of the state of charge of the electrode. This result indicates a higher overpotential for redox of the MnO_2, predominantly for the oxidation reaction, which is likely due to the presence of less water in the system overall. However, another important trend is that the electrode left in the discharged state, AD-MnO_2, has a higher peak current and overall higher capacity compared to the electrode left in the charged state, AC-MnO_2. The AD-MnO_2 is expected to have Mg^{2+} and co-intercalated water still inside the lattice with $Mg(OH)_2$ on the surface, while AC-MnO_2 has Mg^{2+} ions and excess water removed with minimal $Mg(OH)_2$ on the surface. However, both electrodes are believed to have water trapped within the MnO_2, although more is expected in the case of AD-MnO_2. Figure 2.9b and c show O 1s spectra of AD-MnO_2 and AC-MnO_2 that were cycled in dry electrolyte and left in the discharged state. Both electrodes demonstrate an increase in OH contributions at 531.7 eV upon discharge, though more OH is apparent in the AD-MnO_2 sample. While all

the OH cannot be definitively ascribed to $Mg(OH)_2$ due to the visible amount of Mn, the increase in OH is still accompanied by the discharge and subsequent Mg insertion. This possible layer formation is also apparent through the decreased amount of both oxide and manganese signals in AD-MnO_2 as compared to AC-MnO_2, as well as the larger amount of OH detected in AD-MnO_2. The atomic composition and peak fitting data for the XPS spectra are shown in Table 2-3.

Table 2-3. Atomic composition results determined from XPS analysis of activated electrodes cycled in dry electrolyte and stopped in the discharged state

	% Composition							
			O 1s			C 1s		
	Mg 1s	Mn 2p	H_2O/C-O/ClO_4^-	OH/C=O	O^{2-}	C-C/C-H	COOR	C-O
AC-MnO_2	6.1	17.5	14.5	21.7	12.1	15.9	4.1	3.6
AD-MnO_2	6.1	12.4	12.6	25.5	9.0	20.0	5.5	6.0

To further investigate the OH formation on the surface, angle-resolved XPS (AR-XPS) was performed on AD and AC-MnO_2 samples that were discharged in dry electrolyte. In AR-XPS, the sample stage is tilted to alter the take-off angle of the electrons from the surface. At smaller angles relative to the sample surface, electrons are detected from a shallower depth while at larger angles the electrons are collected from deeper into the bulk of the sample. In this study, analysis was done at electron take-off angles of 90° and 20° (with respect to the sample surface). The AR-XPS for AC-MnO_2 and AD-MnO_2 are in Figure 2.10a and b, respectively, and all data is normalized to the O^{2-} peak. In the O 1s data in Figure 2.10a, the increase in signal is apparent in the OH and H_2O/C-O regions at 531.7 and 533 eV, respectively. As the XPS gets more surface sensitive, there is more hydroxide species as well as some carbon species from surface contamination. Most important is the increase in the

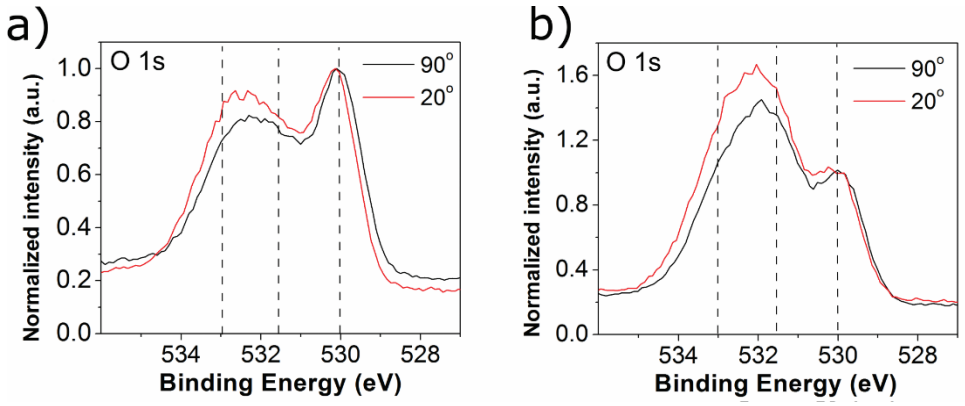

Figure 2.10 Angle-Resolved O 1s XPS spectra for (a) AC-MnO_2 discharged in dry electrolyte and (b) AD-MnO_2 discharged in dry electrolyte.

Table 2-4. Atomic composition results for AR-XPS of activated electrodes cycled in dry electrolyte

	% Composition		Peak ratio	
	Mg 1s	Mn 2p	C–O/C–C	OH/O^{2-}
AC-MnO_2 – 90°	2.4	15.6	0.36	0.7
AC-MnO_2 – 20°	2.4	14.5	0.33	0.9
AD-MnO_2 – 90°	5.5	9.7	0.28	1.6
AD-MnO_2 – 20°	6.6	11.0	0.25	1.8

amount of OH relative to O^{2-} as indicated in Table 2-4. This observation supports the formation of hydroxides closer to the surface. Additionally, in Figure 2.10b, the same increase in the OH and H_2O/C-O regions is clear, and there is a marked increase in OH compared to O^{2-}. However, in the AD-MnO_2 there is a larger overall OH/O^{2-} ratio. This result makes sense, as the AD-MnO_2 is believed to contain more water and therefore have a larger propensity for $Mg(OH)_2$ formation, and hydroxide formation in general. The AD-MnO_2 sample has a larger amount of Mg visible at the surface, with Mg/Mn ratios of 0.57 at 0.59 at 90° and 20°, respectively. Conversely, the Mg/Mn ratios of the AC-MnO_2 are 0.15 at 90° and 0.17 at 20°. The higher Mg/Mn ratios for AD-MnO_2 further support that the OH formation is directly related to the discharge and Mg insertion process and shows a correlation with water content in the electrode.

The pre-activated electrodes' electrochemical response and surface chemical speciation upon cycling in dry electrolyte give important insight into the role of water in Mg insertion into MnO_2. When cycling in water-containing electrolyte, if all the water which co-intercalates with Mg^{2+} is removed upon charging, $Mg(OH)_2$ would not be formed upon cycling in dry electrolyte, especially in AC-MnO_2. Further, the extent of $Mg(OH)_2$ formation is influenced by what state of charge the MnO_2 is in, thus the amount of water likely in the structure, with AD-MnO_2 showing more extensive $Mg(OH)_2$ conversion products than AC-MnO_2. These observations support the proposal that some water remains in the MnO_2 structure after cycling in wet PC electrolyte. Additionally, the presence of structural water is a likely explanation for the water activation phenomenon where MnO_2 retains capacity after cycling in wet electrolyte and transferring the electrode to dry electrolyte.

As mentioned in the introduction to this chapter, many groups have studied Mg insertion mechanisms into a variety of polymorphs of MnO_2, including λ-MnO_2,[116] α-MnO_2,[107] and other studies of δ-MnO_2.[76, 109] Despite differences in the crystal structures studied, there is a general trend that intercalation of Mg is favored in aqueous electrolyte systems, while surface conversion reactions predominate in non-aqueous or organic electrolyte systems. A recent study by Sun et.al. reported on the mechanisms for the same δ-MnO_2 in both aqueous and organic systems. They also observed significant $Mg(OH)_2$ formation in addition to MgO on the surface, and they were able to differentiate some Mn species using XPS and EELS.[76] Similar to our study, the insertion is attributed to the ability of water to solvate Mg^{2+} and screen the charge from the metal oxide. They propose that the conversion reaction in non-aqueous electrolyte

occurred due to the increased thermodynamic stability of $Mg(OH)_2$ and MgO products which form from unstable Mg_xMnO_2. Our results lead to a somewhat different conclusion in our amorphous material, and we propose that in a mixed water-containing organic electrolyte system there is a combined insertion mechanism and $Mg(OH)_2$ formation. We suggest that in systems where water is present, whether aqueous or mixed water-in-organic electrolyte or cathodes containing structural water, there is insertion of Mg^{2+} into the amorphous electrodeposited MnO_2. This insertion is either simultaneous with a conversion reaction, or a conversion reaction follows insertion, giving $Mg(OH)_2$ at the surface and reduced MnO, MnOOH, or $Mn(OH)_2$ species in the bulk. Also, we suggest that the formation of $Mg(OH)_2$ in conjunction with the charge screening effect could be the driving force that has generated the observed improvement in Mg^{2+} capacity in the presence of water molecules.

2.3.6. Effect of air Exposure on XPS analysis

To test the effect of air exposure, two MnO_2 samples of different thicknesses (one deposited by passing 15 mC of charge, the other was deposited by passing 5 mC of charge) were first electrochemically treated outside of the glovebox in the same manner as described in the experimental section. However, after being rinsed with PC to remove salt species, they were transferred directly to the antechamber of a MBRAUN glovebox with <0.5 ppm water and oxygen instead of being moved into a vacuum desiccator. The electrodes were still wet with PC during transfer to prevent as much air exposure as possible. They were also transferred from the glovebox to a glove bag attached to the XPS vacuum chamber without any air exposure. With these precautions,

the samples were not exposed to air. After taking the XPS spectra in Figure 2.11a and c, both samples were removed from the glovebox and allowed to sit in the atmosphere exposed to air and humidity for 24 hours. The XPS spectra in Figure 2.11c and d were then taken. This amount of exposure was done as an extreme case, as at most the samples in this dissertation were exposed to air for 10 minutes during transfer.

Examining the XPS data after air exposure, it is apparent that there are not major changes to the samples. The 15 mC deposited sample saw an increase in the amount of oxide present and a decrease in the amount of Mg, which may indicate oxidation of Mn by the atmosphere. There was a small amount of this effect seen in the 5 mC sample, but very minor. However, this oxidation does not significantly alter our analysis or conclusions – air exposure cannot account for the $Mg(OH)_2$ formation according to these results. Additionally, this Mn oxidation would in fact make our expected results less pronounced if the Mg ions diffuse into the bulk of the MnO_2 and away from the surface upon air exposure. While not shown here, the binding energies of the Mg 1s regions did not shift more than 0.2 eV after air exposure, which is within the margin of error and confirms the stability of the $Mg(OH)_2$ layer upon air exposure. Detailed atomic composition results are shown in Table 2-5.

Table 2-5. Atomic composition results determined from XPS for MnO_2 samples before and after air exposure

	% Composition							
			O 1s			C 1s		
	Mg 1s	Mn 2p	H_2O/C-O/ClO_4^-	OH/C=O	O^{2-}	C-C/C-H	COOR	C-O
15 mC AD-MnO_2, CA	8.2	1.2	21.6	23.9	0.4	28.1	5.2	7.4
15 mC AD-MnO_2, CA (air)	5.9	4.6	22.2	21.3	4.5	27.0	5.7	3.4
5 mC AD-MnO_2, CA	12.1	2.8	11.5	31.2	2.4	24.0	6.3	7.5
5 mC AD-MnO_2, CA (air)	11.9	3.9	11.7	30.6	3.8	22.9	5.7	7.4

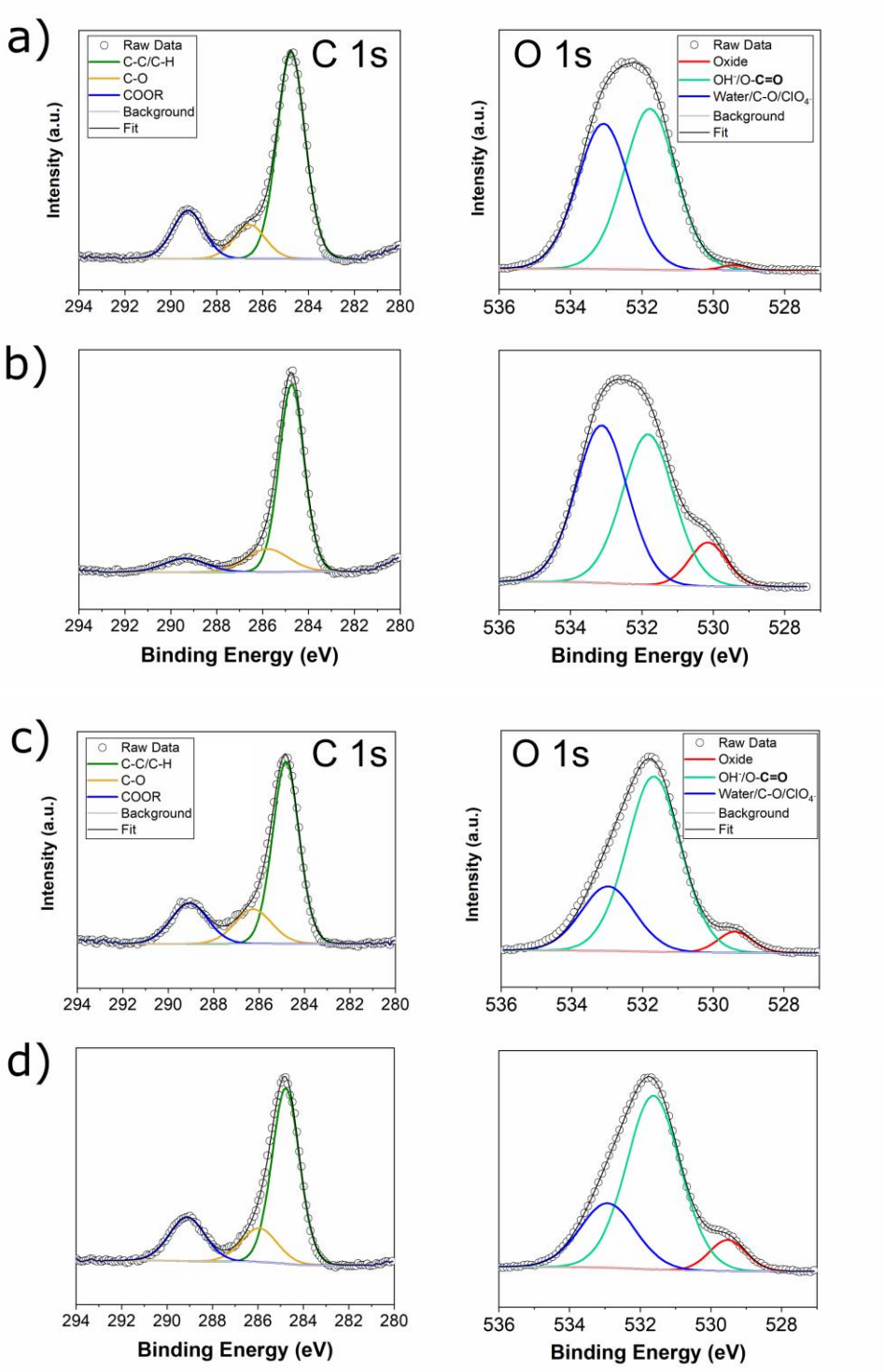

Figure 2.11 XPS results for O 1s and C 1s regions of two MnO_2 samples discharged using CA tested before and after air exposure. a) 15 mC MnO_2 deposited and discharged, XPS taken with no air exposure b) same sample from (a) after 24 hours of air exposure c) 5 mC MnO_2 deposited and discharged, XPS taken with no air exposure d) same sample from (c) after 24 hours of air exposure.

2.4. Conclusions

The mechanism of charge storage was elucidated for amorphous, electrodeposited MnO_2 in water-containing $Mg(ClO_4)_2$/PC electrolyte. The electrochemical experiments coupled with surface, angle-resolved, and depth-profiling XPS analysis demonstrated the formation of a $Mg(OH)_2$ layer on the surface of discharged electrodes in addition to Mg^{2+} insertion into the bulk of the MnO_2 film. The $Mg(OH)_2$ formation was found to be present both during the water activation process and when cycling pre-activated electrodes in dry electrolyte. This layer's formation is reversible, as demonstrated by its disappearance upon charging, and is attributed to the reaction of Mg with water either within the MnO_2 structure or the electrolyte. These findings verify the importance of water to the increased performance of amorphous MnO_2 cathodes, and stress that water needs to be present in some form to enhance the Mg-ion capacity. Importantly, the water was observed to not only screen the charge of Mg^{2+} to facilitate insertion, but also contributed to a chemical conversion at the cathode.

.

Chapter 3: Influence of conductive polymer layers on MnO_2 cathode performance and charge storage mechanism

3.1. Introduction

In the previous chapter, MnO_2 was demonstrated as a potential cathode material for RMB upon the addition of water into organic electrolyte. Water can stay within the structure to enable Mg^{2+} insertion even in a dry electrolyte, and the electrochemical charge storage mechanism is proposed to be a combination of Mg^{2+} insertion and a reversible conversion reaction forming $Mg(OH)_2$ at the MnO_2 surface. This understanding of the MnO_2 reactivity is important, but the performance of this cathode can still be improved. One disadvantage of MnO_2 is that it has a relatively low electronic conductivity.[117, 118] Poor electronic conductivity can cause a large potential drop along the length of the NWs, which may cause decreased material utilization especially at higher current densities.[105, 119] Also, a well-known issue for MnO_2 cathodes is that there is the possibility of Mn dissolution during cycling, where even a small amount of Mn loss can cause significant capacity decay due to its alteration of the MnO_2 surface chemistry.[120] As previously mentioned, Mg^{2+} has poor kinetics in many solid materials, meaning protective layers at the cathode may also impede Mg insertion. If Mg^{2+} can insert into the core MnO_2 through a layer engineered on the surface, it will be a step forward for understanding the capability for cathode protection. To potentially address both of these issues, the research in this chapter investigates a previously established co-electrodeposition method to synthesis coaxial PEDOT/MnO_2 nanowires as a test-bed structure for Mg^{2+} insertion.[104, 121] PEDOT is a well-studied conductive polymer,[122] which in the coaxial structure will deposit on the outside of the

MnO_2 core to provide electron pathways along the length of the NW while also encapsulating the MnO_2.

When utilizing nanostructured materials as battery cathodes, another important part of the charge storage mechanism is understanding the contributions to charge storage from diffusion-limited reactions versus surface-dominant capacitive or pseudocapacitive reactions. Diffusion-limited reactions include the intercalation reactions of Mg^{2+} into the bulk MnO_2, which is kinetically much slower than the capacitive and pseudocapacitive reactions. The latter two charge storage types differ from insertion reactions in that they are dependent on the surface area of the electrode materials. While capacitive charge storage is the electrical energy that is stored via ion adsorption/desorption in the electrical double layer, pseudocapacitance involves fast, surface electron-transfer reactions that are most commonly found in nanostructured electrodes. When materials are nanostructured, their surface area is greatly increased. As the surface area increases in redox-capable cathode materials, more of the charge can be stored due to surface redox reactions, not just capacitive charge. These different diffusion-limited and surface-dominant contributions can be mathematically deconvoluted using two different methods, which will be referred to as Trasatti's[123] and Dunn's methods.[124] These methods will be discussed in detail in Section 3.3.3.

The different contributions to charge storage have not been widely investigated in nanostructured MnO_2 materials for RMB. Many studies of MnO_2 as supercapacitor electrodes have demonstrated the utility of these calculations in determining how charge is stored,[103, 125] but there are few studies of MnO_2 as cathodes for RMB. A recent study of λ-MnO_2 nanoparticles demonstrated that smaller particles (80 nm) have

increased diffusion-limited charge storage compared to large particles (800 nm) and had larger capacity overall, demonstrating the importance of understanding how the mechanism may affect performance of different nanostructured electrodes.[116] The work in this chapter will address this gap in understanding of MnO_2 cathodes as RMB materials, and investigate the charge storage mechanism of MnO_2 in 1D nanowires and how the surface PEDOT layer affects the charge storage. Using electrochemical characterization in conjunction with microscopy and elemental analysis, we will report the influence of the PEDOT conductive polymer on the Mg^{2+} insertion into MnO_2 and the contributions from diffusion-limited and surface-dominant processes.

3.2. Experimental Methods

3.2.1. Nanowire Electrodeposition

The MnO_2/PEDOT coaxial nanowires were synthesized using a previously published procedure,[121] which is described briefly here. First, 300 nm thick gold (Au) was sputtered on the branched side of a Whatman AAO template, with 200 nm diameter pores, as a current collector using a Denton Desk III sputter coater. Copper tape with conductive adhesive (3M) was then attached to the Au sputtered side of the AAO as a contact for electrodeposition. The ordered pores were exposed to the electrolyte solution. The electrode was sealed between two layers of parafilm with an exposed circular area punched out to define the electroactive area (0.32 cm^2) and sealed using a heat gun. The electrodeposition was performed in a three-electrode cell, with Ag/AgCl as the reference electrode, Pt foil as the counter electrode, and the AAO as the working electrode. The electrodeposition solution contained 10 mM Mn acetate tetrahydrate,

80 mM 3,4-ethylenedioxythiophene (EDOT), 100 mM $LiClO_4$, and 140 mM sodium dodecyl sulfate (SDS) dissolved in Millipore water. As previously reported, the thickness of the PEDOT shell was altered by depositing at different constant voltages. Here, voltages of 0.67, 0.70, 0.75, and 0.80 V vs. Ag/AgCl were used. Pure MnO_2 nanowires were deposited at 0.60 V vs. Ag/AgCl in 0.1 M Mn acetate tetrahydrate in Millipore water.

3.2.2. Electrochemical Measurement

All the electrochemical measurements were performed in a three-electrode cell with MnO_2 or coaxial nanowires as the working electrode, Pt foil as the counter electrode, and Ag/AgCl as the reference electrode, except for the GV cycling where activated carbon cloth (ACC) as used as the counter electrode. The electrolyte was 0.1 M $Mg(ClO_4)_2 \cdot 6H_2O$/PC, with a voltage window of -0.4 to 1.1 V vs. Ag/AgCl for CV and -0.4 to 1.15 V for GV. For the charge storage mechanism analysis, scan rates of 0.2, 0.3, 0.3, 0.8, 1, 2, 3, 5, 10, 20, and 40 mV/s were run. Each electrode was activated for 10 cycles by cycling the electrodes from -0.4 to 1.1 V vs. Ag/AgCl in 0.1 M $Mg(ClO_4)_2 \cdot 6H_2O$/PC before performing the CV with different scan rates and before GV power performance testing. The current densities used for the GV of both MnO_2 and coaxial PEDOT/MnO_2 samples will be specified within the text in this chapter.

3.2.3. Electron Microscopy Characterization

Samples for SEM were mounted with the gold side down on conductive carbon tape. The AAO was removed with 3 M NaOH for 20 minutes, then rinsed 3 times with Millipore water. Cycled samples were soaked in PC and water (2 times in each solvent)

to remove salt and electrolyte residue before being gently scraped from the parafilm and mounted on the conductive carbon. For TEM analysis, the AAO was removed from the parafilm after electrodeposition of the active material. The gold current collector was scraped off using sandpaper, and then the whole AAO was dissolved in 3 M NaOH solution. The NaOH was replaced with water and the nanowires were rinsed with Millipore water as many times as needed to achieve a neutral pH, indicating removal of all NaOH (~10 times). The nanowires were then dispersed in ethanol, and 6 μL was dropped onto a lacey carbon TEM grid and dried at 60 °C for 1 hour before analysis.

3.2.4. Raman Spectroscopy

Raman samples were left sealed in the parafilm electrodes after removal of the AAO, and spectra were taken of both pristine and electrochemically treated MnO_2 and coaxial structures. Raman spectra were collected on a Horiba Jobin Yvon LabRam ARAMIS instrument with a 532 nm laser and ~ 1 μm^2 spot size. MnO_2 spectra were collected with a spectral window of 300 to 900 cm^{-1}, while coaxial PEDOT/MnO_2 were collected with a window of 100 to 2500 cm^{-1}.

3.2.5. ICP-AES Analysis

ICP-AES analysis was collected using a Shimadzu ICPE-9000. Samples for ICP analysis were digested in concentrated aqua regia (3:1 HCl:HNO_3) solution for 1 hour for pure MnO_2 nanowires, while coaxial PEDOT/MnO_2 samples were digested for at least 3 hours. For coaxial samples, only the MnO_2 portion was dissolved while PEDOT remained on the parafilm electrode. Samples were diluted to 100 mL in volumetric

flasks with Millipore water, giving final acid concentrations of 2% nitric acid and 2.7% hydrochloric acid. Standards for calibration curves were prepared using an Inorganic Ventures multi-element standard, traceable to NIST standard reference materials. The wavelengths used for analysis were 279.553 nm for Mg, and 257.610 nm for Mn.

3.3. Results and Discussion

3.3.1. Deposition of Coaxial Nanowires

The PEDOT/MnO_2 coaxial nanowire synthesis was previously developed and published by Dr. Ran Liu as an ideal structure for supercapacitors.[121] For this work, the published protocol was repeated to achieve the coaxial nanostructures at deposition voltages of 0.70 V, 0.75 V, and 0.80 V vs. Ag/AgCl. An additional coaxial nanowire structure was also deposited at 0.67 V to achieve a structure with thinner PEDOT than the 0.70 V sample. A TEM image of the 0.67 V structure is depicted in Figure 3.1a, where the porous structure of MnO_2 can be seen with a thin layer of PEDOT on the surface, less than 10 nm in thickness. EDS mapping was performed, and an EDS spectrum was extracted from this data. However, due to the low S content, the S signal from the EDS was below the threshold of the TEM software and neither an individual map of the S signal nor a line scan could be created. As a rough comparison, the Mn/S ratio able to be calculated from the EDS for 0.67 V was ~10, where the published Mn/S ratios for 0.70 V and 0.75 V were 9 and 1.05, respectively.[104] These ratios indicate the higher amount of Mn at 0.67 V, although it is very close to the composition of the 0.70 V sample. On the other hand, a line scan was able to be created for the 0.75 V sample in Figure 3.1c due to the much higher proportion of PEDOT, and therefore S signal

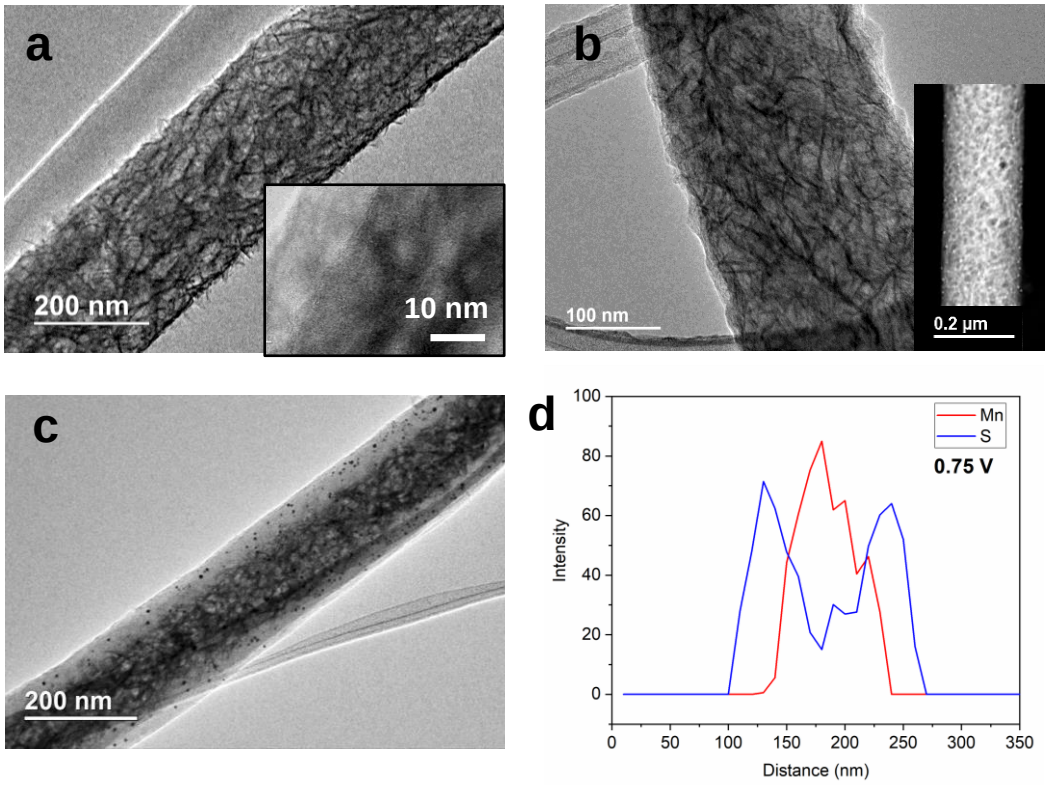

Figure 3.1 TEM images of coaxial nanowires deposited at a) 0.67 V b) 0.70 V with an HAADF image in the inset, c) 0.75 V, and d) EDS line scan of the 0.75 V sample.

intensity. The coaxial structure is apparent for the 0.75 V sample, showing the reproducibility of the coaxial NW synthesis.

3.3.2. Cyclic Voltammetry and Confirmation of Mg^{2+} insertion

After depositing the coaxial NWs, it first needed to be determined whether Mg^{2+} ions could insert into the MnO_2 through the outer PEDOT layer. Previous investigations of the PEDOT/MnO_2 coaxial structures discovered that the PEDOT layer is relatively porous,[104] so it was hypothesized that Mg insertion would not be an issue. To assess the Mg^{2+} insertion capability, CV of the coaxial electrodes was conducted in 0.1 M $Mg(ClO_4)_2 \cdot 6H_2O$ PC. As discussed in Chapter 2, water is necessary for Mg^{2+} insertion into MnO_2, and this is still the case for the coaxial structure. This hydrated electrolyte

is used for all electrochemistry in this chapter. Three CVs representative of different PEDOT thicknesses are depicted in Figure 3.2 to give an overview of how PEDOT affects the Mg^{2+} insertion. CVs of other samples will be provided later in this chapter, but for comparison samples deposited at 0.67 V have a PEDOT thickness of < 10 nm and 0.75 V samples have PEDOT layers ~45 nm thick.

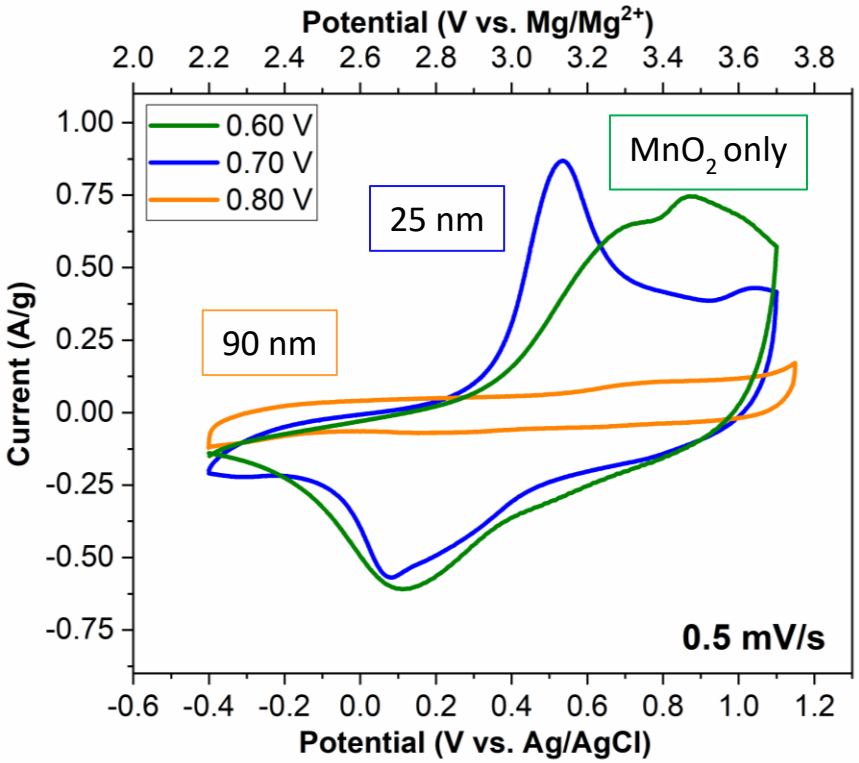

Figure 3.2 Cyclic voltammetry of pure MnO_2 and PEDOT/MnO_2 coaxial nanowires at varied deposition potentials.

As a control sample, pure MnO_2 was deposited and is the green curve in Figure 3.2. The peaks are broad, but there are still peaks for both oxidation and reduction of Mn that occurs upon extraction and insertion of Mg^{2+}, respectively. In blue, the 0.70 V coaxial NW sample with a mid-range thickness of PEDOT, about 25 nm, shows a much sharper oxidation peak than pure MnO_2 around 0.5 V and a reduction peak at 0.1 V, which is a comparable potential to pure MnO_2. There is smaller peak separation

for the 0.70 V coaxial sample with PEDOT compared to pure MnO_2, which has a broad oxidation peak around 0.8 V. The sharper peak and smaller peak separation for the coaxial NW are likely due to the increased electronic conductivity provided by the PEDOT along the length of the NW. Although Mg can insert into MnO_2 through the PEDOT layer at 0.70 V, when there is much thicker PEDOT it does hinder the Mg^{2+} insertion. The sample deposited at 0.80 V, shown in yellow, is the extreme case where the thickness of PEDOT is ~90 nm. The current response in the CV looks strictly capacitive, with no oxidation and reduction peaks visible. The lack of Mn redox peaks indicated that Mg is not able to intercalate into the inner MnO_2 core.

One common argument is because there is water in the electrolyte, proton insertion may be enabling the Mn redox instead of Mg^{2+} insertion. While EQCM and ICP-AES studies on the electrochemistry of pure MnO_2[75] and the XPS studies in the previous chapter support Mg^{2+} insertion, ICP-AES analysis was also performed on the coaxial NW to further confirm that Mg^{2+} insertion is responsible for the observed electrochemical activity with the added PEDOT layer. For samples deposited at 0.67 V, 0.70 V, and 0.75 V, the Mg/Mn ratio calculated from the ICP elemental analysis is shown in Figure 3.3. The activation process consists of 10 CV cycles at 0.5 mV/s in water-containing electrolyte, and samples that were activated and left in the discharged state are in purple. The Mg/Mn ratios range from 0.45 to 0.50, which correspond to a ~1 electron transfer reaction per MnO_2 unit. This result agrees with the presence of only one set of major oxidation and reduction peaks in the CV curves, indicative of an oxidation state change from Mn^{4+} to Mn^{3+} and vice versa. The capacities calculated from the CV curves in the next section 3.3.3, and later GV curves in section 3.3.4, also

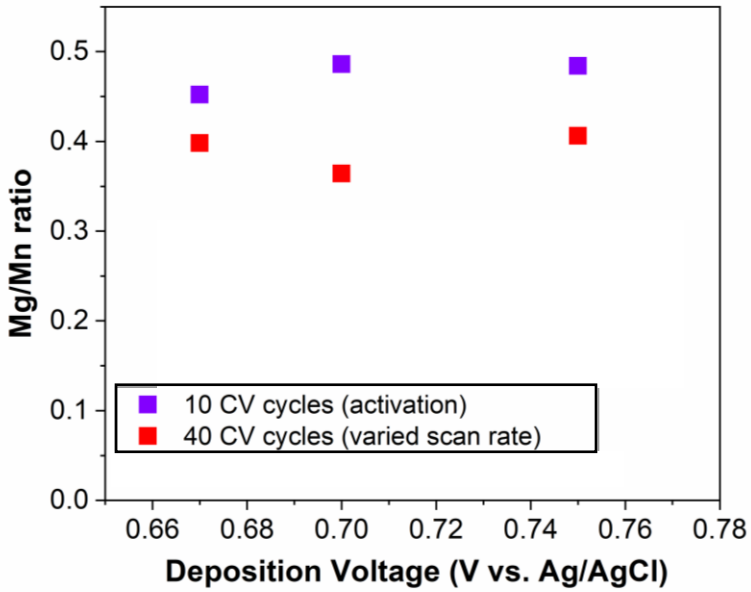

Figure 3.3 ICP-AES analysis of MnO_2 /PEDOT coaxial NW cycles using CV and left in the discharged state.

agree well with these Mg/Mn ratios. As further confirmation, Mg/Mn ratios were reported for coaxial NW samples that underwent longer CV cycling at higher scan rates. These samples with higher scan rates are depicted by the red data points in Figure 3.3 and have a lower Mg/Mn ratio between 0.35 and 0.40. This is expected because Mg cannot fully (de)insert at faster scan rates, so there will be a lower Mg/Mn ratio.

More information about the electrochemical reactions can be determined through closer analysis of the CVs. Figure 3.4 shows the voltammograms for each sample at a slow scan rate of 0.2 mV/s compared with a faster scan rate, 1 mV/s. An important property in CV analysis is the peak separation of the oxidation and reduction peaks. These are typically relatively widely separated in battery cathode materials[126] which is very different from ideal, reversible electrochemical redox couples which follow Nernstian behavior ($\Delta Ep = 59.1$ mV/n).[127] However, although the peaks for batteries are already widely separated, the peak shifting behavior upon increasing the

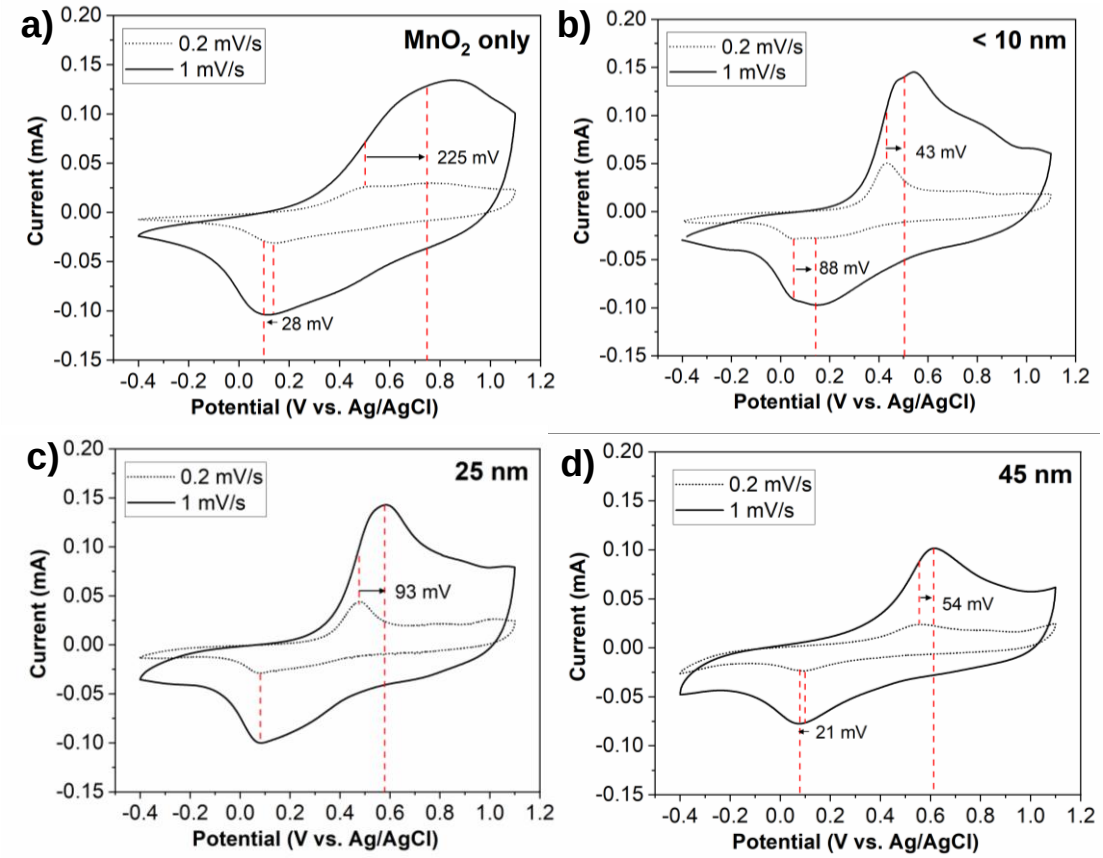

Figure 3.4 Cyclic voltammograms at 0.2 and 1 mV/s illustrating peak current shifts for a) MnO_2 and coaxial NWs deposited at b) 0.67 V, c) 0.70 V, and d) 0.75 V.

scan rate can help discern some of the effects related to electron and ion transport in MnO_2.

As the amount of PEDOT increases, going from pure MnO_2 in Figure 3.4a to 45 nm (0.75 V) PEDOT in d, the extent of peak shifting for the oxidation peak upon increasing the scan rate from 0.2 mV/s to 1 mV/s decreases, with the exception of the 0.67 V sample. For the 0.70 V samples in c, the reduction peak does not shift much in this scan rate range, while for pure MnO_2 and 0.75 V samples in a and d there is a negative shift of the reduction peak potential. An outlier of these trends is the 0.67 sample. This CV is more complicated due to the presence of shoulder peaks, which

makes the peak analysis using EC-Lab more difficult. The overlapping two reduction peaks merge at 1 mV/s, and when the peak analysis is done these two peaks are analyzed as one, making it appear to shift to a more positive potential. Due to this difficulty, the sample for 0.67 V cannot be conclusively analyzed. Better peak fitting analysis outside of EC-Lab could improve the conclusions about peak shifting for this sample. However, the observable trends in the other samples indicate that with more PEDOT, there is a smaller change in peak separation upon increasing the scan rate, while pure MnO_2 has the largest peak separation at 1 mV/s.

In addition to looking at peak shifting, the peak separation at different scan rates for each sample is in Table 3-1. The overall ΔEp is the largest for the sample deposited at 0.75 V at both scan rates, except for the pure MnO_2 sample at 1 mV/s. However, upon increasing the scan rate, the peak separation changes the least for the 0.75 V sample, increasing only 70 mV. Going from 0.2 mV/s to 1 mV/s, ΔEp increases by 93 mV for 0.70 V, 75 mV for 0.75 V, and 253 mV for MnO_2. These results indicate that it is likely the low electronic conductivity and large polarization of the MnO_2 NWs causing the peak shifting at higher scan rates, thus this effect is decreased upon adding the more electronically conducting PEDOT layer. The larger overall ΔEp for the 0.75 V sample compared to the samples with thinner PEDOT (0.67 V and 0.70 V) may be due to the thickness of the PEDOT layer slowing the Mg^{2+} insertion into the core of the NW. This result is different from the pure MnO_2 case where poor electronic conductivity was causing the peak separation. These behaviors deduced from the CV data confirm that material properties and structures are closely intertwined with the

electrochemical reactions. The next section will address the charge storage mechanism of these reactions in more detail.

Table 3-1 Peak separation values for nanowire samples at different scan rates

	ΔEp (mV)	
Sample	0.2 mV/s	1 mV/s
MnO_2	370	623
0.67 V (<10 nm)	367	322
0.70 V (25 nm)	395	488
0.75 V (45 nm)	450	525

3.3.3. Charge Storage Mechanism – Trasatti's and Dunn's Methods

As mentioned in Chapter 1, there are various types of reactions that can occur at the cathodes depending on whether it is intercalation, conversion, or an alloying type material. It was determined in Chapter 2 that MnO_2 has a combination of insertion and conversion reactions in a water-containing Mg electrolyte system. Also characteristic in nanomaterials with high surface area are capacitive and pseudocapacitive contributions to the charge storage. To further understand how much of the charge storage is surface-dominant (capacitive and/or pseudocapacitive) and how much is diffusion-limited (insertion reactions), two different methods were utilized. Both methods rely on the fundamental concept that surface-dominant reactions and diffusion-limited reactions have different kinetics that can be deconvoluted based on their current and charge responses as a function of scan rate.

The first method for separating charge storage contributions utilizes the relationship between peak current and scan rate. This method was introduced by Conway[128] and further explored by Dunn[124]. In a system with both surface-dominant and insertion reactions, the current at any given point in a CV will be a sum of these

two contributions, which can be described by Equation 3.1. In this equation, the current, i, at a given voltage is the sum of surface-dominant contributions (k_1) times the scan rate v and diffusion-limited contributions (k_2) times $v^{1/2}$.

$$i(V) = k_1 v + k_2 v^{1/2} \qquad \text{Equation 3.1}$$

In order to calculate the k_1 and k_2 values, the above equation can be rearranged to provide Equation 3.2. Using this equation, a simple linear fit of a plot of $v^{1/2}$ vs. $i/v^{1/2}$ enables the calculation of the slope (k_1) and the intercept (k_2) for each voltage point.

$$\frac{i(V)}{v^{1/2}} = k_1 v^{1/2} + k_2 \qquad \text{Equation 3.2}$$

This method, which will be referred to as Dunn's method, enables calculation of surface-dominant and insertion contributions at multiple different scan rates. Further, plots can be created from this data to directly visualize the different contributions in a CV. However, this method is often affected by peak-shifting which can cause poor fits of the data. Therefore, a second method is often used to confirm results from Dunn's method and establish conclusions from the data.

The second method for deconvoluting charge storage contributions was proposed by Trasatti and coworkers in a study of RuO_2.[123] Instead of utilizing the dependence of current on scan rate, Trasatti's method is based upon the concept that the charge, Q, of a system is a sum of faster, surface-dominant processes and slower diffusion-limited processes. The different contributions are calculated based on the difference in kinetics for the surface and bulk processes. As the scan rate becomes infinitely fast, or as $v=\infty$, the only processes that can occur are the fast, surface reactions. This value can be calculated from the intercept of the plot of 1/Q vs. $1/v^{1/2}$.

Conversely, at the low end of the theoretical scan rate limit, or v=0, both processes would fully be participating. Thus, the total charge is calculated from the intercept when Q vs. $v^{1/2}$ is plotted. Using these principles, the surface-dominant charge can be calculated at v=∞ and the total charge of the system can be calculated at v=0, while the insertion, diffusion-limited charge is the difference between the two. This method is not susceptible to peak shifting, although the total charge sometimes can be over-estimated as it is extrapolated to an extremely low scan rate. However, this method should give similar results to Dunn's method and give two points of comparison in determining the contributions to charge storage.

Both methods can be utilized to calculate surface and insertion contributions from one set of data, as both need CVs collected for multiple different scan rates. The voltammograms for the four different MnO_2 and coaxial PEDOT/MnO_2 nanowires structures are depicted in Figure 3.5. It is important to note all the nanowires were deposited by passing the same amount of total charge, 200 mC. Qualitatively examining these voltammograms, the effect of PEDOT can be visualized. Comparing Figure 3.5a to b, c, and d, there is an increase in the overall current going from pure MnO_2 to the 0.67 V sample with very thin PEDOT, and 0.70 V and 0.75 V also show higher current at the high scan rate of 20 mV/s. The increased current indicates that with the added PEDOT, the improvement in electron transport likely allows for more uniform Mg insertion and de-insertion and better material utilization along the 10 μm nanowire, especially at very high scan rates. This result is also interesting when considering there is also less MnO_2 content in the NWs with more PEDOT, further highlighting the better utilization of a smaller amount of active MnO_2.

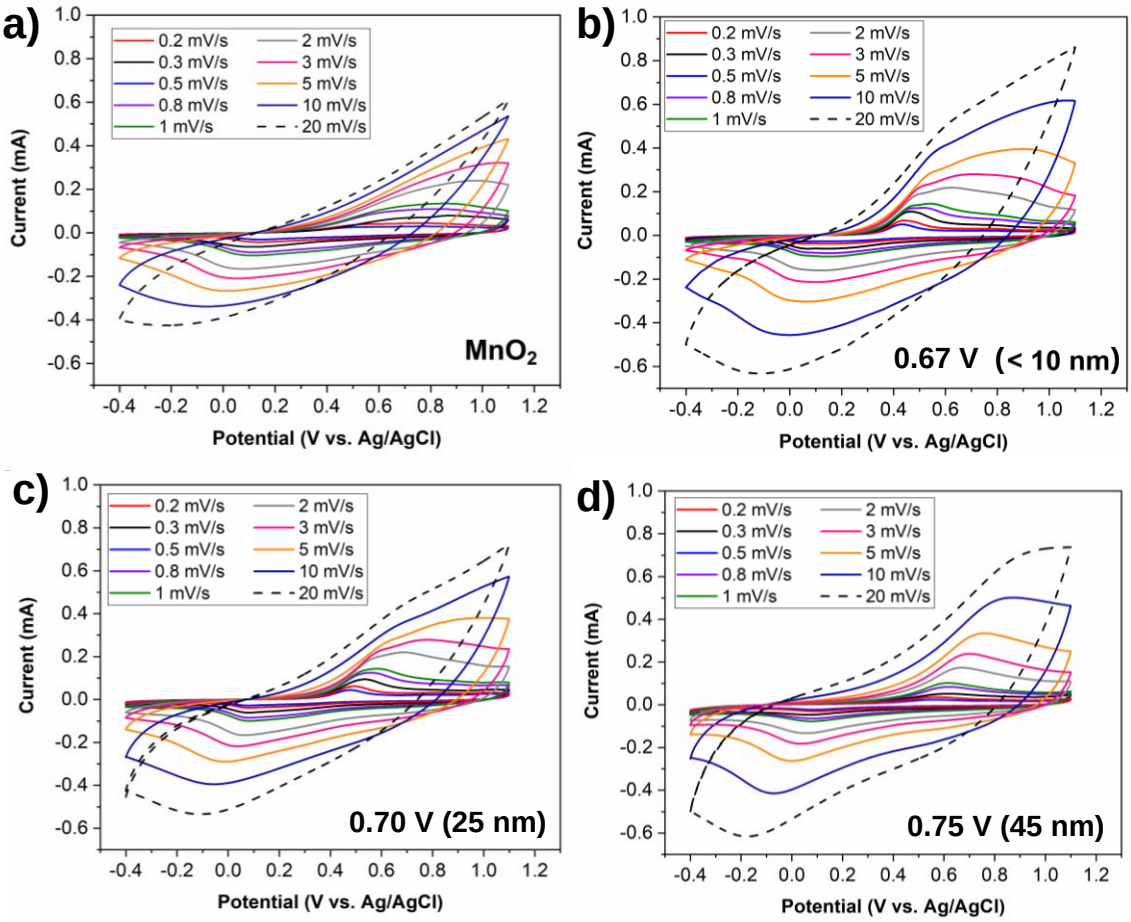

Figure 3.5 Cyclic voltammograms at scan rates of 0.2-20 mV/s for a) MnO_2 and coaxial PEDOT/MnO_2 nanowires deposited at b) 0.67 V, c) 0.70 V and d) 0.75 V.

When examing samples at the scan rates below 20 mV/s, around 2 and 3 mV/s scan rates the maximum peak current values for all samples are about the same. Looking back at Figure 3.4, at 1 mV/s the 0.67 V and 0.70 V samples have the highest current at the lower scan rate of 1 mV/s, with MnO_2 having only a little bit less current, while 0.75 V has the lowest peak current. Due to the lower electronic conductivity of MnO_2 without PEDOT, there is a potential drop from the bottom of the NWs to the top, meaning the MnO_2 furthest from the current collector is not fully utilized without the PEDOT layer. This effect is not as detrimental at lower scan rates, but as the scan rates increase the current for MnO_2 falls behind the others. Further, in Figure 3.5b-d the

reduction peak does not shift out of the voltage window at the fast scan rate of 20 mV/s and does not broaden as much as the MnO_2 sample in a. The oxidation peaks broaden at high scan rates for b and c, but for the 0.75 V sample in d both oxidation and reduction peaks are still visible at 20 mV/s. There is also the possibility that there is a contribution to the capacity from the PEDOT above 0.70 V, which could contribute to the higher current. These qualitative observations build upon the discussion of Figure 3.4 in the previous section, and further demonstrate that the electron transport of PEDOT helps improve the material utilization of MnO_2.

Using this CV data, the contributions from surface-dominant and bulk insertion was calculated using Trasatti's and Dunn's methods. The difference in the charge storage contributions for both discharge (reduction of MnO_2, Mg^{2+} insertion) and charge (oxidation of MnO_2, Mg^{2+} extraction) reactions using both methods are depicted in Figure 3.6. For Dunn's method, due to peak shifting above 1 mV/s, the data from 0.2 to 1 mV/s were used for analysis. The results for the calculated charge contributions at multiple scan rates are in Figure 3.6a-c. At the low scan rate of 0.2 mV/s, all samples have more than 50% of the capacity coming from surface-dominant charge. As the scan rate increases, the percent surface contribution also increases for all electrodes. This result is expected, as with a higher scan rate Mg^{2+} diffusion and its ability to insert is not fast enough, thus the surface-dominant pseudocapacitive reactions are favored. Overall, adding the PEDOT outer layer in the coaxial NWs does not significantly alter the contributions to the charge storage when compared to MnO_2.

The MnO_2 has a higher percent of the capacity coming from surface contributions, particularly upon charging. There are a few possible explanations for this

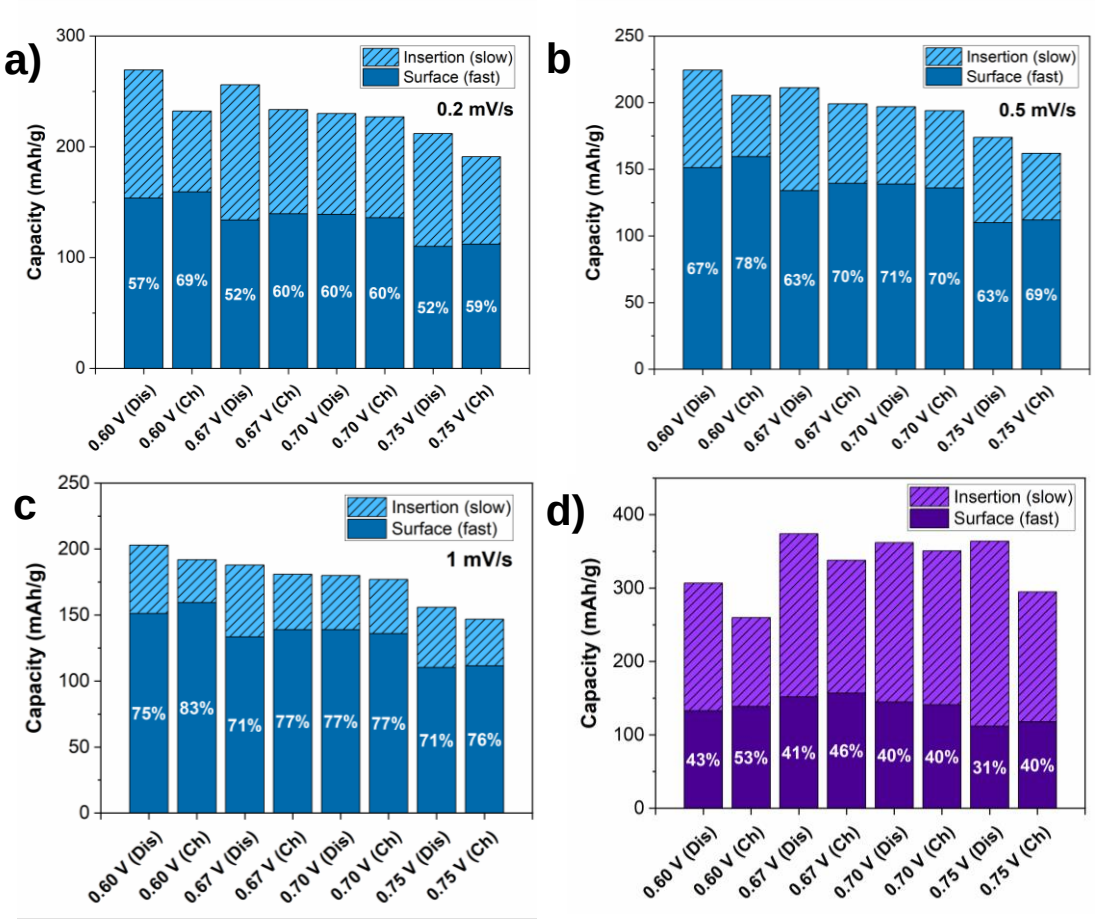

Figure 3.6 Deconvoluted insertion and surface contributions for each type of nanowire, MnO_2 or coaxial PEDOT/MnO_2. The contributions calculated using Dunn's method are demonstrated at different scan rates: a) 0.2 mV/s, b) 0.5 mV/s, and c) 1 mV/s. The contributions calculated from Trasatti's method are shown in d).

difference in surface-dominant and insertion contributions. The primary reasons behind the differences could be due to changes in the structure upon going from a homogeneous MnO_2 NW electrode to a heterogeneous PEDOT/MnO_2 coaxial NW. As the PEDOT thickness increases, the MnO_2 diameter decreases. With a wider diameter, there is a larger distance for the Mg^{2+} ions to penetrate the core for insertion reactions. Therefore, there is possibly more unused MnO_2 at the core of the MnO_2 compared to the coaxial NW structures with smaller diameters. This reaction may cause a higher surface contribution compared to insertion. By this principle, the narrower

PEDOT/MnO_2 coaxial NWs should have a higher percent insertion contribution. However, as the thickness of PEDOT increases, the Mg^{2+} diffusion through the PEDOT into the core of the MnO_2 also becomes more hindered, meaning the surface reactions predominate. If these two different structural effects begin to offset one another, this could explain why there is not much of a change for the percent surface and insertion contributions for the PEDOT/MnO_2 coaxial NWs as the PEDOT thickness increases.

The results from Trasatti's method show similar trends to those from Dunn's method. The percent of the capacity from the different contributions is depicted in Figure 3.6d. As previously mentioned, Trasatti's mathematical approximation of the total capacity at a theoretical scan rate of 0 mV/s can lead to an overestimation of the total capacity. For almost all MnO_2 and coaxial electrodes, the total capacity calculated is over the one-electron theoretical capacity of MnO_2 (308 mAh/g), however it is under the two-electron theoretical capacity (616 mAh/g), which is greater than those calculated via Dunn's method. The trends in surface contributions from Trasatti's agree well with those calculated using Dunn's method, however, due to the higher total capacity estimated using Trasatti's the percent surface contribution for all samples appears lower. Trasatti's method also demonstrates that the charge storage processes remain similar across samples, with little difference caused by the PEDOT layer.

The data used to calculate charge storage contributions using Dunn's method can also be used to create plots of the surface and insertion contributions overlaid with the experimentally collected CVs. The curves for all four MnO_2 and coaxial PEDOT/MnO_2 samples at 1 mV/s are in Figure 3.7. While only the predicted surface contributions are shaded, the areas that lack shading indicate where the insertion

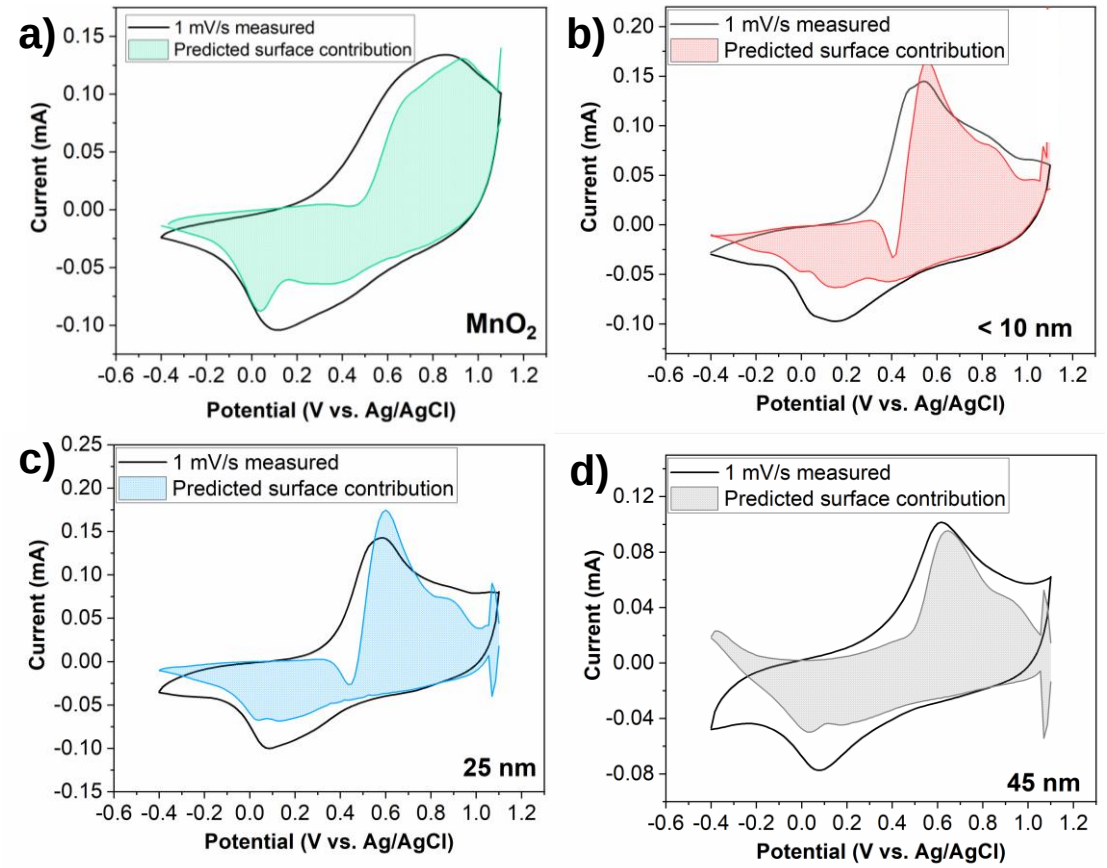

Figure 3.7 Predicted surfaced contributions calculated using Dunn's method at 1 mV/s for a) MnO_2, and PEDOT/MnO_2 coaxial NWs deposited at b) 0.67 V, c) 0.70 V, and d) 0.75 V.

contributions occur. These plots allow a visualization of the potentials at which the redox reactions are occurring. There is an indication that the de-insertion reactions occur around 0.5-0.6 V during the oxidation sweep and the insertion at 0.1-0.2 V during the reduction sweep. These similarities demonstrate that adding the PEDOT layer does not fundamentally change the electrochemical reactions or their oxidation and reduction potentials. The shapes of the shaded regions also show that the surface-dominant reactions do not have a square-shaped current profile indicative of strictly capacitive or double-layer like reactions. The presence of distinct peaks supports a pseudocapacitive charge storage mechanism consistent with faradaic reactions

occurring within MnO_2.[126] Overall, the charge storage deconvolution using Dunn's and Trasatti's methods give further evidence that there is a combination of insertion reactions and surface dominant reactions for MnO_2 and coaxial PEDOT/MnO_2 NWs in a water-containing organic electrolyte system.

3.3.4. Galvanostatic Cycling

In the previous section, the charge storage mechanism of MnO_2 and PEDOT/MnO_2 coaxial NWs was able to be further elucidated using cyclic voltammetry. To test these electrodes for their potential as cathodes for Mg batteries, constant current or galvanostatic (GV) cycling was utilized. Of interest during GV testing is the ability to assess the power performance of the MnO_2 and coaxial electrodes. Due to the increased electronic conductivity along the length of the NWs containing PEDOT, it was hypothesized that the coaxial NWs would perform better at higher current densities than MnO_2 on its own. The current densities were calculated based on the theoretical two-electron transfer capacity of MnO_2, 616 mAh/g. The current densities were calculated based on the mass of MnO_2 after depositing 200 mC of charge, and all electrodes were cycled at the same areal current densities based on nominal electrode area (0.32 cm^2). However, it is important to note that the masses of the coaxial electrodes deposited with the same amount of charge, 200 mC, have different masses than pure MnO_2. This difference is due in part to the higher molar mass of EDOT as well as the lesser amount of MnO_2 in the coaxial nanowires as the deposition voltage is increased. The results of the power performance followed by long-term cycling GV cycling are depicted in Figure 3.8. Also, coulombic efficiency

indicated in this figure is referring to the ratio of charge measured during the discharge and charge processes, which is slightly different to the definition in Chapter 1. For cathodes, coulombic efficiency is discharge capacity/charge capacity x 100%.

The GV cycling data demonstrate that adding the PEDOT layer in the coaxial NWs does affect the power performance and cyclability of the MnO_2. Examining Figure 3.8a, the sample that is MnO_2 with no PEDOT is shown in green and has the second-highest overall initial capacity, ~220 mAh/g. The sample deposited at 0.70 V with 25 nm of PEDOT in blue has slightly higher initial capacity, ~230 mAh/g, while the 0.67 V sample with < 10 nm PEDOT starts off with a capacity of ~200 mAh/g but increases over the first 5 cycles to 210 mAh/g. This increase may be due to some activation with water in the electrolyte still occurring, even though all samples were

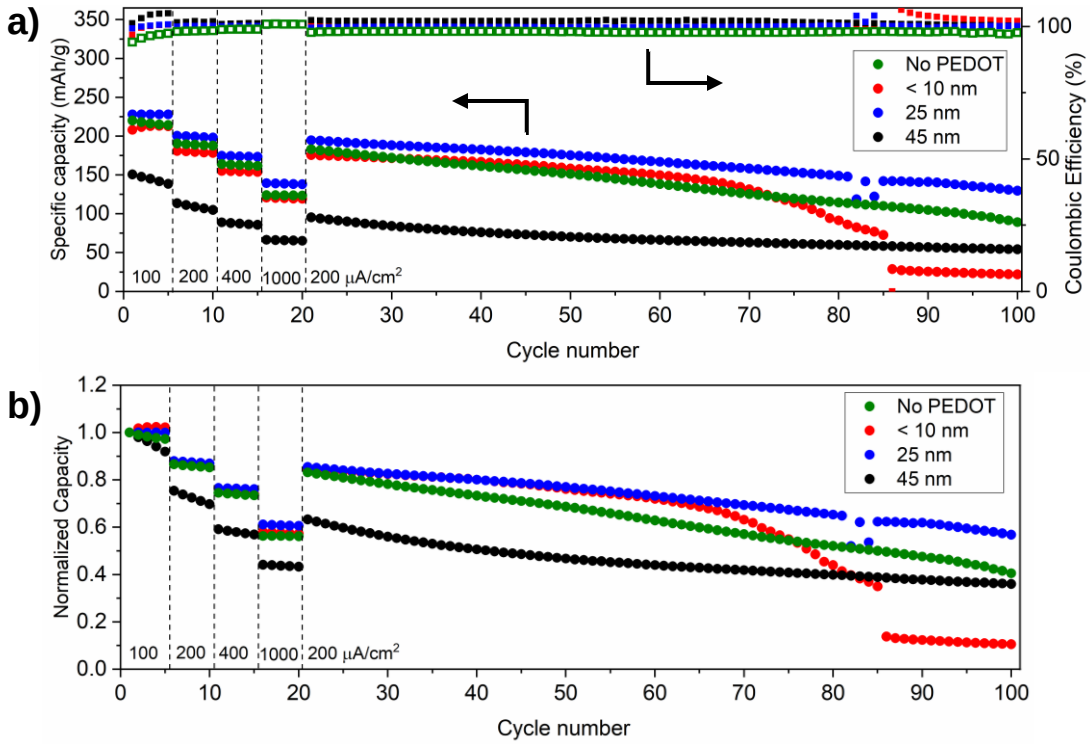

Figure 3.8 Galvanostatic charge and discharge cycling for MnO_2 and PEDOT/MnO_2 coaxial NWs. The data shown in a) are normalized to the entire mass of the active material, while b) is normalized to the first cycle capacity (100 μA/cm^2).

cycled for 10 CV cycles to activate them before GV cycling. The 0.75 V coaxial sample with the thickest PEDOT has the lowest initial capacity of 150 mAh/g, which is expected due to the decreased amount of MnO_2 deposited in these samples. Overall, the 25 nm sample retains the highest capacity for the longest, followed by the pure MnO_2 sample. The 0.67 V sample performs well for the first 60 cycles but has a sharp decrease beyond 70 cycles. There is not a clear reason for this behavior, but it was reproducible and seen for more than one sample. Similar behavior was seen in some MnO_2 samples also, though not all, but was not seen in any of the 0.70 V or 0.75 V samples. It could be a result of a contact issue with the electrodes, or a point at which there was some large number of NWs that became disconnected or fell off the gold current collector. The latter may be why samples with more PEDOT did not have this issue – the polymer was able to add structural and mechanical stability to the electrodes. Lastly, the 0.75 V sample has a sharp decrease in capacity over the first 10 cycles, but then levels off and remains the most stable throughout the long cycling at 200 $\mu A/cm^2$.

The bottom graph, Figure 3.8b, shows the same data from Figure 3.8a normalized to the first cycle capacity to make the power performance data easier to compare. The 0.75 V sample from the beginning has the worst power performance, losing almost 56% of its capacity going from 100 A/cm^2 to 1 mA/cm^2. The 0.70 V sample in blue performs the best, even at high current, losing 39% of its initial capacity while the 0.67 V sample lost 42% and the MnO_2 sample lost 44%. The 0.75 V sample with the thickest PEDOT likely loses the most capacity due to the limitation of Mg^{2+} diffusion through the PEDOT at higher current densities. The sharp decrease in capacity over the long-term cycling is more apparent for the MnO_2 shown in green,

which after 100 cycles loses 60% of its initial capacity like the 0.75 V sample. The 0.70 V sample in blue does not have as severe of a capacity drop and loses ~40% of its initial capacity after 100 cycles. Overall, PEDOT helps improves power performance by increasing electronic conductivity, although it becomes a barrier to Mg^{2+} transport at thicknesses greater than 25 nm. This observation is supported by the Trasatti's and Dunn's method analysis that shows the percent contributions do not change significantly, possibly indicating a balance between increased electron transport and decreased ion transport. The sample with the best performance is 0.70 V, where there is a balance between the thickness of PEDOT and the improved electronic conductivity.

To gain further understanding of the effect of the charge storage mechanism on the cathodes' performance, the same samples were cycled at lower current densities. The Trasatti's and Dunn's method data suggest that at lower scan rates, and similarly lower current densities, insertion behavior predominates over surface reactions. In Figure 3.9a and b, the GV performance of coaxial PEDOT/MnO_2 NWs at different current densities are normalized to the mass and 50 $\mu A/cm^2$ first cycle capacities, respectively. The specific capacities in Figure 3.9a agree well with those in Figure 3.8 at the same current densities, and the power performance shows the same trends in Figure 3.9b, with 0.67 and 0.70 V samples performing similarly and 0.75 V not maintaining capacity at higher current densities. The major difference appears during the long-term cycling at 100 $\mu A/cm^2$, half of the current density used in Figure 3.8. The 0.67 V coaxial NW shows a sharp decrease in capacity after only 45 total cycles. The 0.70 V sample lasts longer, about 75 cycles, before also showing a sharp drop in capacity. The 0.75 sample shows a more gradual decrease in capacity, and has the

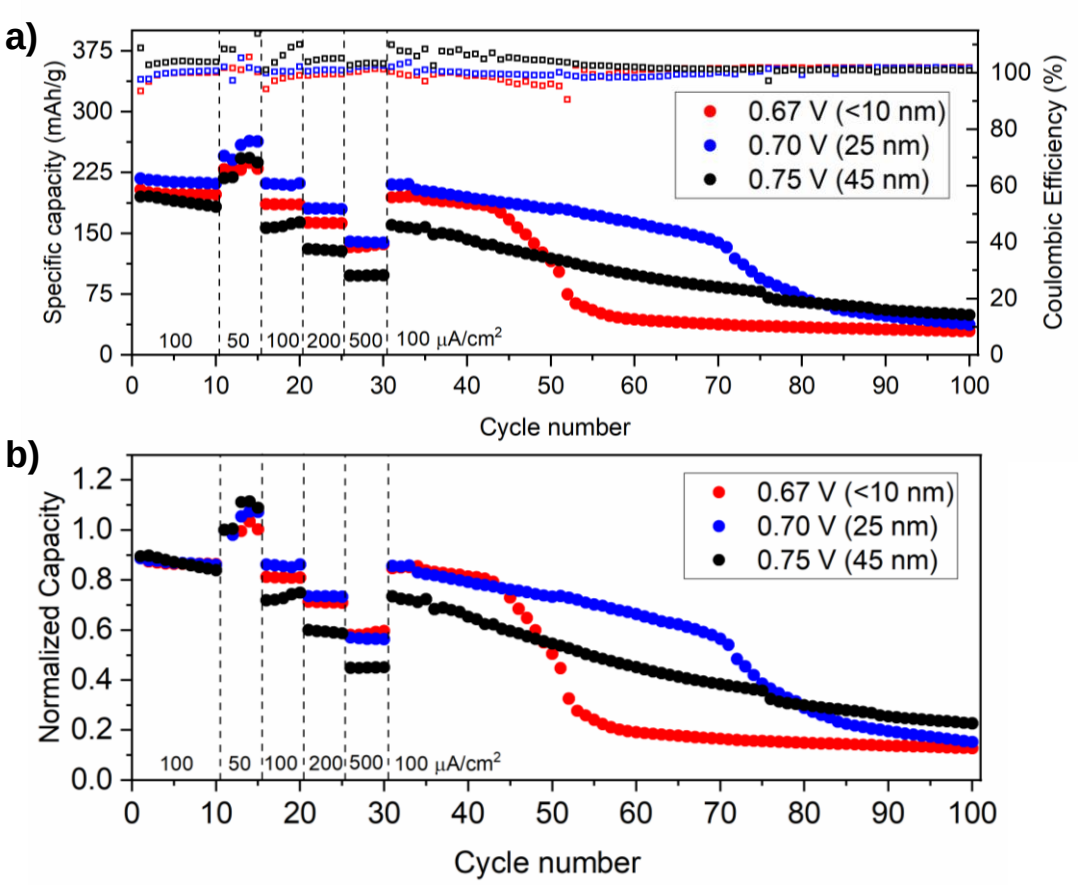

Figure 3.9 Galvanostatic cycling at lower current densities.

highest capacity after 100 cycles, although only by a small margin and all samples have a capacity of less than 50 mAh/g. The differences in performance at high and low current density likely indicate how the overall performance is affected by the charge storage mechanism, and how the ion insertion or conversion reactions influence the cathodes' cyclability. These effects will be further discussed in the next section.

The effect of current density of MnO_2 electrodes without PEDOT was also explored. In Figure 3.10, two MnO_2 electrodes were cycled at two different current densities, 1C and 1.5 C (200 and 300 μA/cm^2). The sample cycled at 1 C has a higher capacity initially, which is expected due to the better material utilization at a lower current density. However, the capacity drops off significantly over 100 cycles, retaining

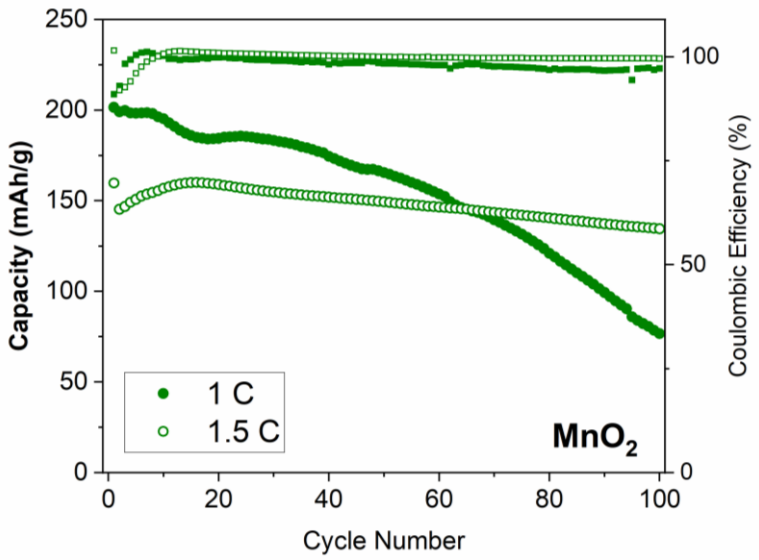

Figure 3.10 Capacities over 100 cycles for MnO_2 electrodes cycled at 1 C and 1.5 C.

only 38% of its capacity. On the other hand, the sample cycled at 1.5 C is much more stable over 100 cycles and retains 84% of its initial capacity. The sample at 1.5 C also has better coulombic efficiency, which may be an indicator for its superior performance – at 1 C, if more inserted Mg is stuck in the structure each cycle, there would be less capacity on the next discharge, leading to a lower coulombic efficiency. The possible reasons for the degradation based on the charge storage processes are addressed next.

3.3.5. Possible Degradation Mechanisms of MnO_2

Both MnO_2 and PEDOT/MnO_2 coaxial nanowires demonstrate decreases in capacity over long-term cycling. One common cause of degradation in manganese oxide cathodes is dissolution of Mn at the surface.[120] These interfacial changes have been determined to affect the phase stability over cycling of spinel $LiMn_2O_4$ in Li systems,[129] although the effects have not been very well-studied in cathodes for RMB. To track differences in both Mg and Mn content in the different electrode structures,

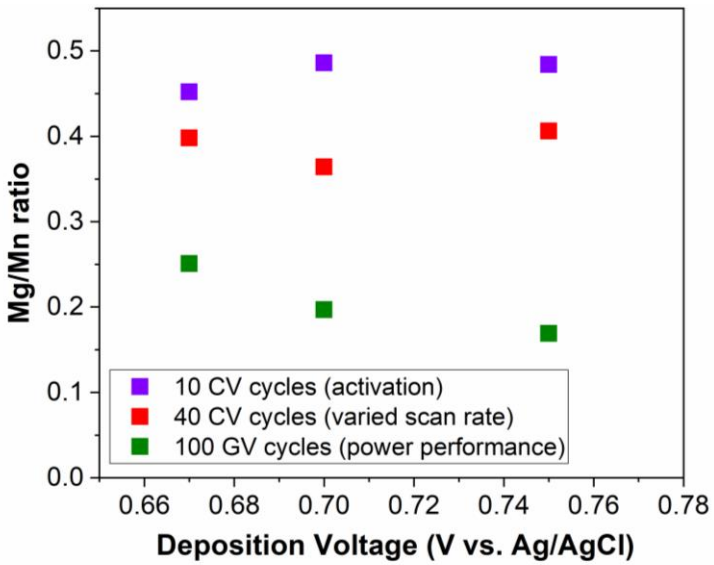

Figure 3.11 ICP-AES analysis of MnO_2 /PEDOT coaxial NW cycled using CV and GV and left in the discharged state.

ICP-AES was utilized. The Mg/Mn ratio of different electrode samples left in their discharged state after GV testing is shown in Figure 3.11, which also includes data from Figure 3.3, repeated here for easy comparison. The GV data for each electrode, shown in green, are the same samples cycled at low current density in Figure 3.9. It is apparent that the samples cycled by GV have a lower Mg/Mn ratio than those cycled using CV, which indicates that less Mg^{2+} is inserted per Mn unit. This trend makes sense considering that the capacity is dropping significantly over time, meaning less charge is being stored and therefore less Mg^{2+} should be present.

However, if the capacity is calculated based on the amount of Mg^{2+} detected by ICP-AES, the expected capacities would be ~154 mAh/g (0.25 Mg/Mn) for 0.67 V, 123 mAh/g (0.20 Mg/Mn) for 0.70 V, and 92 mAh/g for 0.75 V (0.15 Mg/Mn), based on a theoretical one-electron transfer capacity of 308 mAh/g for MnO_2 (0.5 Mg/Mn). These theoretical capacities are much higher than the experimentally observed capacities in Figure 3.9, which indicates that there is Mg trapped in the structure that is

not being reversibly inserted and extracted. This theory of Mg^{2+} trapping is supported by the XPS depth profiles in the previous chapter, which shows about 0.1 Mg/Mn in the bulk of the MnO_2 thin film upon charging (Figure 2.7). The trapping of Mg^{2+} in addition to interface affects from Mn dissolution may account for the capacity fading.

ICP-AES was used to compare the masses of MnO_2 for the different electrode compositions to give more insight into the possible Mn dissolution. In Figure 3.12, the calculated values for all electrodes are generally the highest, as they assume that all the electrons transferred during the electrodeposition go to the oxidation of Mn^{2+} to Mn^{4+}, and in most cases the as-deposited masses agree well with those calculated based on the charge passed. The as-deposited masses had the smallest standard deviation for pure MnO_2, while all coaxial samples had some variation. These differences are due to small variations in the relative thickness of the PEDOT layer and amount of MnO_2 in the core. For pure MnO_2, there is a decrease in amount of MnO_2 upon cycling via CV, and

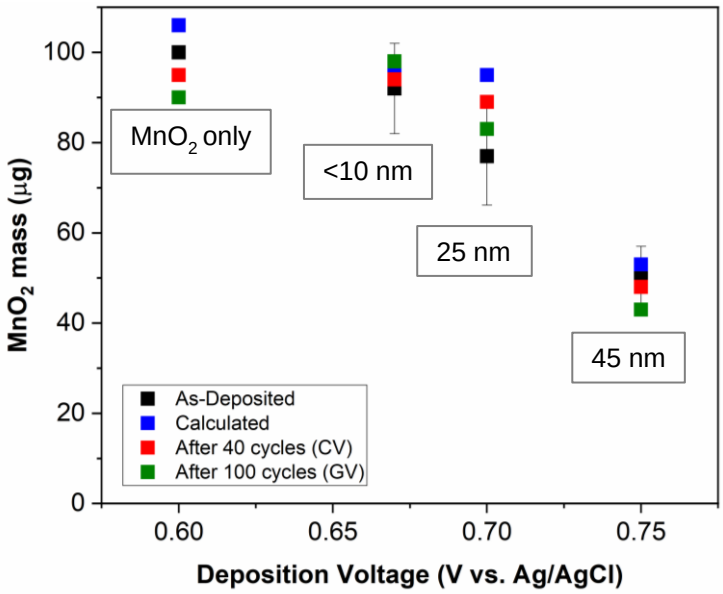

Figure 3.12 Mass of MnO_2 in all electrodes, including theoretically calculated values, pristine electrodes, and Mn content of cycled electrodes (both CV and GV) analyzed using ICP-AES. Error bars indicate standard deviations of as-deposited samples.

then even more for GV, about 5% and 10% of the total mass, respectively. While that general trend is also noticeable for the coaxial samples, it is difficult to definitively say this is due to Mn loss instead of just sample variation because the values fall within the standard deviation. The loss seen in the MnO_2 only NW is consistent with previous results that show this small amount (~5%) of Mn dissolution can cause significant capacity fade.[120] Therefore, we tentatively propose that Mn dissolution combined with Mg trapping within the structure are responsible for the capacity loss over time.

3.4. Conclusions

The combination of structure, materials' properties, and the charge storage mechanism are critical factors in the MnO_2 cathode's performance in a Mg battery system. Mg^{2+} ions were determined to be able to insert into the MnO_2 core of PEDOT/MnO_2 coaxial nanowires. Further, the charge storage mechanism of MnO_2 and coaxial structures was found to be largely surface-dominant, although there is increased contribution from insertion processes at slow scan rates and low current densities. The presence of a PEDOT layer at the surface did not significantly alter the charge storage mechanism, but the added electronic conductivity helped increase material utilization along the length of the nanowires and improve power performance. Electrodes did exhibit significant capacity decay, and it is proposed that irreversible insertion of Mg in addition to Mn dissolution may be responsible, though further experiments may be needed to fully support the latter claim. These fundamental understandings of Mg^{2+} reactions and properties of the MnO_2 cathode are important for informing what types of materials, structures, and electrolyte systems will be ideal for next generation RMB.

Chapter 4: Effect of aluminum oxide ALD coatings on magnesium anode surface reactions

4.1. Introduction

The previous two chapters gave a detailed understanding of the reaction and charge storage mechanisms for electrodeposited MnO_2. While adding water into the electrolyte and a conductive polymer surface layer improve Mg^{2+} insertion/conversion and power performance, helping to mitigate the issue of having a cathode with fast enough Mg^{2+} insertion to demonstrate in a full-cell, this cathode cannot be paired with a Mg metal anode with water in the electrode or electrolyte. Another important thing to note is that the cathode demonstrated good performance in a $Mg(ClO_4)_2$/PC electrolyte, which is not compatible with the Mg metal anode. One solution to both compatibility issues is to create a protection layer on the Mg metal surface to prevent water, electrolyte components, and other potential contaminants from reacting with Mg metal and passivating the electrode. Another advantage of this method is that complex Mg electrolytes would not be needed. The application of protection layers has been extensively studied in Li-ion batteries[130, 131] as well as other battery chemistries such as Na batteries.[132] Protection layers are also called artificial SEI layers, as these interface layers generally serve to protect the anode interface from unwanted reactions by preemptively creating an engineered SEI layer with the desired properties needed to improve the anode's compatibility with the electrolyte as well as its performance.

Aluminum oxide (Al_2O_3) has a very robust and well-known atomic layer deposition (ALD) chemistry.[133] Al_2O_3 has been effective as a protection layer in both Li[134] and

Na[132] metal anode systems, protecting these interfaces from significant electrolyte degradation on the surface and helping prevent the formation of dendrites, which are an issue for both Li and Na. However, utilizing Al_2O_3 for Mg would serve slightly different purposes. While the prevention of the electrolyte degradation is still the major goal, Mg does not have significant dendrite issues. However, Mg has poor diffusion kinetics in most solid materials, so using a protection layer with good Mg mobility that is also electronically insulating is critical. ALD Al_2O_3 could potentially mitigate the poor Mg^{2+} diffusion issue by creating an extremely thin layer. While Mg^{2+} conductivity in Al_2O_3 may be low, if Mg only needs to travel a few nanometers ionic conductance may be sufficient despite low intrinsic Mg^{2+} ionic conductivity. Recent computational work has indicated that $MgAl_2O_4$ has an electrochemical stability window (stable versus reduction and oxidation) of 3.13 V, and suggests that although it is not stable at 0 V vs. Mg/Mg^{2+}, it could exhibit some metastability that would enable it to function as a protective coating.[135] Further, another study demonstrated that $MgAl_2O_4$ has a low migration barrier for Mg^{2+}, calculated to be 491 meV.[136] While ALD deposits non-magnesiated Al_2O_3, if the layer can be magnesiated to $MgAl_2O_4$ the results from this computational work are encouraging.

While the ultimate goal of Mg anode protection is to utilize $Mg(ClO_4)_2$/PC based electrolyte in a full-cell, some other simple salt-based electrolytes are common in the literature that are more compatible with Mg metal but also have room to improve their interfacial characteristics. At the time this work was initiated, the understanding of magnesium bis(trifluoromethanesulfonyl imide) ($Mg(TFSI)_2$) in ether electrolytes was relatively unexplored. $Mg(TFSI)_2$ in a mix of 1,2-dimethoxyethane (DME) and

diglyme was first demonstrated as an electrolyte for RMB in 2014.[51] Further studies of $Mg(TFSI)_2$/DME electrolyte demonstrated that there was a high overpotential for both Mg deposition (0.6 V) and stripping (1.5 V) using this electrolyte.[52] Regarding Mg deposition and stripping via CV, thermodynamically reduction (deposition) should occur once the potential of the system is scanned below 0 V vs. Mg/Mg^{2+}, while oxidation (stripping) should occur above 0 V vs. Mg/Mg^{2+}. The amount of potential required above/below 0 V to induce these reactions is called the overpotential. The high overpotential in $Mg(TFSI)_2$ electrolytes is due to the $TFSI^-$ anion's instability at the Mg anode which causes it to degrade and form MgS as well as MgF_2.[32, 53, 137] While the degradation layer is not completely passivating, it causes large voltage hysteresis issues in full-cell systems.[138] Some work has also proposed that cycling Mg metal in this electrolyte can cause dendrite growth,[32] although the deposits are not long and branch-like so some researchers do not agree with this terminology. However, it is now more well-known that spherical Mg deposits can potentially grow through separators, though they may not deposit as true dendrites.[53]

In this work, to determine if a protection layer can help improve the degradation of $Mg(TFSI)_2$, Al_2O_3 was deposited at different thicknesses on different Mg metal substrates. The surface chemistry, overpotential evolution, impedance, and surface morphology were examined to investigate the effect of the Al_2O_3 layer on Mg deposition and stripping. The goal of this chapter is to demonstrate different methods and substrates that could be utilized to study the potential for ALD materials to be used to protect Mg metal anodes, describe how Al_2O_3 affects the electrochemical properties and surface chemistry, and elucidate properties important for protection layers.

4.2.Experimental Methods

4.2.1. Preparation of Mg metal

The magnesium metal foil used was >99.9% purity, 0.1 mm thick purchased from MTI corporation. Prior to use, all foil was mechanically polished with SiC sandpaper with three grits, going from lowest to highest (600, 1200, and 2000) and then wiped with a Kim Wipe. For use in coin cells, foils were punched out with a hammer-driven punch with the desired diameters, either 3/8" or 1/2". Thermal evaporation was also used to deposit Mg on stainless steel spacers (15 mm diameter, MTI) in a homemade high-vacuum evaporation chamber attached to a glovebox filled with inert Ar to minimize air and moisture exposure. The Mg source for evaporation was Mg ribbon (99.5%, Sigma Aldrich) scraped with a razor blade to remove the surface MgO layer. All Mg preparation, both foil and evaporation, was performed in either MBraun or LC technology gloveboxes with <0.5 ppm H_2O and O_2.

4.2.2. Atomic Layer Deposition

All ALD on Mg metal was performed in a Cambridge Ultratech Fiji reactor attached to an MBraun glovebox with inert Ar, allowing for no exposure to the ambient atmosphere. The Al_2O_3 ALD process used trimethylaluminum (TMA) as the aluminum source and oxygen plasma as the oxidant. The ALD process consisted of a 0.06s TMA pulse, Ar purge, 20s oxygen plasma pulse, and an Ar purge at a reactor temperature of 150 °C, giving a growth rate of ~1 Å/cycle. Approximate thickness of the layers will be indicated in the text.

4.2.3. Electrochemical Testing

All electrochemical tests were performed in 2032 coin cells (MTI) in a symmetric configuration where both electrodes in the two-electrode cell are Mg metal (foil or evaporated). The separators used were glass fiber (Whatman GF-A) and were wet with 125 μL of electrolyte in each test. The electrolyte was 0.25 M $Mg(TFSI)_2$ in 1,2-dimethoxyethane. GV tests were run at constant current for fixed amounts of time (30 min or one hour) alternating positive and negative currents for oxidation and reduction, respectively, to monitor the overpotential. Electrochemical Impedance spectroscopy was performed an a Biologic VMP Potentiostat with 10 mV amplitude between frequencies of 200 kHz-10mHz, either at the OCP or at relevant potential values. Details for EIS voltages, alternative frequency ranges or voltage amplitudes will be indicated in the text.

4.2.4. Characterization

Ex-situ XPS analysis was performed using a Kratos Ultra DLD XPS spectrometer using monochromatic aluminum x-rays. Cases where non-monochromatic magnesium x-rays needed to be used will be specified in the text. Survey spectra and high resolution spectra were collected with pass energies of 160 eV and 20 eV respectively. An argon ion sputter source was employed for depth profiling. The curves were fitted using CasaXPS software. Spectra were processed using a 70%-30% Gaussian-Lorentzian product function and a Shirley-type background.[110]

4.3. Characterization of Bare Mg metal

Before the protection of Mg metal, the surfaces of both Mg metal and evaporated Mg were characterized. The XPS survey spectrum and SEM image of the evaporated Mg surface are depicted in Figure 4.1. The only detectable elements after Mg evaporation are carbon, oxygen, and magnesium. Although the surface contamination layers (typically MgO and $MgCO_3$) were removed as much as possible from the Mg metal used for the evaporation, there is still enough present to deposit with the Mg film. The full % composition for the evaporated Mg is in Table 4-1. The Mg surface in Figure 4.1b shows a uniform surface, where small Mg crystals are visible. These properties are promising as Mg substrates, but high resolution XPS spectra and XPS depth profiles give further insight into the chemical composition.

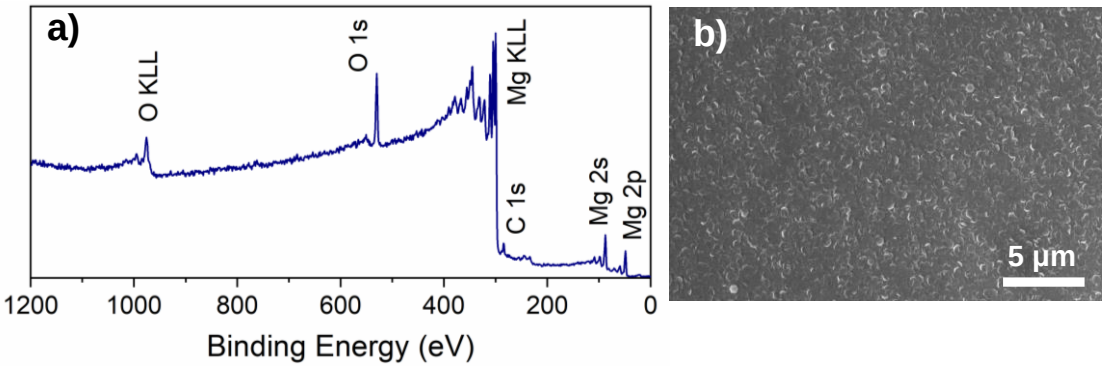

Figure 4.1 Surface characteristics of evaporated Mg, a) XPS survey spectrum and b) SEM image of the Mg surface on a stainless steel spacer.

To further understand the chemical speciation at the evaporated Mg metal surface, the high resolution XPS spectra are shown in Figure 4.2. While the overall composition at the surface is 45% Mg, a significant portion of that is MgO and other Mg^{2+} species as apparent in Figure 4.2a and b. In the Mg 2s spectrum in Figure 4.2a,

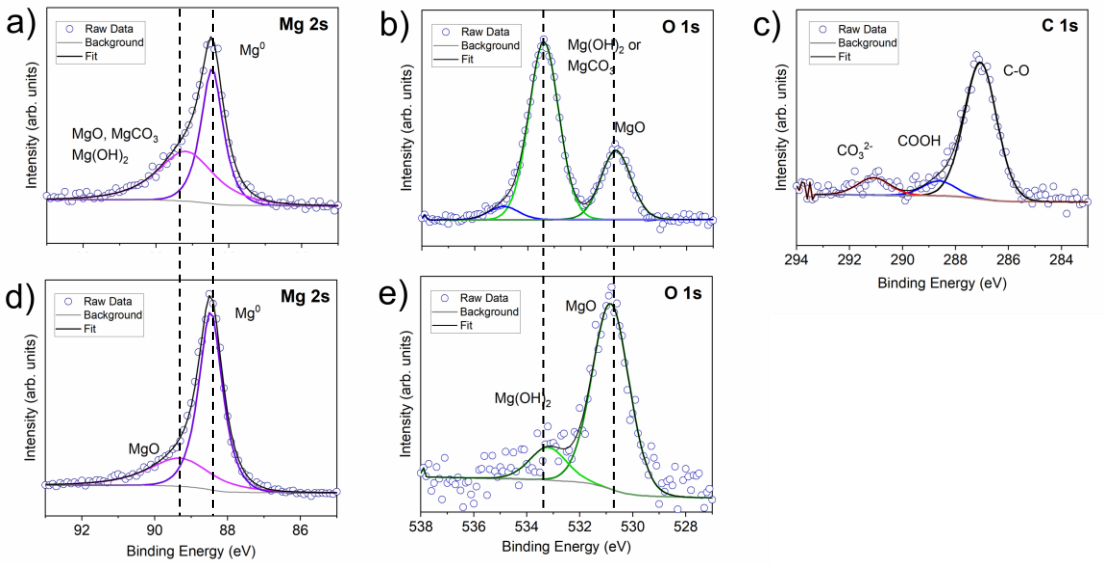

Figure 4.2 High resolution XPS spectra as deposited for a) Mg 2s, b) O1s, and c) C 1s and after 1250 seconds Ar sputtering for d) Mg 2s and e) O 1s.

the Mg metal peak appears at 88.5 eV and a broader peak is present at 89.5 eV, the latter of which is representative of Mg^{2+} species. Examining the O 1s spectra in Figure 4.2b, the oxide peak appears at 530.7 eV, while the high binding energy peak around 533 eV consists of a combination of $Mg(OH)_2$ and $MgCO_3$, and a higher energy peak at 535 eV which is likely $MgCl_2$ formed by reacting with contaminants in the glovebox atmosphere. The C 1s spectrum in Figure 4.2c contains adventitious hydrocarbon surface species at around 286.5 eV, C-O species around 288 eV, and carbonate species at 291 eV. Depth profiling was also performed to determine which species were present at the surface as compared to those that exist in the bulk of the film. In Figure 4.2d and e, some of the surface species in the Mg 2s and O 1s are the same as before sputtering, in particular Mg metal and MgO. However, some notable changes include the removal of the carbon species that were shown in Figure 4.2c, including $MgCO_3$. Further, the $Mg(OH)_2$ and MgO have decreased. This demonstrates that the carbon, most of the

$Mg(OH)_2$, and the $MgCO_3$ were surface contaminants while Mg metal and MgO are present throughout the film.

Table 4-1 Atomic composition results for Mg metal surfaces

	% Composition			
Region	Evaporated Mg	Mg metal (as received)	Mg metal (polished, F contaminated)	Mg metal (polished)
Mg 2p	45.46	9.96	21.04	14.43
O 1s	38.24	36.29	35.63	24.16
C 1s	16.30	50.91	31.14	61.41
F 1s	-	2.84	12.19	-

The full depth profile demonstrating how the elements vary into the bulk is presented in Figure 4.3. The carbon and chlorine are only present at the very surface, disappearing after 30 seconds and 180 seconds, respectively, supporting the assertion that they are surface contaminants. While the majority of the sample is about 80% Mg, 30% of that Mg in the bulk is MgO – it is not pure Mg metal. Because most of the evaporated Mg was metal, this substrate was still utilized in the ALD protection tests. The influence of the MgO on the electrochemistry will be discussed in Section 4.4.

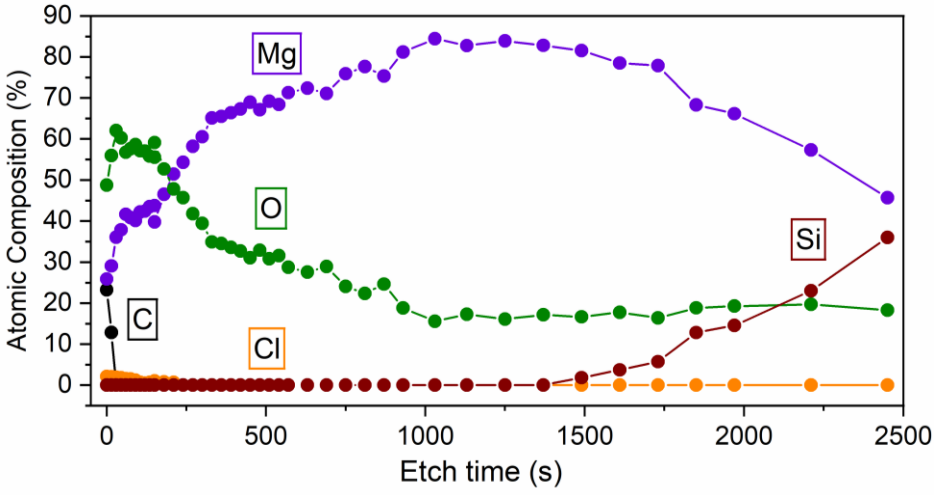

Figure 4.3 XPS depth profile of 100 nm thick evaporated Mg film on Si wafer.

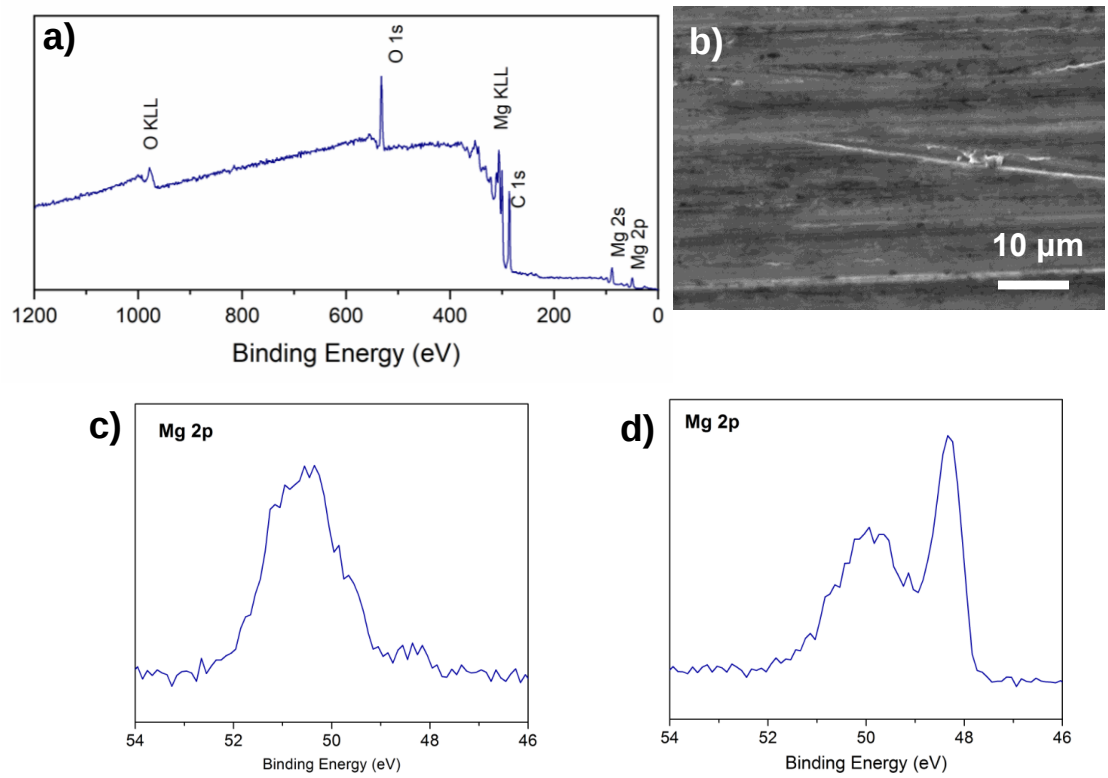

Figure 4.4 Surface characteristics of polished Mg foil, a) XPS survey spectrum and b) SEM image of the Mg surface. High resolution XPS spectra of c) as-received Mg metal foil and d) mechanically polished Mg metal foil.

In addition to evaporated Mg, Mg foil was also chosen to study the effects of ALD on the interface characteristics. Mg foil electrodes are quicker and easier to prepare for experiments; however, the interface needs to be mechanically polished due to the significant amounts of surface contamination that naturally form on the surface during processing and shipping. The XPS survey spectrum and an SEM image of the polished Mg foil are shown in Figure 4.4a and b, respectively. From the SEM, it is apparent that the surface is rough, likely on the order of µm, so it was not further characterized by AFM. This observation is one important difference from evaporated Mg, but due to the high conformality of ALD and its ability to coat high aspect-ratio structures the roughness should not prevent coating by ALD.

Different prepared Mg metal surfaces and their elemental compositions determined using XPS are shown in Table 4.1. The as-received Mg metal has significant carbon and oxygen species on the surface and only 9% of the observed sample was Mg, and the Mg detected was almost entirely in the form of Mg^{2+} compounds (~50-51 eV) and not Mg metal which occurs at lower BE (Figure 4.4c). There is also F contamination present, which was in the high vacuum system or glovebox atmosphere. Two polished Mg samples are represented, one with and without F contamination. In both cases the Mg content is almost doubled, and the Mg metal peaks appear after polishing demonstrating the removal of some, although not all, surface Mg^{2+} species (Figure 4.4d). With the exposure of Mg metal through polishing, this method was carried forward and used to prepare samples prior to ALD coating of the Mg metal electrodes.

4.4. Al_2O_3 Protected Mg electrodes

4.4.1. ALD Deposition on Mg metal

For ALD growth, the functional groups on the surface of the Mg need to be reactive with the Al precursor, TMA. Since the XPS in the previous section demonstrated that the surface contains some MgO and $Mg(OH)_2$, it was hypothesized that Al_2O_3 growth should not be an issue on Mg metal. The proposed reaction scheme is depicted in Figure 4.5. Figure 4.6a shows the Al 2p high resolution spectra of an evaporated Mg surface after 5 cycles and 10 cycles of Al_2O_3 ALD. This data illustrates that the Al_2O_3 coating does not grow enough to be detected on the surface until after 10 cycles, which based on the growth rate on Si is about 1 nm. The Mg metal peak is still visible, which can be determined from the presence of the Mg plasmon peak around

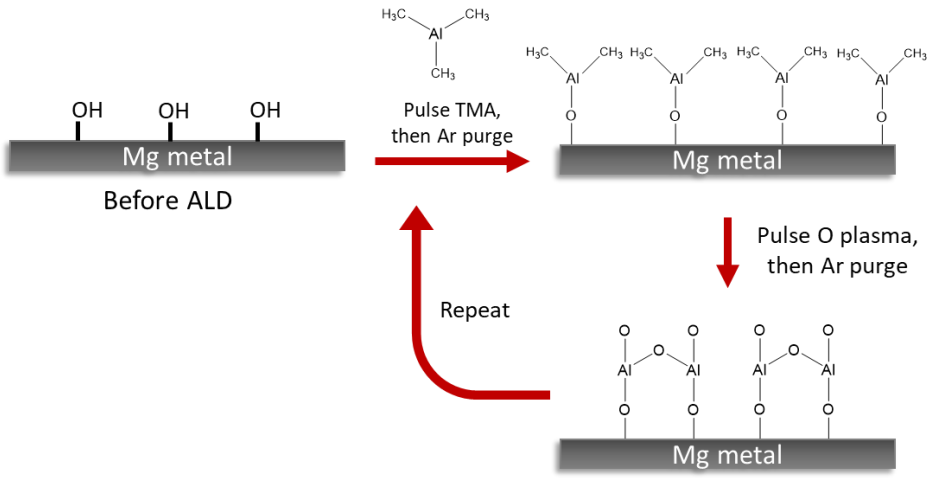

Figure 4.5 Schematic demonstrating the reactions during Al_2O_3 deposition with TMA and oxygen plasma.

70 eV that is still apparent. ALD deposition was also performed on Mg metal, and Figure 4.6b shows the XPS survey spectrum for Mg metal after 100 cycles of Al_2O_3 ALD. The thickness of the Al_2O_3 with this number of cycles is likely between 9-10 nm, and at this thickness it completely and conformally covers the Mg metal – no signal in the XPS for Mg is apparent. Generally, 6-10 nm is the depth of the surface that XPS can penetrate, although this depends on the materials and the inelastic mean free path of the photoelectrons.[139] This observation supports that the thickness of the Mg is likely consistent with the ALD growth rate on Si, with slightly thinner Al_2O_3 based on the 10-cycle delay in detecting the Al signal.

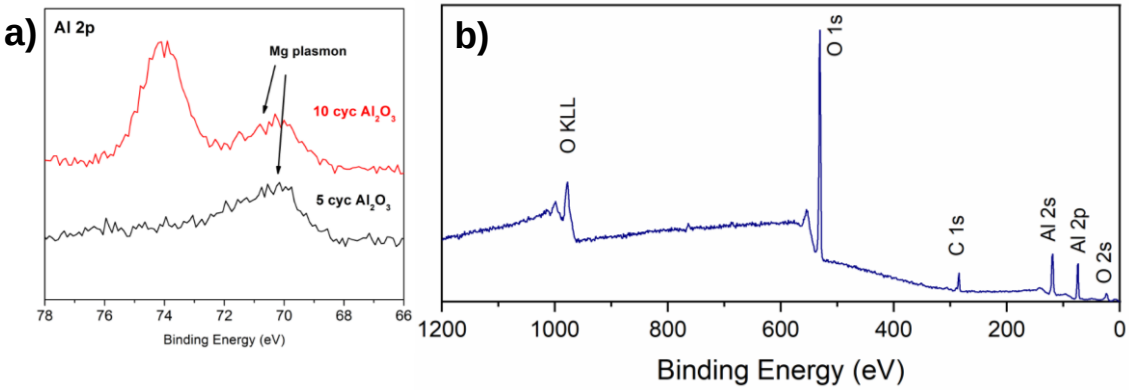

Figure 4.6 XPS of a) evaporated Mg after 5 and 10 Al_2O_3 ALD cycles and b) Mg metal after 100 cycles Al_2O_3.

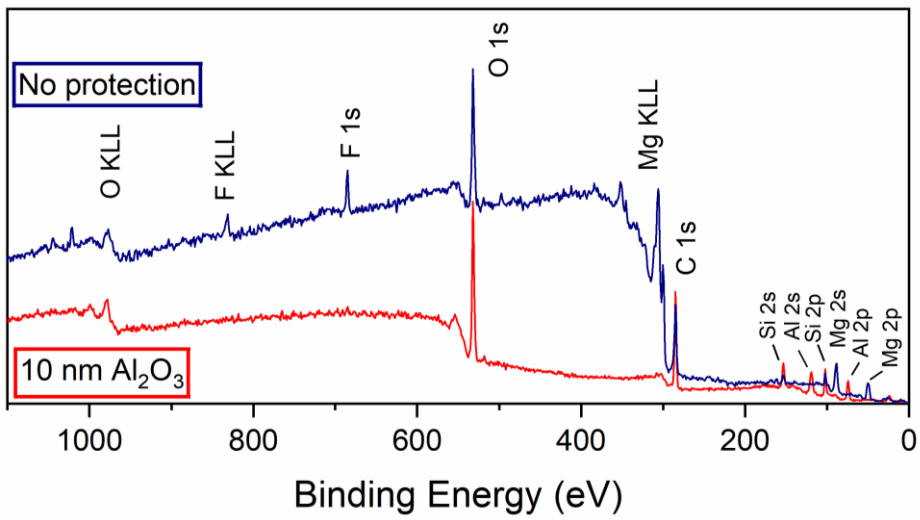

Figure 4.7 XPS survey spectra of Mg metal electrodes soaked in 0.25 M $Mg(TFSI)_2$ in DME electrolyte for 24 hours.

Mg metal has a sufficiently low reduction potential that degradation can occur on the surface from electrolyte being reduced at the metal interface. To test the ability of Al_2O_3 to protect Mg metal from initial contact with the electrolyte, Mg metal foil electrodes, both bare and protected with Al_2O_3, were soaked in 0.25 M $Mg(TFSI)_2$/DME electrolyte for 24 hours. The XPS survey spectra of these electrodes are shown in Figure 4.7. The sample without protection has degradation products on the surface from the electrolyte, with both F and S appearing in the XPS spectra. The exact atomic composition for the protected and bare samples is shown in Table 4-2. Both samples contain a small amount of Si contamination that likely comes from contact with residue from the latex gloves used inside of the glovebox. Most importantly, the sample with 100 cycles of Al_2O_3 deposited does not show any degradation on the surface, as there are no F or S signals in the XPS, only Al, O, C, and the Si. These results confirm that the ALD layer can keep the Mg metal underneath from reducing the electrolyte components.

Table 4-2 Atomic composition of Mg soaked in 0.25 M $Mg(TFSI)_2$/DME

Region	% Composition	
	Mg metal (bare)	Mg metal (10 nm Al_2O_3)
Mg 2p	19.55	-
O 1s	30.86	32.79
C 1s	40.05	51.88
Al 2p	-	12.74
F 1s	6.14	-
S 2p	2.46	-
Si 2s	0.94	2.60

4.4.2. Electrochemistry of evaporated Mg

The first substrate tested with Al_2O_3 deposition was the evaporated Mg metal. To get an initial baseline for the electrochemical performance, symmetric coin cells were made with 0.25 M $Mg(TFSI)_2$/DME electrolyte and bare evaporated Mg electrodes. The GV and EIS data for a bare Mg cell are depicted in Figure 4.8. The overpotential starts high, around 3 V, then settles to 2 V most consistently. In the following data, 1 cycle consists of 30 minutes of negative current plus 30 minutes of positive current, so 1 cycle = 1 hour. There are a few cycles where the overpotential drops below 1 V, indicating that the current at certain times could be maintained at a lower voltage. This high overpotential value is larger than some reported in the literature for Mg with this electrolyte,[54] which may be a result of the MgO in the evaporated Mg or some surface layer preventing Mg deposition and stripping. Lower overpotentials were observed for a different trial with evaporated Mg (Figure 4.9), but in that case the overpotential does ultimately increase and reach the upper limit set for the measurement (4 V).

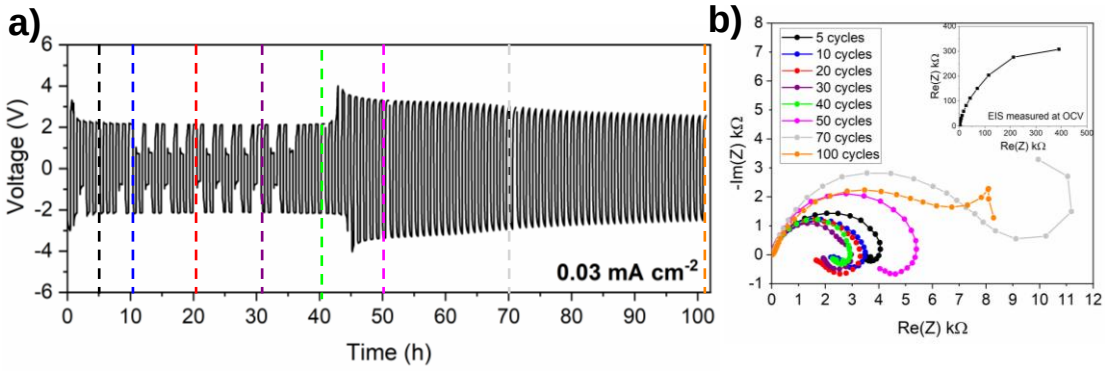

Figure 4.8 Electrochemistry of symmetric evaporated Mg coin cells, a) GV overpotential profiles and b) EIS during cycling, with EIS at the OCV before cycling in the inset.

The EIS in the inset of Figure 4.8b shows a large initial interfacial impedance in the inset, which supports that an SEI or passivation layer is forming at the interface. As this Mg is not protected, the electrolyte is likely degraded at the interface as demonstrated by the XPS results in Figure 4.7, increasing the impedance. The remaining EIS data are different from the inset because they are performed at the overpotential value, so the voltage is oscillated at the voltage measured from the preceding GV cycle. The main semicircle, representing the interfacial resistance, evolves over the course of the GV cycling. The origin of the low frequency semicircle going below the axis is not very clear and could have been due to instrumental issues causing inductive behavior.

The impedance in Figure 4.8b decreases going from 5 to 30 cycles, then slowly increases up to 70 cycles, then decreases again at the 100th cycle. The initial decrease in impedance could be due to breakdown of an initial MgO or other contamination still left on the surface, creating areas for Mg to more easily deposit/strip. However, if those sites become passivated by reacting with the electrolyte the impedance will reach a point where it starts to increase again. SEM imaging and XPS of the cycled evaporated

Mg electrodes was difficult because the Mg deposits grew into the glass fiber separator, meaning they could not be separated from the Mg. A less extreme example of this is shown in Figure 4.9b, where Mg deposits on Mg metal grew into the glass fiber separator and pieces of it are left behind after disassembling the cell (discussed further in the next section, 4.4.3). This observation may also indicate that the Mg was plating and stripping on top of the Mg film and the evaporated Mg potentially was minimally participating in the reaction.

The overpotential performance of the evaporated Mg electrodes after ALD of Al_2O_3 is shown in Figure 4.9. The overpotentials for both samples with Al_2O_3 are higher, remaining stable just above 2 V for about the first 30 GV cycles. The voltage of the sample with ~ 2 nm Al_2O_3 (20 ALD cycles) is only slightly higher than the sample with ~ 1 nm (10 cycles), with only a 50 mV difference between them. These high overpotential values indicate that the Mg deposition and stripping process occurs farther from the equilibrium potential. The increase can be attributed to the addition of the Al_2O_3 layer, and the root cause is likely either slow Mg diffusion in the Al_2O_3 (mass transport limited) or the electron transport is limited by the Al_2O_3, but still occurs due to the extremely thin nature of the protection layer or other defects. The bare and 2 nm Al_2O_3 samples both reach a point where the overpotential increases and reaches the voltage limit set, which was 5 V. The 10 cycle sample does not reach 5 V, although it comes close. The difference between hitting the limit and stopping versus continuing to cycle is very small, so we believe similar processes are occurring at all electrodes. However, more uniform passivation or somehow more ion or electron-blocking in

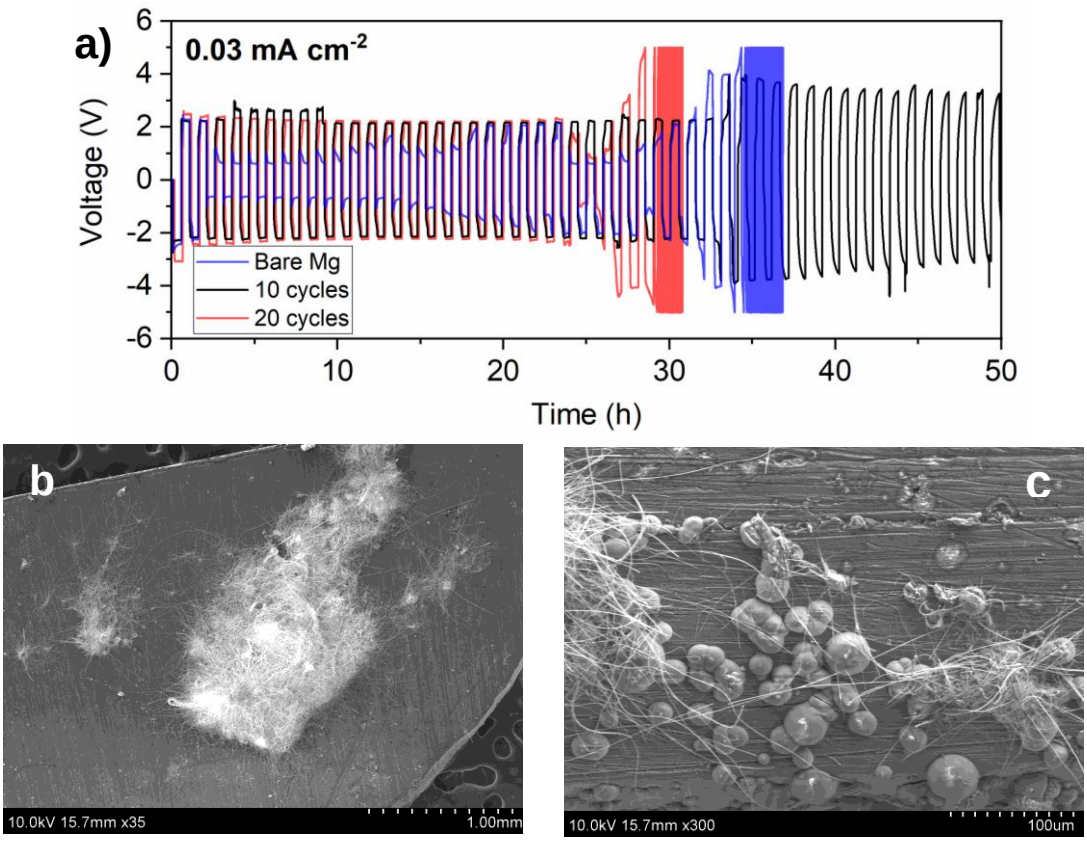

Figure 4.9 a) GV cycling of evaporated Mg after different cycle numbers of Al_2O_3 ALD: Mg with no coating, 10 cycles, and 20 cycles. SEM images in b) and c) demonstrate Mg deposits on top of Mg foil electrodes that grew into the separator.

certain cases (bare and 20 cycles in Figure 4.8) causes the limit to be reached whereas other electrodes (10 cycles in Figure 4.8 and bare Mg in Figure 4.7) can cycle longer.

Another interesting observation about the GV curves themselves is that they change shape when going from the lower overpotential region ~2 V to the higher region at ~3-4 V. The profiles change from flat plateaus to more of an arc shape for the 1 nm of Al_2O_3 sample. In studies with Li metal, this GV shape change was attributed to dead Li metal accumulating at the anode interface, creating mass transport limitations at the anode surfaces.[140] The similar GV curve evolution in these evaporated Mg cells may indicate that a layer at the interface is limiting the mass transport of Mg^{2+} ions as well,

though more detailed study would be needed to confirm this hypothesis. Due to the protrusive nature of the Mg deposits into the separator as well as the variances in GV performance, Mg metal was next investigated to determine if the evaporated Mg substrate could improve the electrochemical performance and properties.

4.4.3. Electrochemistry of Mg foil

Mg foil was studied under the same conditions as evaporated Mg to determine if the characteristics from the previous section could be attributed to the different methods of preparation and surface characteristics of the two types of Mg. The GV cycling and corresponding EIS of bare Mg foil before ALD is shown in Figure 4.10. There are a few cycles with a high overpotential, but it quickly stabilizes with an overpotential value around 500 mV. This behavior is similar to the bare evaporated Mg, although the overpotential value is much more stable and does not increase after longer cycling times and never reaches the 4 V limit. Examining the EIS, the initial impedance at the OCV before cycling for Mg foil is less than the evaporated Mg, but it is still in the hundreds of kiloohms range, indicating the interfacial resistance is high. At the overpotential around 500 mV after 10 cycles, the impedance again decreases

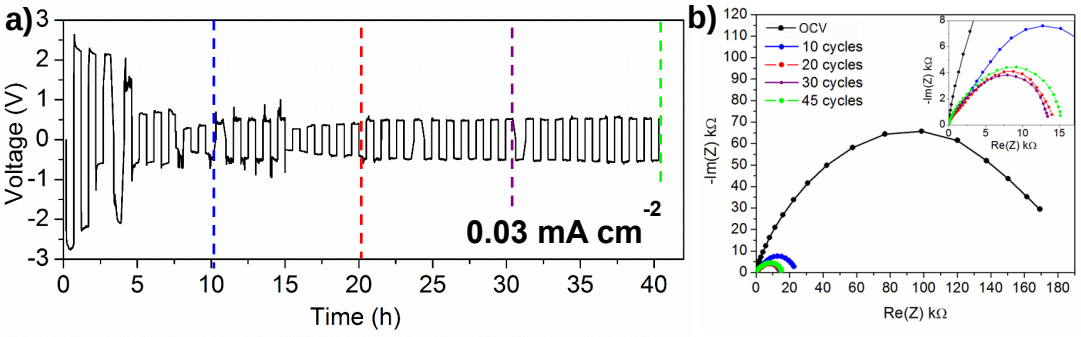

Figure 4.10 Bare Mg foil cycles in 0.25 M $Mg(TFIS)_2$/DME electrolyte a) GV cycling and b) EIS at corresponding overpotential values during cycling.

significantly like in the evaporated Mg case. Over successive cycles, the impedance once again increases each time. As mentioned previously, this observation is likely due to the passivation of new Mg deposits which causes higher impedance at the interface. With the addition of an Al_2O_3 layer, we expect there to be changes in overpotential and impedance, likely increases for both. However, improvements in stability of the overpotential and impedance values are some desired outcomes that could indicate improvement of Mg deposition and stripping at the interface.

The electrochemical data for Mg foil protected with 20 cycles of Al_2O_3 is provided in Figure 4.11. While at the same current density of the bare sample, the overpotential stays higher for many more cycles around 2 V, similar to the value for evaporated Mg. However, over time the overpotential value starts to decrease, and stabilizes around 325 mV, like the bare Mg foil sample in Figure 4.10a. If the high overpotential is due to a hindrance of the electron transport, the stabilization over time could be a result of defects forming in the Al_2O_3 layer which allows better electron transport and thus a decrease in the overpotential. The EIS data follows the same trend previously exhibited by both the evaporated Mg samples and the control sample of the bare Mg foil. The initial value of the impedance at the OCV is high, but after cycling

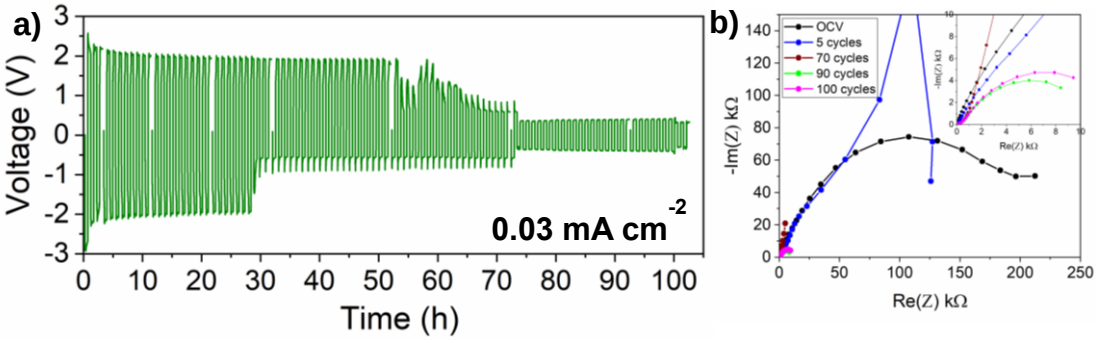

Figure 4.11 Mg foil with 20 cycles Al_2O_3 in 0.25 M $Mg(TFSI)_2$/DME electrolyte, a) GV cycling and b) EIS at the overpotential values during cycling.

and probing at the overpotential for the reaction there is a decrease in interfacial impedance.

The last thickness of Al_2O_3 tested on Mg foil was 50 cycles, or ~5 nm. The overall overpotential behavior, shown in Figure 4.12a, is like previous thicknesses although the high overpotential region at the beginning only lasts ~12 hours. Additionally, the overpotential stabilizes around 250 mV, which is the lowest value so far. A higher current density was also tested, 0.1 mA/cm^2, in Figure 4.12b. The higher current sample settles to a noisy overpotential of ~500 mV but reaches this value after only 5 hours. We propose that the higher current forces breakdown of the protection layer more quickly than low current, decreasing the time at the high overpotential. The

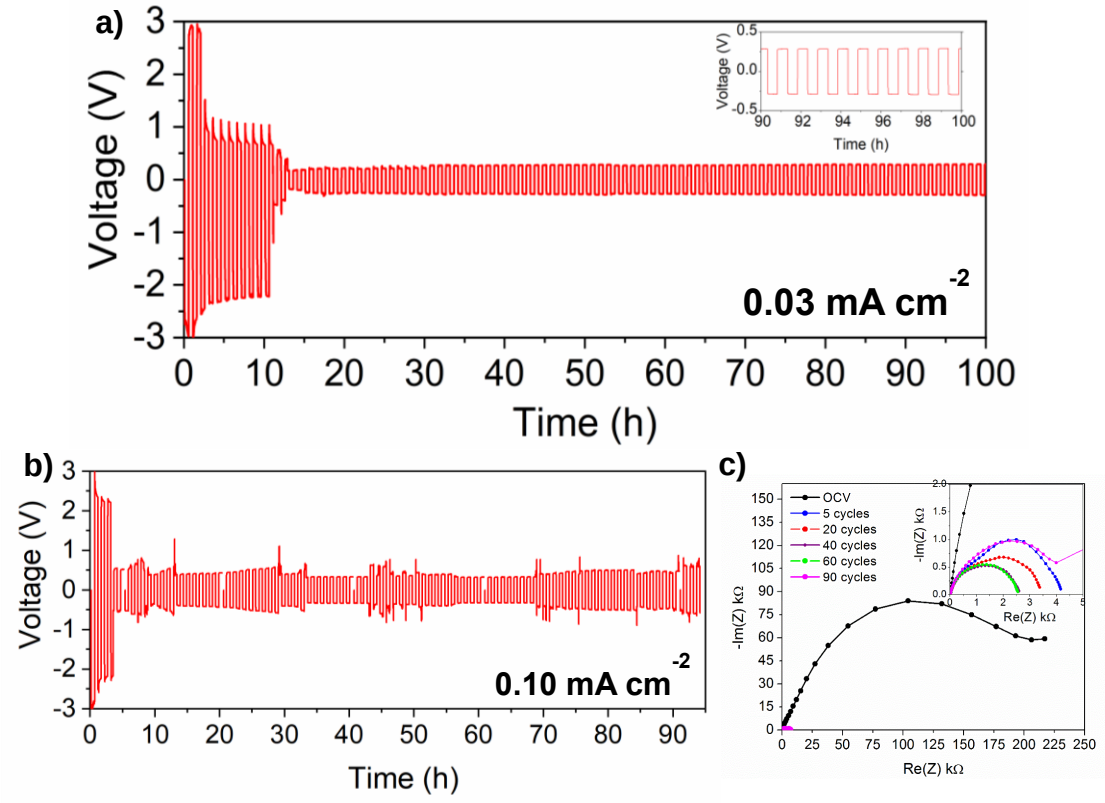

Figure 4.12 Mg foil with 50 cycles of Al_2O_3 in 0.25 M $Mg(TFSI)_2$/DME electrolyte, a) GV at low current density, b) GV at higher current density, and c) EIS during cycling at high current density.

stability of the cycling could possibly be related to where the Mg is depositing and stripping, whether it is from the bulk Mg or a portion of the Mg that deposited on top of the metal, although this is just one possible explanation. Again, the impedance data shown in Figure 4.12c follows the same trend as previous samples, with decreasing impedance at the voltage of the GV plateaus with an increase around 90-100 cycles, indicating degradation of the electrolyte is occurring over time on the surface of new Mg deposits.

The electrochemistry of symmetric Mg metal electrodes gives some insight into the effect of Al_2O_3 on Mg redox reactions at the metal anode interface. Overall, all the samples, both bare and Al_2O_3 coated Mg, demonstrate similar trends in overpotential as well as impedance. The Mg metal samples differ from evaporated Mg in that they settle to a lower overpotential of a couple hundred mV, whereas the overpotential of evaporated Mg stays around 2 V regardless if it is protection with Al_2O_3. The next section will tie these observations into further SEM and XPS characterization to propose possible explanations for these behaviors and relate them to current findings in the literature.

4.5. Possible Interfacial Reaction and Degradation Mechanisms

Building upon the results from the last section, it is difficult to definitively determine the origins of some of the electrochemical characteristics, but some explanations can be proposed. In Figure 4.13a, GV curves for a bare sample of Mg metal foil and a sample with 100 cycles of Al_2O_3 are depicted. The corresponding post-cycling SEM images of the overall surface for these samples are shown in Figure 4.13b

and c, respectively. Similar to examples in the last section, the bare Mg sample shown in black in Figure 4.13a initially has a high overpotential which gradually decreases. The cell was stopped immediately after the overpotential dropped from ~1 V to <0.1 V, which is usually indicative of a soft short.[32] A soft short is characterized by Mg deposits that may grow through the separator and contact the opposite electrode, but due to the electronically insulating passivation layer on the deposits there is not a direct electron path. This characteristic of the symmetric cells is one that has not completely been resolved in the literature – some researchers have instead said that a sharp overpotential decrease may be due to stabilization of the interface, not necessarily

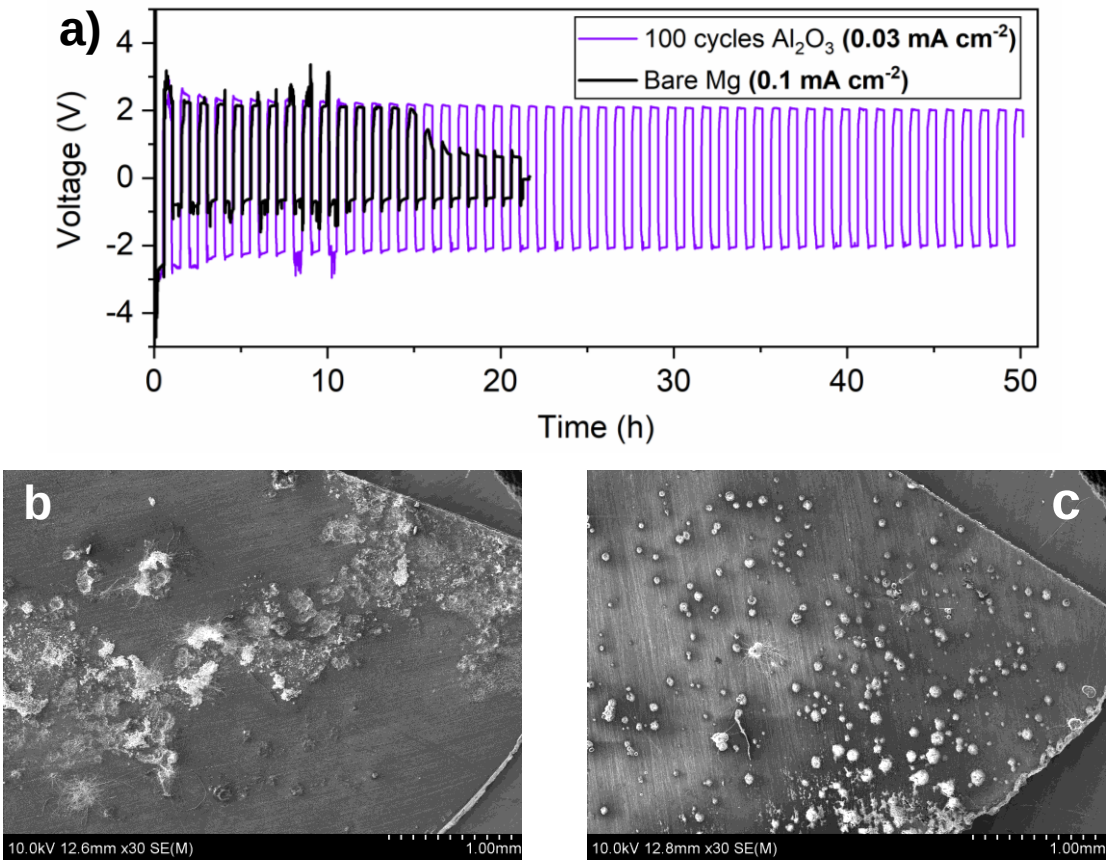

Figure 4.13 GV and SEM data for both bare Mg and 100 cycles Al_2O_3 on Mg. a) GV overpotential data for both samples, b) SEM of bare Mg after 20 hours, and c) SEM of 100 cycle covered sample after 50 hours.

shorting.[54] For the samples herein, it seems likely that a soft short may have occurred as pieces of the glass fiber separator can be seen attached to deposits in Figure 4.13b.

On the other hand, the sample shown in purple with 100 cycles of Al_2O_3 remains at a high stable overpotential right around 2 V, like the evaporated Mg samples. Unlike the bare sample which seems to have large bunched-up areas of Mg deposits, the sample with Al_2O_3 seems to have a more regular distribution of sites where Mg is depositing and stripping. The stable overpotential and well-distributed deposits help support the idea that the low overpotential values are tied to soft-shorting. If the deposits are occurring more uniformly across the surface and not building up on top of one another, they are less likely to go through the separator and make contact at the other electrode. These two different cases are illustrated in Figure 4.14. A soft-short may come from Mg deposits which grow from one electrode to the other, but because it is covered by a degradation layer that is slightly passivating, the layer may act as an electrolyte and keep the cell from completely shorting. The more regular morphology in Figure 4.13c could also help explain the behavior for evaporated Mg electrodes, despite not being able to directly image them. If the deposits on the evaporated Mg

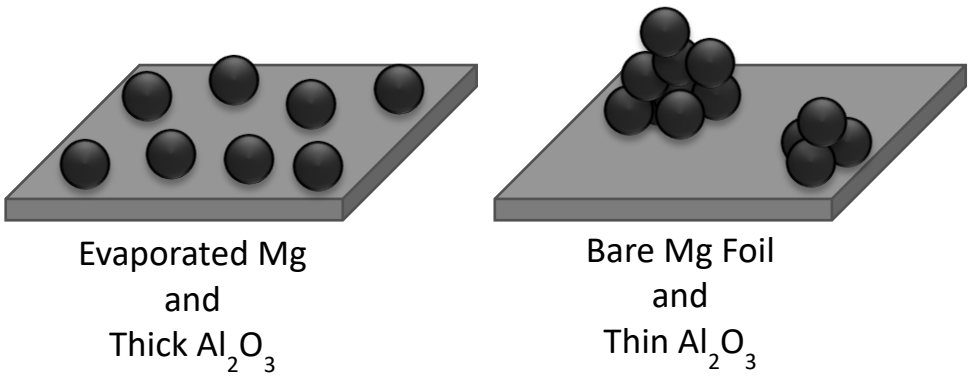

Figure 4.14 Schematic showing possible deposition morphologies based on Mg substrate and ALD films.

formed in a regular layer across the surface and only grew a short distance into the separator, the whole separator may stick to the electrode but it would not soft-short because the Mg did not grow through the separator to the opposite electrode.

To further understand the surface chemistry, different characterization methods were utilized to analyze how the electrolyte reacts on different surfaces of the cycled Mg electrodes. In Figure 4.15, SEM-EDS and XPS analysis is presented to demonstrate the surface chemical species on an electrode with 20 cycles of Al_2O_3 after it has been cycled for 250 hours. The SEM images show both Mg deposits and regions where Mg

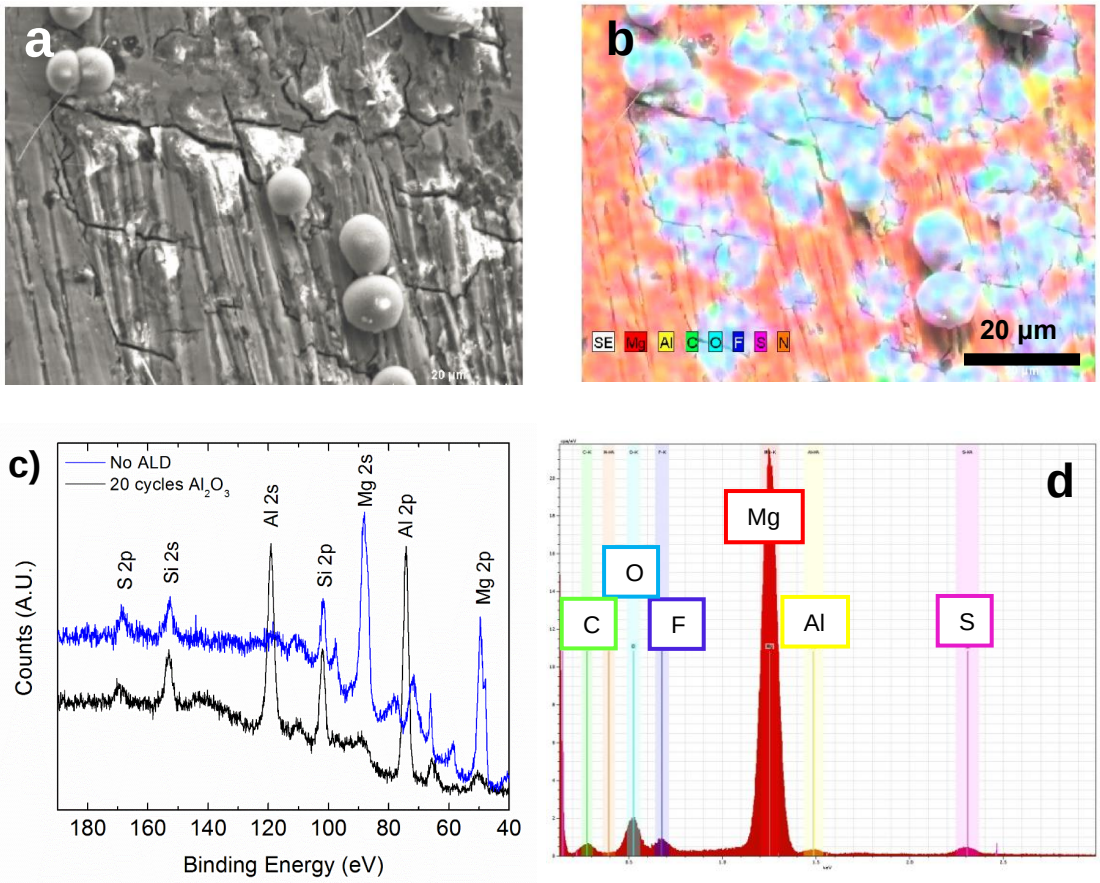

Figure 4.15 Analysis of a cycled Mg foil electrode with 20 cycles of Al_2O_3. a) SEM image showing Mg deposits and stripping regions, b) EDS map of the region in (a), c) XPS spectrum of the low binding energy region containing Mg and Al signals taken using a non-monochromatic Mg x-ray source, and d) EDS spectrum corresponding to the map in (b). The scale bar in (b) is the same for both SEM images.

has been stripped away on a previous cycle. The charging on the SEM image is common for SEI layers on metals, as the degraded products are not electronically conductive. In the corresponding EDS map in Figure 4.15b, the Mg deposits as well as the stripped areas have significant amounts of O, F, S, and C species, while the pristine areas are mostly Mg and Al. The relative amounts of these degraded species were examined using XPS, with a portion of the spectra depicted in Figure 4.15c. The quantitative atomic composition percentages from XPS are in Table 4-3.

Table 4-3 Atomic composition from XPS analysis of cycled Mg foil electrodes

	% Composition						
	Mg 2p	Al 2p	Si 2s	S 2p	O 1s	C 1s	F 1s
Bare Mg foil (Mg deposited)	19.0	-	2.6	0.7	28.4	44.4	4.9
Bare Mg foil (Mg stripped)	8.5	-	4.6	2.3	22.6	22.6	6.4
20 cycles (Mg deposited)	4.3	14.3	2.3	1.1	32.4	41.6	4.0
20 cycles (Mg stripped)	3.9	12.2	2.2	1.2	28.6	46.9	5.1

Overall, the electrolyte degrades on both bare and protected Mg foil surfaces upon cycling, as similar amounts of S and F degradation products are apparent from Table 4-3. The EDS mapping agrees well with the earlier studies where Al_2O_3 protected electrodes were soaked in the electrolyte because it also shows that the degradation does not happen on the protected Mg regions. The electrolyte is only degrading on the regions where Mg has been stripped from the surface, removing the Al_2O_3 layer and exposing fresh Mg, or on new fresh deposits above the Al_2O_3 layer. While EDS is not effective for detecting the Al_2O_3 due to the large amount of bulk Mg and very thin (~2 nm) Al_2O_3 layer, apparent from the small Al signal in Figure 4.15d, the XPS shows the Al signal is present on the surface, even after 250 hours of cycling. From these results, it appears that Al_2O_3 can protect Mg from the electrolyte marginally, although the layer

does not stay intact during cycling. Over time, as Mg strips and deposits, the Al_2O_3 layer is degraded and no longer prevents electrolyte from reacting with fresh Mg.

This project was initiated before much of the current literature on the properties of $Mg(TFSI)_2$ based electrolytes was reported. Early studies on characterizing this electrolyte demonstrated similar spherical deposits to those observed in this study,[51] which were identified as non-dendritic. Other works at the time demonstrated the high overpotential for deposition and stripping[52] which was the basis for the work in this dissertation. Study of a slightly modified version of the electrolyte, containing $Mg(TFSI)_2$ and $MgCl_2$ salts, demonstrated more reversible deposition and stripping as Cl^- has been identified as a species that improves interfacial characteristics of Mg metal by blocking contaminants from reacting at the interface.[36] However, even this Cl^- containing electrolyte still demonstrated passivation which resulted in spherical Mg deposits at high current densities, as well as pitting and roughened Mg surfaces upon cycling.[53] The results in this chapter support these studies in the literature, while also helping to inform what properties are necessary for a protection layer to be effective.

From this work, Al_2O_3 protection layers deposited via ALD that are <10 nm in thickness are not effective at protecting the Mg anode interface from electrolyte degradation and do not help to decrease the overpotential for Mg deposition and stripping. Some other factors to consider are the roughness of the Mg anode surface, as there were differences in the performance of the evaporated Mg and Mg foil samples. However, these differences can not only be attributed to the surface roughness as the evaporated Mg also had more MgO within the film. The thickness of the Al_2O_3 did also not to appear to have a major effect on the electrochemistry, although no thicknesses

beyond 10 nm were tested here. More uniform surfaces, such as evaporated Mg and Mg foil with thicker ALD layers appeared to have more regularly dispersed deposits of Mg compared to Mg foils with thin or no Al_2O_3. This result may be related to surface roughness as well, as the mechanically cleaned surfaces are very rough and more electrochemical hot spots experiencing higher current density may be present.

For future efforts in Mg anode protection, the results of this work give some insight into important properties for the protection layer materials. The rigid Al_2O_3 was unable to withstand the volume change induced by Mg deposition and stripping, leading to defects in the layer and deposition on top of it. This observation means that more flexible layers such as polymers may be more feasible for Mg anodes, and this has been recently demonstrated using polyacrylonitrile.[61] Further, since it is not clear whether the Al_2O_3 was actually magnesiated during these tests to $MgAl_2O_4$, one issue with this protective layer could have been poor Mg diffusion, highlighting the importance of having an interphase layer with good Mg^{2+} ion conductivity. Additionally, if defects ultimately form in a protection layer, another method is to put additives in the electrolyte that react at the anode interface to form a Mg^{2+} conductive layer that prevents electrolyte degradation and passivation. This strategy has been demonstrated using iodine in a RMB system, and the additive can continually form the protection layer on new Mg deposits during cell operation.[60] While Al_2O_3 was not found to be effective in this study, further experiments could determine the exact cause of the failure, such as looking more closely at the surface roughness, Al_2O_3 layer thickness, as well as ion mobility and the formation of $MgAl_2O_4$. Other ALD chemistries for Mg

materials should also be explored, as there are not many reported materials synthesized using ALD that are useful as Mg battery electrolytes or protection layers.

4.6. Conclusions

The effect of Al_2O_3 ALD layers on the electrochemical properties and surface chemistry of Mg metal anodes was investigated using a range of characterization techniques and Mg substrates. Two Mg metal substrates, one made via Mg evaporation and the other a cleaned Mg foil, were studied in symmetric coin cells in 0.25 M $Mg(TFSI)_2$/DME electrolyte. Al_2O_3 was deposited on both substrates using ALD, and it was determined that the ALD layer prevented electrolyte decomposition when protected electrodes were soaked in the electrolyte. However, upon electrochemical testing and characterization of the surface morphology using SEM, it was apparent that this layer was not preventing Mg metal from depositing on top of the protection layer and was unable to effectively protect the Mg anode surface. This work gives a starting point for identifying some major issues in protecting the Mg interface, and these results can be used to design better protection layers in future studies.

Chapter 5: Mg^{2+} ion-catalyzed polymerization of 1,3-dioxolane in battery electrolytes

Portions of this chapter are included in a just accepted publication, Sahadeo et al, Mg^{2+} ion-catalyzed polymerization of 1,3-dioxolane in battery electrolytes. *Chem. Commun.* **2020**. *Reproduced by the permission of the Royal Society of Chemistry*. (https://doi.org/10.1039/D0CC01769H) *MALDI samples were prepared in collaboration with Yang Wang, who contributed to discussion and analysis of the MALDI data. My contribution was all H-NMR and electrochemical data and analysis.*

5.1. Introduction

Solid and gel polymer electrolytes have been studied for a variety of energy storage systems, particularly Lithium-ion[141-144] and rechargeable magnesium batteries.[4, 145, 146] There are safety benefits in moving away from flammable liquid electrolytes, and there have been improvements to polymers' ion transport, stability, and mechanical properties which make them an attractive choice for electrolytes.[146] One solvent commonly used in Li batteries known to undergo polymerization reactions is 1,3-dioxolane (DOL). This solvent has been used widely as a component in electrolytes for Li-sulfur batteries due to its unique ability to electropolymerize on the surface of Li metal anodes, investigated by Aurbach's group.[5] The DOL additive helped to create a protective SEI layer containing a DOL elastomer combined with commonly formed inorganic species such as Li_2O, Li_2CO_3, and $LiNO_3$ (which may differ depending on electrolyte additives) and has been utilized in a variety of ways to improve Li anode performance.[130] In addition to its application in creating a functional, protective SEI layer, recently polymerized DOL (poly-DOL) has been demonstrated as an effective solid polymer electrolyte in Li batteries.[147-149] DOL has not been used or investigated extensively in Mg batteries as an electrolyte solvent, which may be due to

reports indicating instability at the Mg anode and a decreased coulombic efficiency in electrolytes containing DOL.[150] However, some Mg-S battery studies have utilized DOL as a part of their electrolytes,[15, 38, 151] and understanding the Mg anode interface properties are critical to battery design.[152] The lack of insight into DOL compatibility with Mg anodes is important to investigate.

Therefore, the findings in this work will have two-fold importance. First, it is urgent to inform the Mg battery community of certain Mg^{2+} salts ability to catalytically polymerize DOL in electrolyte solutions, which has not previously been reported. In a broader impact to the science community, while Mg^{2+} ion catalytic activity is known in some biological systems and small organic molecule synthesis,[153] researchers have not realized its applications in polymerization reactions. Second, it is essential to investigate the electrochemical properties of Mg^{2+} catalyzed DOL polymer layers that may form on electrode surfaces in electrolyte systems containing Mg^{2+} and DOL. Additionally, while poly-DOL was determined to be an effective polymer electrolyte for Li systems,[147-149] it has not been studied in Mg batteries; if it can be utilized as a solid or gel polymer electrolyte, it could bypass possible incompatibilities of liquid DOL electrolytes.

5.2. Experimental methods

5.2.1. Electrolyte Preparation

All solutions were prepared in an LC Technology glovebox with inert Ar environment and water and oxygen content <0.5 ppm. Mg bis(trifluoromethanesulfonyl)imide (Solvionic, Inc) was dried at 200 °C under vacuum

for 24 hours. Magnesium perchlorate and Lithium bis(trifluoromethanesulfonyl)imide (Sigma Aldrich) were dried at 140 °C and 160 °C, respectively under vacuum overnight. Magnesium triflate (STREM chemicals), Aluminum triflate, Lithium triflate, 1,3-dioxolane, and 1,2-dimethoxyethane (Sigma Aldrich) were used as-received. Solutions were mixed in 10 mL glass vials. In making the DOL solutions, micropipettes were used to add exact amounts of 1,3-dioxolane to the salts, e.g. 2 mL DOL added to 0.0474 g $Al(OTf)_3$ for 50 mM solution. The true molar concentration may be slightly less than 50 mM, but across samples the mole ratio of cation:DOL remains constant.

5.2.2. H-NMR

All samples were prepared in the inert glovebox environment using d_6-DMSO (Cambridge Isotope Inc.) unless otherwise indicated and referenced to the DMSO solvent residual signal (TMS=0). H-NMR analyses were performed on a Bruker AV-400 MHz spectrometer and analyzed using TopSpin software.

5.2.3. MALDI-MS

The Matrix-assisted laser desorption/ionization – mass spectrometry (MALDI -MS) measurements were performed on a Bruker Autoflex MALDI-TOF mass spectrometer. The mass spectra were obtained in linear positive mode with 2,5-dihyroxybenzoic acid as the matrix. The mass range was from 500 to 5000 Daltons.

5.2.4. IR Spectroscopy

FTIR measurements were taken on a Thermo Nicolet NEXUS 670 FTIR with an attenuated total reflectance smart endurance unit and a standard diamond window.

5.2.5. Electrochemical Impedance Spectroscopy

The electrolyte was made by mixing the $Mg(ClO_4)_2$ salt with DOL and fully dissolving it before adding the $Mg(TFSI)_2$ salt. While still liquid enough to pipette, the solution was drop-casted onto the stainless steel disks 62.5 μL at a time, with 125 μL total deposited on each disk. The polymers were left to polymerize for 6 hours before sandwiching two halves together and closing in a coin cell. The thickness was measured after EIS by taking apart the coin cell and measuring the whole stack with a micrometer and subtracting the thickness of the stainless steel disks. Impedance data was collected at the open circuit potential (generally 5-10 mV) between 200 kHz and 10 mHz with 100 mV amplitude. Fitting was performed using Z-fit in the EC-Lab software.

5.3. Results and Discussion

In this study, the polymerization behavior of DOL with multivalent Mg and Al salts was investigated. The ability of Lewis Acid species to catalyze many organic reactions is well known,[153] however Mg triflate (OTf) and bis(trifluoro-methanesulfonyl)imide (TFSI) have only been demonstrated as catalysts for a few reactions and have not been demonstrated for use in the polymerization of DOL to our knowledge. We studied Mg^{2+} and Al^{3+} Lewis acid catalyzed polymerization of DOL and investigated the effect of strength of Lewis acidity, Mg^{2+} counter anions, and cosolvents on such polymerization. We briefly explored the potential application of the DOL polymer as a solid electrolyte.

To evaluate the role of the cation of the metal salt in the catalysis of DOL polymerization, different metal (Mg, Li, and Al) triflate salts were tested. The stronger Lewis acid cations (Mg^{2+} and Al^{3+}) were anticipated to induce the polymerization reaction, which is supported by the use of $Al(OTf)_3$ as a catalyst for a variety of reactions in the literature.[154, 155] However, the less Lewis acidic Li^+ cation was not expected to cause the same reaction. After adding the salts to DOL, H-NMR was conducted after the salt was fully dissolved, after about 10 minutes of mixing. The solutions were then left overnight, and H-NMR samples were run the following day after 18 hours. MALDI-MS was run on the solidified, polymerized samples after the same 18 hour reaction period.

The results of H-NMR and MALDI experiments are depicted in Figure 5.1. The H-NMR in Figure 5.1a indicates that in the case of the LiOTf solution, no peaks indicative of DOL polymerization can be seen in the spectra – only the peaks at 3.77 and 4.78 ppm for the DOL monomer (O-CH_2-O and O-CH_2CH_2-O) are present. The same observation is true of the 50 mM Mg and Al triflate salt solutions after short time periods (10 minutes). However, after waiting for 1 hour, $Al(OTf)_3$ shows new peaks for poly-DOL at 3.59 and 4.63 ppm,[147, 156] whereas Mg triflate shows a similar level of polymerization after 18 hours. FTIR spectra of polymerized DOL using $Al(OTf)_3$ and $Mg(TFSI)_2$ catalysts and a sample also containing $Mg(ClO_4)_2$ are in Figure 5.2, demonstrating the major C-H and C-O functional groups indicative of poly-DOL structure around 2900 and 1000 cm^{-1}, respectively.

$$\frac{H_p}{H_p+H_m}\times 100 = \%\ \text{polymer} \qquad \text{Equation 5.1}$$

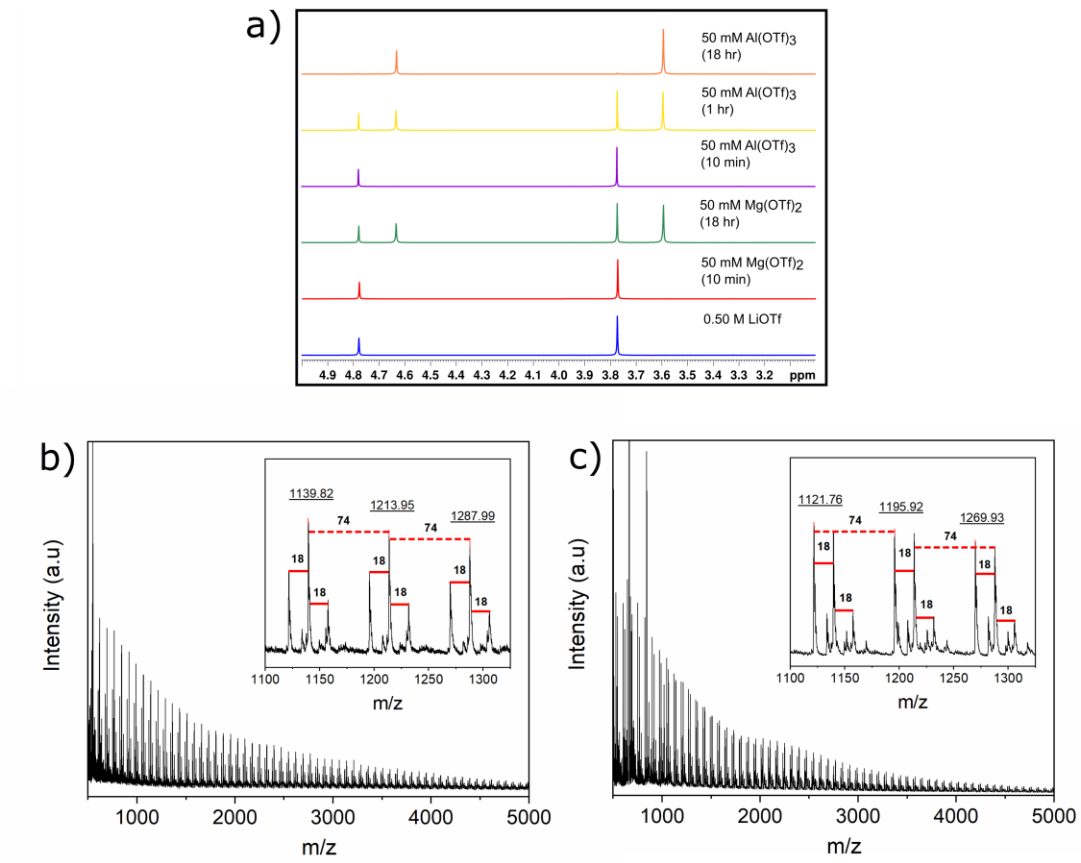

Figure 5.1 H-NMR spectra of a) DOL samples with Al, Mg, and Li triflate salts after various reaction times, and MALDI-MS spectra of 50 mM b) $Mg(OTf)_2$ in DOL and c) $Al(OTf)_3$ in DOL after 18 hours.

The percent polymer detected by H-NMR, using Equation 5.1 where H_p is the integral of polymer protons and H_m is the integral of monomer protons,[147] for $Mg(OTf)_2$ is 61.7% after 18 hours while $Al(OTf)_3$ is 63.6% after 1 hour. The $Al(OTf)_3$ sample has achieved 99.0% polymer composition at 18 hours and minimal monomer is present. The H-NMR spectra show only peaks from the DOL monomer, poly-DOL, and water (3.33 ppm). The DMSO solvent peak appears at 2.50 ppm but is omitted for simplicity. These observations indicate that we do not see end groups for the polymer, meaning the hydroxyl terminations may be in too low concentration to detect or some products may be cyclic oligomers.

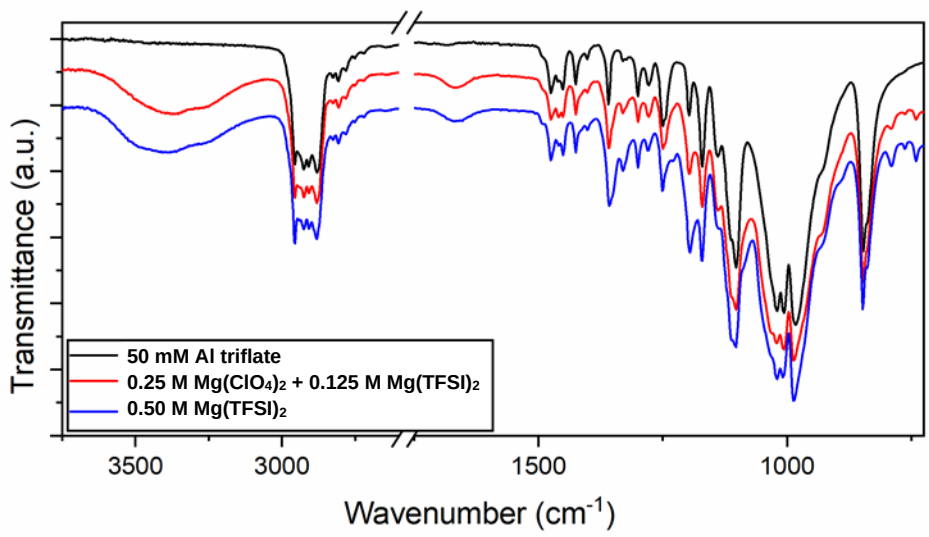

Figure 5.2 FTIR spectra of fully polymerized DOL with different amounts of salt catalysts.

To confirm the products of the DOL polymerization, MALDI-MS was performed on all samples. Figure 5.1 shows the MALDI-TOF MS result of polymerized 50 mM $Mg(OTf)_2$ and $Al(OTf)_3$ dissolved in DOL solvent. It shows a series of molecular ion peaks with molecular weights up to the scanning limit, 5000 Da. The high MW fragments indicate the formation of polymer macromolecules. Further investigating the MALDI mass spectrum, the inset of Figure 5.1b shows the regional spectrum of $Mg(OTf)_2$ in DOL. For each group of peaks that represents a similar pattern, there is a main peak with the highest intensity and two satellite peaks on each side of the main peak. The molecular weight difference between the two main peaks adjacent to each other is ~74 Da, which is equivalent to the molecular weight of one DOL molecule. This pattern is representative of the entire mass spectrum which proves the molecular ion peaks are of poly-DOL molecules, formed due to Mg^{2+} catalytic polymerization of DOL monomers. Moreover, each satellite peak has a molecular weight difference of ~18 Da relative to its main peak, indicating there are likely

polymers with one and two water adducts. In the cluster of three peaks, the first peak contains no water, the second (and highest) has one water, while the final peak has two water molecules.

The 50 mM $Al(OTf)_3$ in DOL was tested using MALDI-MS and the result is shown in Figure 5.1b. In this mass spectrum, there are significant molecular ion peaks even in the high MW region. Those peaks also show the same pattern of 74 difference in MW between the main peaks of two adjacent groups. This confirms that poly-DOL molecules were formed in $Al(OTf)_3$ in DOL solution. However, the peak distribution in the mass spectrum of $Al(OTf)_3$ has changed from the one of $Mg(OTf)_2$. In the mass spectrum of $Al(OTf)_3$, there are two main peaks instead of just one with nearly identical intensity that have a 74 Da difference in MW. This indicates with stronger Lewis acid $Al(OTf)_3$ as polymerization catalyst, the reaction that generates polymer chains assumed without water is more favored. Further, a 0.35 M LiTFSI in DOL sample was tested using MALDI-MS and the results can be found in Figure 5.4a. The mass spectrum of LiTFSI solution is unlike the $Mg(OTf)_2$ and $Al(OTf)_3$ samples in DOL; it does not have peaks of high molecular weight and does not show the pattern of 74 Da in MW between adjacent groups of peaks. This demonstrates that under same conditions, Li^+ cannot catalyze the polymerization of DOL, which can be attributed to its lower Lewis acidity compared to Mg^{2+} and Al^{3+}.

While there is a dependence of the DOL reaction on the cation of the metal salt, the anions of Mg^{2+} salts were also altered to determine if it influenced the polymerization. In addition to $Mg(OTf)_2$, $Mg(TFSI)_2$ and Mg perchlorate ($Mg(ClO_4)_2$) salts were tested in DOL. The 0.25 M $Mg(ClO_4)_2$/DOL solution did not visibly increase

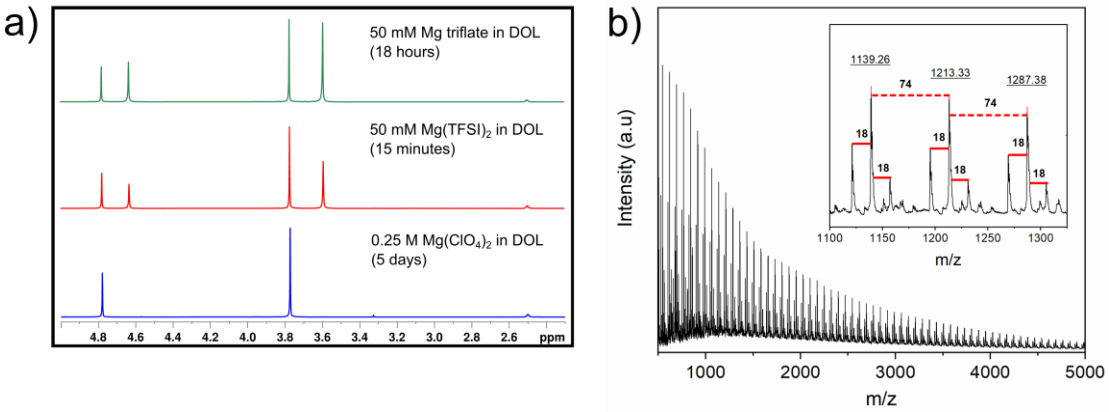

Figure 5.3 H-NMR spectra of a) DOL samples Mg triflate, TFSI, and perchlorate salts after varied reaction times, b) MALDI-MS spectra of 50 mM $Mg(TFSI)_2$ in DOL.

in viscosity or show peaks of a polymerized product in the H-NMR results (Figure 5.3a). The $Mg(ClO_4)_2$ solutions were tested at higher concentrations and left to react for longer times, and even after 5 days no new peaks are present in the H-NMR. Interestingly, the $Mg(TFSI)_2$ salt catalyzes a much faster polymerization than the triflate, as the polymer peaks at 3.59 and 4.63 ppm are visible after only 15 minutes with a 50 mM concentration of the salt. In comparison, the $Mg(OTf)_3$ sample contains 61.7% polymer after 18 hours while $Mg(TFSI)_2$ is 49.1% polymer after 15 minutes.

Like the mass spectrum of $Mg(OTf)_2$ in DOL, the solution with 50 mM $Mg(TFSI)_2$ also shows distinct molecular ion peaks of high molecular weights and the 74 Da difference in MW between adjacent main peaks. It indicates that $Mg(TFSI)_2$ can also catalyze the polymerization of DOL. Both $TFSI^-$ anion and triflate anion have a $-SO_2CF_3$ group in their structures, which helps delocalize the negative charge throughout the anion.[157] The TFSI anion has two $-SO_2CF_3$ groups, making the charge even more delocalized, enhancing its ability to be a weakly coordinating anion and increasing the Mg^{2+} cation's positive character and Lewis acidity. For the 0.25 M $Mg(ClO_4)_2$ in DOL sample (Figure 5.4b), while there was not significant polymer

formation observed in H-NMR, some peaks also show the characteristic 74 Da difference in MW pattern in the MALDI mass spectrum, though the overall intensity of the peaks are smaller than those in $Mg(TFSI)_2$ and $Mg(OTf)_2$ solutions. Most importantly, there are minimal peaks at high MW region of mass spectrum. Mg and Al triflate and $Mg(TFSI)_2$ can catalyze DOL polymerization, and while $Mg(ClO_4)_2$ may catalyze the reaction we believe it is much slower due to the stronger interactions of the ClO_4^- anion with Mg^{2+}.

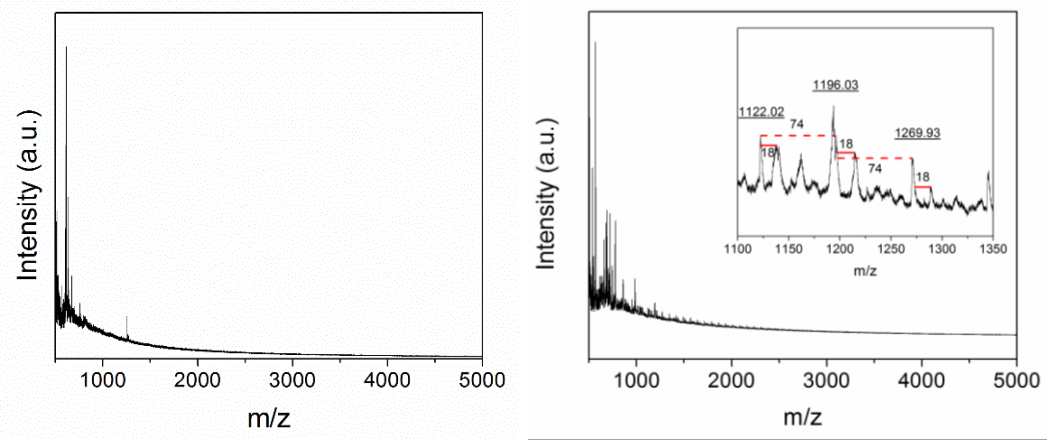

Figure 5.4 MALDI-TOF mass spectrum of a) 0.35 M LiTFSI in DOL and b) 0.25 M $Mg(ClO_4)_2$ in DOL after 5 days.

For electrochemical applications such as batteries, mixtures of solvents are often used to take advantage of an important property of each. For example, in lithium sulfur batteries, DOL has been used as part of electrolytes that also contain ethers such as 1,2-dimethoxyethane (DME) and the larger ethers such as diglyme and tetraglyme. These dual solvent electrolytes are important due to the unique property of DOL to electropolymerize and help create a soft organic layer in the SEI in addition to the inorganic SEI components.[5, 130] Due to the additional positive charge on Mg^{2+} as compared to Li^+, its solvation and solution behavior is very different.[55] There are not

many reported instances of DOL being used in Mg battery electrolytes, and one of the few instances was electrolyte with $Mg(TFSI)_2$ and $MgCl_2$ in TEGDME/DOL (1:1 v:v).[15] This electrolyte with other solvents is known to create a metal complex with Mg,[158] meaning the Mg^{2+} ion itself is not free in the electrolyte. We propose that these complexes do not catalyze DOL polymerization, hence why other groups have not observed significant polymerization of their electrolytes. To further support the hypothesis that free Mg^{2+} ions are necessary to catalyze polymerization of DOL, this solvation behavior of Mg^{2+} was utilized. It was previously observed that Mg^{2+} ions from $Mg(TFSI)_2$ in DME electrolyte became so strongly complexed by 3 DME molecules that the complex could be crystallized and studied using XRD.[159] We propose that if the Mg^{2+} is first complexed by DME, it will not be able to polymerize DOL.

To test this hypothesis, a 1:1 v/v solution of DME/DOL was mixed to create a 0.35 M $Mg(TFSI)_2$ in DME/DOL electrolyte solution. Interestingly, this electrolyte does not polymerize in the same manner as when DME is absent. When the amount of DME is decreased to a 1:7 DME/DOL solution with 0.35 M $Mg(TFSI)_2$, a phase

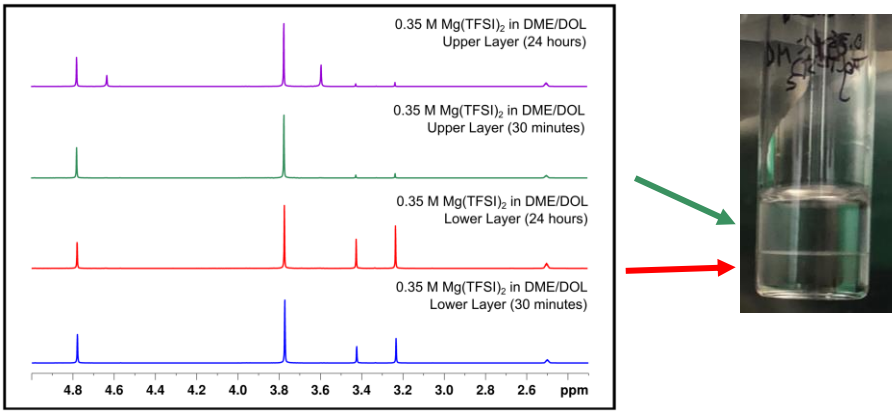

Figure 5.5 H-NMR spectra of 0.35 M $Mg(TFSI)_2$ in 1:7 (v/v) DME/DOL of the top and bottom layers of the separated layers after different amounts of reaction time.

separation is still observed, and gelation of the top layer occurs (Figure 5.5). The initial mole ratio of DOL:DME in this case is 10:1, and different ratios of the solvents were found in the new phase separated upper and lower layer when investigated using H-NMR. The lower layer contained 4 times more DOL than DME, while the upper layer contained 25 times more DOL than DME. Further, the poly-DOL peaks are only in the top layer of the solution after 24 hours. The complexation of DME with Mg may prevent Mg from acting as the catalyst for the cationic ring-opening polymerization reaction, especially if it is concentrated in the lower layer of the solution. A proposed mechanism for the ring-opening polymerization of DOL is shown in Figure 5.6. If the DME prevents the first step where Mg interacts with the DOL to induce the ring-opening, it is possible that is why polymerization is much slower in the case of 1:7 DME/DOL solvents or hindered in 1:1 DME/DOL solvent mixtures.

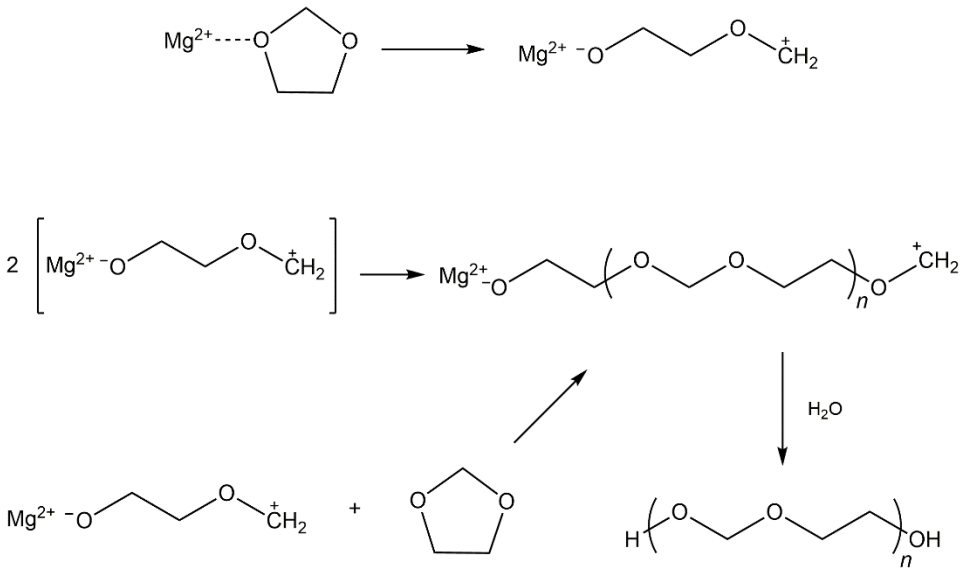

Figure 5.6 Proposed reaction mechanism for $Mg(TFSI)_2$ with DOL ($TFSI^-$ anions omitted for simplification

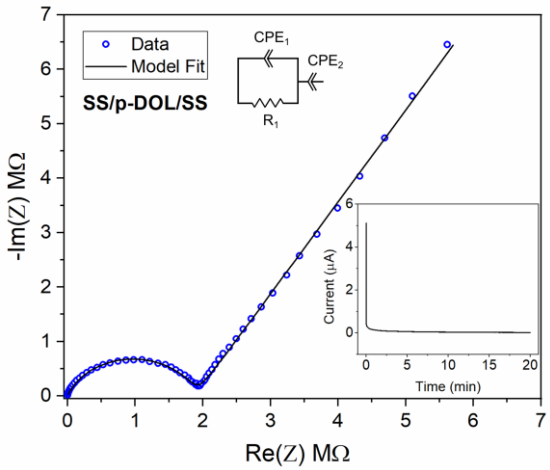

Figure 5.7 Nyquist Impedance plot for Mg-DOL (0.125M $Mg(TFSI)_2$ + 0.25 M $Mg(ClO_4)_2$ in DOL) polymer sandwiched between two stainless steel disks. The inset displays the current vs. time plot for the same cell when a 2 V bias was applied for 20 minutes.

One application for this poly-DOL synthesized using Mg salts is in polymer electrolytes, more specifically a solid electrolyte formed via in-situ polymerization.[143] This type of polymer electrolyte could help decrease interfacial contact resistance from rough or incompatible free-standing polymer gels with electrode interfaces. To test the ionic conductivity of the Mg-DOL electrolyte, an electrolyte solution with 0.125 M $Mg(TFSI)_2$ and 0.25 M $Mg(ClO_4)_2$ in DOL was mixed and drop casted onto stainless steel blocking electrodes. This concentration of $Mg(TFSI)_2$ catalyst is high to help the polymer firm up to close in the coin cell, which may account for its low ionic conductivity.[147] These electrodes were sandwiched after the polymer had begun to harden and closed in a coin cell without a separator. The electrochemical impedance spectra can be seen in Figure 5.7. The ionic conductivity was 2.6×10^{-9} S/cm at room temperature (20 °C). Potential hold tests in the inset demonstrate low electronic conductivity of about 9.2×10^{-11} S/cm. It is important to note that the EIS was recorded

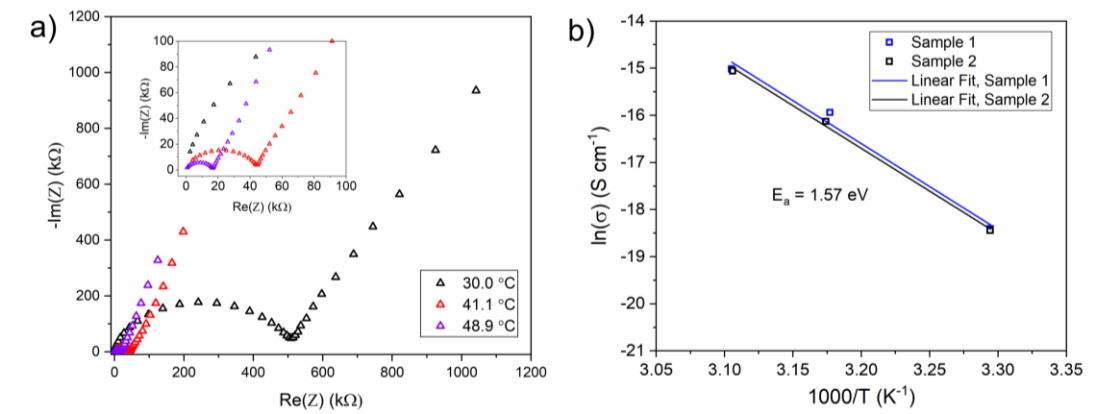

Figure 5.8 Temperature measurements of poly-DOL a) Nyquist impedance plots for p-DOL (0.125M $Mg(TFSI)_2$ + 0.25 M $Mg(ClO_4)_2$ in DOL) between two stainless steel electrodes at different temperatures, at frequencies from 50 kHz to 100 mHz with 100 mV amplitude, and b) is the activation energy calculated for two different samples (the EIS data in (a) is from Sample 1).

on a completely polymerized sample with a high concentration of catalyst, which previous studies demonstrated can decrease the ionic conductivity.[147] Decreasing the amount of $Mg(TFSI)_2$ and optimizing the composition could increase ionic conductivity. To further characterize the polymer, temperature studies were completed, and the results are in Figure 5.8. The ionic conductivity increases even upon a modest increase in temperature to 30 °C. Although the activation energy is high at 1.57 eV, this test is only an initial proof of concept, and more characterization and study are underway to optimize the polymer's properties and ionic conductivity.

5.4. Conclusions

In conclusion, strong Lewis acid cations such as Al^{3+} and Mg^{2+} can catalyze DOL polymerization and their Lewis acidity, and ability to catalyze the reaction, is influenced by the associated anion. It was determined that the order of reactivity for Mg salts based on the anion was $TFSI^-$ > OTf^- > ClO_4^-, and we propose this difference is based on the affinity of this anion to coordinate with Mg^{2+} and affect its Lewis

acidity. We determined other factors that may hinder its reactivity, such as ion solvation with secondary solvents. These discoveries could help expand the applications of Lewis acid catalysts in polymerization reactions and give insight into the importance of the properties of metal salts. These insights may also be critical in deciding whether to utilize DOL as a solvent for Mg battery systems and what electrolyte compositions may be ideal. Further, poly-DOL demonstrated ionic conductivity which if improved could indicate its use as a polymer electrolyte in Mg battery systems.

Chapter 6: Summary and Outlook

6.1. Summary

The overall goal of this dissertation was to investigate fundamental properties of MnO_2 cathodes and Mg metal anodes, particularly focusing on surface and interface characteristics, to develop basic understandings of both chemical and electrochemical mechanisms governing their performance. Further, through this improved understanding, the work in this dissertation aims to move toward finding an effective way to integrate Mg metal and a metal oxide cathode in a full-cell Mg battery. Ultimately, this system would contain a water-activated MnO_2 cathode and protected Mg metal anode in a conventional Mg electrolyte or a solid-state electrolyte.

In Chapter 2, the charge storage mechanism of MnO_2 in a water-containing electrolyte was studied using XPS. The results demonstrated that water is critical to the improved Mg^{2+} insertion kinetics, and water must either be present in the electrolyte or within the cathode as structural water for the improvement to be maintained. The reaction mechanism was also proposed to be a combination of Mg^{2+} insertion combined with a conversion reaction to MnO_2. By understanding how water participates in the reaction, it may be possible to utilize the activated cathode in a full-cell battery if an anode can be appropriately developed that is compatible.

Chapter 3 detailed further study of MnO_2 and how modifications to its structure and electronic conductivity via a PEDOT surface layer impacted its performance. The PEDOT layer did not hinder Mg^{2+} transport at moderate thicknesses (10-45 nm), and the increased electronic conductivity along the nanowire improved material utilization

and power performance, with small improvements to cyclability. The charge storage mechanism seems to be consistent regardless of the PEDOT layer, with all samples showing high surface-dominant capacity. These results demonstrate that having improved electronic conductivity does help MnO_2 performance, and that surface layers may be applicable for protection at the MnO_2 cathode interface as long as they conduct Mg ions. These observations can help in the design of better Mg cathodes, although the impact of the PEDOT on the water-activation of MnO_2 has not been fully explored.

Transitioning to the anode side of the battery, Chapter 4 discussed the possibility for utilizing ALD Al_2O_3 as a protection layer for Mg metal anodes. Both evaporated Mg and Mg foil were able to be utilized as substrates, although it was unclear what the role of slightly different MgO content as well as surface roughness played in the different electrochemical performance of these materials. Al_2O_3 was able to be deposited on Mg using ALD, and it protected the anode from electrolyte degradation upon soaking, however the layer was not able to withstand electrochemical cycling. Mg deposits were visualized on top of the Al_2O_3 layer, and most of the symmetric cells likely experienced soft shorting. Despite the poor performance of this protection layer, these results can inform future studies of Mg anode protection and how to design more appropriate materials for artificial SEI layers.

In Chapter 5, a unique catalytic polymerization reaction was investigated in Mg battery electrolytes containing 1,3-dioxolane. Salts containing Mg^{2+} and weakly coordinating anions such as $TFSI^-$ and OTf^- demonstrated the ability to polymerize DOL. The reaction may be important for systems utilizing DOL in the electrolytes, as this polymer may form on the electrode surfaces. However, it was determined that this

phenomenon likely has not been discovered in RMB previously due to the prevalence of complex salts in RMB electrolytes. If the Mg^{2+} ion is not free to coordinate with DOL, the polymerization may not occur. A future application for this polymer could also be as a solid polymer electrolyte. Although initial studies of the ionic conductivity indicate a low value, further optimization could enable this polymer to be used as a solid electrolyte.

6.2. Outlook

The work in this dissertation demonstrates the importance of understanding the fundamental chemical and electrochemical processes underpinning the performance of cathode, anode, and electrolyte materials for RMB. Building upon the research here, there are many next possible steps to take in moving toward creating a full-cell RMB with a high voltage MnO_2 cathode and Mg metal anode. While the performance of the MnO_2 cathode is not exemplary, it is still an excellent starting cathode material to use in a proof-of-concept technology. Pure MnO_2 or coaxial PEDOT/MnO_2 nanowires could be use in two possible systems stemming from the results included above:

1) A battery consisting of a protected Mg metal anode, conventional Mg electrolyte, and MnO_2 cathode.
2) A battery with a Mg metal anode, solid Mg-DOL polymer electrolyte, and MnO_2 cathode.

The work needed to realize the above mentioned technologies would likely need to include either further ALD material development for a Mg^{2+} ion conductive protective layer, or the development of a chemically formed protective layer such as one

electrochemically formed using DOL. Additionally, if the Mg-DOL polymer electrolyte from chapter 5 can be optimized to create higher ionic conductivity, fully characterized, and has a sufficiently wide electrochemical stability window, this electrolyte could also be applied in a full-cell RMB with an MnO_2 cathode. There are certainly many other possible routes to choose to improve RMB, as this field is still battling many scientific challenges to fully develop a technology that could be commercialized, but the two possibilities included here represent the most plausible next steps in building upon the work described in this dissertation.

Bibliography

1. Yoshino, A., The Birth of the Lithium-Ion Battery. *Angewandte Chemie International Edition* **2012,** *51* (24), 5798-5800.
2. Mizushima, K.; Jones, P. C.; Wiseman, P. J.; Goodenough, J. B., LixCoO2 (0<x<-1): A new cathode material for batteries of high energy density. *Materials Research Bulletin* **1980,** *15* (6), 783-789.
3. Zu, C.-X.; Li, H., Thermodynamic analysis on energy densities of batteries. *Energy & Environmental Science* **2011,** *4* (8), 2614-2624.
4. Muldoon, J.; Bucur, C. B.; Gregory, T., Quest for Nonaqueous Multivalent Secondary Batteries: Magnesium and Beyond. *Chemical Reviews* **2014,** *114* (23), 11683-11720.
5. Aurbach, D., Review of selected electrode–solution interactions which determine the performance of Li and Li ion batteries. *Journal of Power Sources* **2000,** *89* (2), 206-218.
6. Huie, M. M.; Bock, D. C.; Takeuchi, E. S.; Marschilok, A. C.; Takeuchi, K. J., Cathode materials for magnesium and magnesium-ion based batteries. *Coordination Chemistry Reviews* **2015,** *287*, 15 - 27.
7. Salama, M.; Rosy; Attias, R.; Yemini, R.; Gofer, Y.; Aurbach, D.; Noked, M., Metal–Sulfur Batteries: Overview and Research Methods. *ACS Energy Letters* **2019,** *4* (2), 436-446.
8. Kong, L.; Yan, C.; Huang, J.-Q.; Zhao, M.-Q.; Titirici, M.-M.; Xiang, R.; Zhang, Q., A Review of Advanced Energy Materials for Magnesium–Sulfur Batteries. *ENERGY & ENVIRONMENTAL MATERIALS* **2018,** *1* (3), 100-112.
9. Zhang, T.; Tao, Z.; Chen, J., Magnesium–air batteries: from principle to application. *Materials Horizons* **2014,** *1* (2), 196-206.
10. Yao, X.; Luo, J.; Dong, Q.; Wang, D., A rechargeable non-aqueous Mg-Br2 battery. *Nano Energy* **2016,** *28*, 440-446.
11. Tian, H.; Gao, T.; Li, X.; Wang, X.; Luo, C.; Fan, X.; Yang, C.; Suo, L.; Ma, Z.; Han, W.; Wang, C., High power rechargeable magnesium/iodine battery chemistry. *Nature Communications* **2017,** *8*, 14083.
12. Gao, T.; Ji, X.; Hou, S.; Fan, X.; Li, X.; Yang, C.; Han, F.; Wang, F.; Jiang, J.; Xu, K.; Wang, C., Thermodynamics and Kinetics of Sulfur Cathode during Discharge in MgTFSI2–DME Electrolyte. *Advanced Materials* **2017,** *30* (3), 1704313.
13. Gao, T.; Noked, M.; Pearse, A. J.; Gillette, E.; Fan, X.; Zhu, Y.; Luo, C.; Suo, L.; Schroeder, M. A.; Xu, K.; Lee, S. B.; Rubloff, G. W.; Wang, C., Enhancing the Reversibility of Mg/S Battery Chemistry through Li+ Mediation. *Journal of the American Chemical Society* **2015,** *137* (38), 12388-12393.
14. Zhao-Karger, Z.; Zhao, X.; Wang, D.; Diemant, T.; Behm, R. J.; Fichtner, M., Performance Improvement of Magnesium Sulfur Batteries with Modified Non-Nucleophilic Electrolytes. *Advanced Energy Materials* **2014,** *5* (3), 1401155.
15. Robba, A.; Vizintin, A.; Bitenc, J.; Mali, G.; Arčon, I.; Kavčič, M.; Žitnik, M.; Bučar, K.; Aquilanti, G.; Martineau-Corcos, C.; Randon-Vitanova, A.; Dominko,

R., Mechanistic Study of Magnesium–Sulfur Batteries. *Chemistry of Materials* **2017,** *29* (21), 9555-9564.
16. Kolosnitsyn, V. S.; Karaseva, E. V., Lithium-sulfur batteries: Problems and solutions. *Russian Journal of Electrochemistry* **2008,** *44* (5), 506-509.
17. Arthur, T. S.; Singh, N.; Matsui, M., Electrodeposited Bi, Sb and Bi 1-xSb x alloys as anodes for Mg-ion batteries. *Electrochemistry Communications* **2012,** *16* (1), 103--105.
18. Shao, Y.; Gu, M.; Li, X.; Nie, Z.; Zuo, P.; Li, G.; Liu, T.; Xiao, J.; Cheng, Y.; Wang, C.; Zhang, J. G.; Liu, J., Highly reversible Mg insertion in nanostructured Bi for Mg ion batteries. *Nano Letters* **2014,** *14* (1), 255--260.
19. Benmayza, A.; Ramanathan, M.; Singh, N.; Mizuno, F.; Prakash, J., Electrochemical and Thermal Studies of Bismuth Electrodes for Magnesium-Ion Cells. *J. Electrochem. Soc.* **2015,** *162* (8), A1630--A1635.
20. Singh, N.; Arthur, T. S.; Ling, C.; Matsui, M.; Mizuno, F., A high energy-density tin anode for rechargeable magnesium-ion batteries. *Chemical Communications* **2013,** *49* (2), 149-151.
21. Wang, Z.; Su, Q.; Shi, J.; Deng, H.; Yin, G. Q.; Guan, J.; Wu, M. P.; Zhou, Y. L.; Lou, H. L.; Fu, Y. Q., Comparison of tetragonal and cubic tin as anode for Mg ion batteries. *ACS Applied Materials and Interfaces* **2014,** *6* (9), 6786--6789.
22. Parent, L. R.; Cheng, Y.; Sushko, P. V.; Shao, Y.; Liu, J.; Wang, C.-M.; Browning, N. D., Realizing the Full Potential of Insertion Anodes for Mg-Ion Batteries Through the Nanostructuring of Sn. *Nano Letters* **2015,** *15* (2), 1177--1182.
23. Niu, J.; Yin, K.; Gao, H.; Song, M.; Ma, W.; Peng, Z.; Zhang, Z., Composition- and size-modulated porous bismuth–tin biphase alloys as anodes for advanced magnesium ion batteries. *Nanoscale* **2019,** *11* (32), 15279-15288.
24. Song, M.; Zhang, T.; Niu, J.; Gao, H.; Shi, Y.; Zhang, Y.; Ma, W.; Zhang, Z., Boosting electrochemical reactivity of tin as an anode for Mg ion batteries through introduction of second phase. *Journal of Power Sources* **2020,** *451*, 227735.
25. Blondeau, L.; Foy, E.; Khodja, H.; Gauthier, M., Unexpected Behavior of the InSb Alloy in Mg-Ion Batteries: Unlocking the Reversibility of Sb. *The Journal of Physical Chemistry C* **2019,** *123* (2), 1120-1126.
26. Malyi, O. I.; Tan, T. L.; Manzhos, S., In search of high performance anode materials for Mg batteries: Computational studies of Mg in Ge, Si, and Sn. *Journal of Power Sources* **2013,** *233*, 341-345.
27. Singh, N. a. A. T. S. a. L. C. a. M. M. a. M. F., A high energy-density tin anode for rechargeable magnesium-ion batteries. *Chemical communications (Cambridge, England)* **2013,** *49* (2), 149--51.
28. Bachhav, M. N.; Hahn, N. T.; Zavadil, K. R.; Nelson, E. G.; Crowe, A. J.; Bartlett, B. M.; Chu, P.-W.; Araullo-Peters, V. J.; Marquis, E. A., Microstructure and Chemistry of Electrodeposited Mg Films. *Journal of The Electrochemical Society* **2016,** *163* (13), D645-D650.
29. Ling, C.; Banerjee, D.; Matsui, M., Study of the electrochemical deposition of Mg in the atomic level: Why it prefers the non-dendritic morphology. *Electrochimica Acta* **2012,** *76*, 270-274.

30. Hu, X.-C.; Shi, Y.; Lang, S.-Y.; Zhang, X.; Gu, L.; Guo, Y.-G.; Wen, R.; Wan, L.-J., Direct insights into the electrochemical processes at anode/electrolyte interfaces in magnesium-sulfur batteries. *Nano Energy* **2018,** *49*, 453-459.
31. Matsui, M., Study on electrochemically deposited Mg metal. *Journal of Power Sources* **2011,** *196* (16), 7048-7055.
32. Ding, M. S.; Diemant, T.; Behm, R. J.; Passerini, S.; Giffin, G. A., Dendrite Growth in Mg Metal Cells Containing Mg(TFSI)2/Glyme Electrolytes. *Journal of The Electrochemical Society* **2018,** *165* (10), A1983-A1990.
33. Davidson, R.; Verma, A.; Santos, D.; Hao, F.; Fincher, C.; Xiang, S.; Van Buskirk, J.; Xie, K.; Pharr, M.; Mukherjee, P. P.; Banerjee, S., Formation of Magnesium Dendrites during Electrodeposition. *ACS Energy Letters* **2019,** *4* (2), 375-376.
34. Lu, Z.; Schechter, A.; Moshkovich, M.; Aurbach, D., On the electrochemical behavior of magnesium electrodes in polar aprotic electrolyte solutions. *Journal of Electroanalytical Chemistry* **1999,** *466* (2), 203-217.
35. Aurbach, D.; Gofer, Y.; Schechter, A.; Chusid, O.; Gizbar, H.; Cohen, Y.; Moshkovich, M.; Turgeman, R., A comparison between the electrochemical behavior of reversible magnesium and lithium electrodes. *Journal of Power Sources* **2001,** *97–98*, 269 - 273.
36. Connell, J. G.; Genorio, B.; Lopes, P. P.; Strmcnik, D.; Stamenkovic, V. R.; Markovic, N. M., Tuning the Reversibility of Mg Anodes via Controlled Surface Passivation by H2O/Cl– in Organic Electrolytes. *Chemistry of Materials* **2016,** *28* (22), 8268-8277.
37. Rodríguez-Pérez, I. A.; Yuan, Y.; Bommier, C.; Wang, X.; Ma, L.; Leonard, D. P.; Lerner, M. M.; Carter, R. G.; Wu, T.; Greaney, P. A.; Lu, J.; Ji, X., Mg-Ion Battery Electrode: An Organic Solid's Herringbone Structure Squeezed upon Mg-Ion Insertion. *Journal of the American Chemical Society* **2017,** *139* (37), 13031-13037.
38. Vizintin, A.; Bitenc, J.; Kopač Lautar, A.; Pirnat, K.; Grdadolnik, J.; Stare, J.; Randon-Vitanova, A.; Dominko, R., Probing electrochemical reactions in organic cathode materials via in operando infrared spectroscopy. *Nature Communications* **2018,** *9* (1), 661.
39. Fan, X.; Wang, F.; Ji, X.; Wang, R.; Gao, T.; Hou, S.; Chen, J.; Deng, T.; Li, X.; Chen, L.; Luo, C.; Wang, L.; Wang, C., A Universal Organic Cathode for Ultrafast Lithium and Multivalent Metal Batteries. *Angewandte Chemie International Edition* **2018,** *57* (24), 7146-7150.
40. Muldoon, J.; Bucur, C. B.; Oliver, A. G.; Sugimoto, T.; Matsui, M.; Kim, H. S.; Allred, G. D.; Zajicek, J.; Kotani, Y., Electrolyte roadblocks to a magnesium rechargeable battery. *Energy & Environmental Science* **2012,** *5* (3), 5941.
41. Song, J.; Sahadeo, E.; Noked, M.; Lee, S. B., Mapping the Challenges of Magnesium Battery. *The Journal of Physical Chemistry Letters* **2016,** *7* (9), 1736-1749.
42. Rajput, N. N.; Qu, X.; Sa, N.; Burrell, A. K.; Persson, K. A., The Coupling between Stability and Ion Pair Formation in Magnesium Electrolytes from First-Principles Quantum Mechanics and Classical Molecular Dynamics. *Journal of the American Chemical Society* **2015,** *137* (9), 3411-3420.

43. Tutusaus, O.; Mohtadi, R.; Arthur, T. S.; Mizuno, F.; Nelson, E. G.; Sevryugina, Y. V., An Efficient Halogen-Free Electrolyte for Use in Rechargeable Magnesium Batteries. *Angewandte Chemie International Edition* **2015,** *54* (27), 7900-7904.
44. McArthur, S. G.; Geng, L.; Guo, J.; Lavallo, V., Cation reduction and comproportionation as novel strategies to produce high voltage, halide free, carborane based electrolytes for rechargeable Mg batteries. *Inorganic Chemistry Frontiers* **2015,** *2* (12), 1101-1104.
45. McArthur, S. G.; Jay, R.; Geng, L.; Guo, J.; Lavallo, V., Below the 12-vertex: 10-vertex carborane anions as non-corrosive, halide free, electrolytes for rechargeable Mg batteries. *Chemical Communications* **2017,** *53* (32), 4453-4456.
46. Lau, K.-C.; Seguin, T. J.; Carino, E. V.; Hahn, N. T.; Connell, J. G.; Ingram, B. J.; Persson, K. A.; Zavadil, K. R.; Liao, C., Widening Electrochemical Window of Mg Salt by Weakly Coordinating Perfluoroalkoxyaluminate Anion for Mg Battery Electrolyte. *Journal of The Electrochemical Society* **2019,** *166* (8), A1510-A1519.
47. Herb, J. T.; Nist-Lund, C. A.; Arnold, C. B., A Fluorinated Alkoxyaluminate Electrolyte for Magnesium-Ion Batteries. *ACS Energy Letters* **2016,** *1* (6), 1227-1232.
48. Kim, S. S.; Bevilacqua, S. C.; See, K. A., Conditioning-Free Mg Electrolyte by the Minor Addition of Mg(HMDS)2. *ACS Applied Materials & Interfaces* **2020,** *12* (5), 5226-5233.
49. Kang, S.-J.; Kim, H.; Hwang, S.; Jo, M.; Jang, M.; Park, C.; Hong, S.-T.; Lee, H., Electrolyte Additive Enabling Conditioning-Free Electrolytes for Magnesium Batteries. *ACS Applied Materials & Interfaces* **2019,** *11* (1), 517-524.
50. Arthur, T. S.; Glans, P.-A.; Singh, N.; Tutusaus, O.; Nie, K.; Liu, Y.-S.; Mizuno, F.; Guo, J.; Alsem, D. H.; Salmon, N. J.; Mohtadi, R., Interfacial Insight from Operando XAS/TEM for Magnesium Metal Deposition with Borohydride Electrolytes. *Chemistry of Materials* **2017,** *29* (17), 7183-7188.
51. Ha, S.-Y.; Lee, Y.-W.; Woo, S. W.; Koo, B.; Kim, J.-S.; Cho, J.; Lee, K. T.; Choi, N.-S., Magnesium(II) Bis(trifluoromethane sulfonyl) Imide-Based Electrolytes with Wide Electrochemical Windows for Rechargeable Magnesium Batteries. *ACS Applied Materials & Interfaces* **2014,** *6* (6), 4063-4073.
52. Shterenberg, I.; Salama, M.; Yoo, H. D.; Gofer, Y.; Park, J.-B.; Sun, Y.-K.; Aurbach, D., Evaluation of (CF3SO2)2N− (TFSI) Based Electrolyte Solutions for Mg Batteries. *Journal of The Electrochemical Society* **2015,** *162* (13), A7118-A7128.
53. Yoo, H. D.; Han, S.-D.; Bolotin, I. L.; Nolis, G. M.; Bayliss, R. D.; Burrell, A. K.; Vaughey, J. T.; Cabana, J., Degradation Mechanisms of Magnesium Metal Anodes in Electrolytes Based on (CF3SO2)2N– at High Current Densities. *Langmuir* **2017,** *33* (37), 9398-9406.
54. Tutusaus, O.; Mohtadi, R.; Singh, N.; Arthur, T. S.; Mizuno, F., Study of Electrochemical Phenomena Observed at the Mg Metal/Electrolyte Interface. *ACS Energy Letters* **2017,** *2* (1), 224-229.
55. Rajput, N. N.; Seguin, T. J.; Wood, B. M.; Qu, X.; Persson, K. A., Elucidating Solvation Structures for Rational Design of Multivalent Electrolytes—A Review. *Topics in Current Chemistry* **2018,** *376* (3), 19.
56. Yu, Y.; Baskin, A.; Valero-Vidal, C.; Hahn, N. T.; Liu, Q.; Zavadil, K. R.; Eichhorn, B. W.; Prendergast, D.; Crumlin, E. J., Instability at the

Electrode/Electrolyte Interface Induced by Hard Cation Chelation and Nucleophilic Attack. *Chemistry of Materials* **2017,** *29* (19), 8504-8512.
57. Muldoon, J.; Bucur, C. B.; Oliver, A. G.; Zajicek, J.; Allred, G. D.; Boggess, W. C., Corrosion of magnesium electrolytes: chlorides – the culprit. *Energy \& Environmental Science* **2013,** *6* (2), 482.
58. Lowe, J. S.; Siegel, D. J., Reaction Pathways for Solvent Decomposition on Magnesium Anodes. *The Journal of Physical Chemistry C* **2018,** *122* (20), 10714-10724.
59. Gao, T.; Hou, S.; Huynh, K.; Wang, F.; Eidson, N.; Fan, X.; Han, F.; Luo, C.; Mao, M.; Li, X.; Wang, C., Existence of Solid Electrolyte Interphase in Mg Batteries: Mg/S Chemistry as an Example. *ACS Applied Materials & Interfaces* **2018**.
60. Li, X.; Gao, T.; Han, F.; Ma, Z.; Fan, X.; Hou, S.; Eidson, N.; Li, W.; Wang, C., Reducing Mg Anode Overpotential via Ion Conductive Surface Layer Formation by Iodine Additive. *Advanced Energy Materials* **2018,** *8* (7), 1701728.
61. Son, S.-B.; Gao, T.; Harvey, S. P.; Steirer, K. X.; Stokes, A.; Norman, A.; Wang, C.; Cresce, A.; Xu, K.; Ban, C., An artificial interphase enables reversible magnesium chemistry in carbonate electrolytes. *Nature Chemistry* **2018**.
62. Rong, Z.; Malik, R.; Canepa, P.; Sai Gautam, G.; Liu, M.; Jain, A.; Persson, K.; Ceder, G., Materials Design Rules for Multivalent Ion Mobility in Intercalation Structures. *Chemistry of Materials* **2015,** *27* (17), 6016-6021.
63. Shannon, R. D., Revised effective ionic radii and systematic studies of interatomic distances in halides and chalcogenides. *Acta Cryst.* **1976,** *A32*, 751-767.
64. Aurbach, D.; Lu, Z.; Schechter, A.; Gofer, Y.; Gizbar, H.; Turgeman, R.; Cohen, Y.; Moshkovich, M.; Levi, E., Prototype systems for rechargeable magnesium batteries. *Nature* **2000,** *407* (6805), 724.
65. Mao, M.; Gao, T.; Hou, S.; Wang, C., A critical review of cathodes for rechargeable Mg batteries. *Chemical Society Reviews* **2018,** *47* (23), 8804-8841.
66. Wan, L. F.; Perdue, B. R.; Apblett, C. A.; Prendergast, D., Mg Desolvation and Intercalation Mechanism at the Mo6S8 Chevrel Phase Surface. *Chemistry of Materials* **2015,** *27* (17), 5932-5940.
67. Wan, L. F.; Prendergast, D., Ion-Pair Dissociation on α-MoO3 Surfaces: Focus on the Electrolyte–Cathode Compatibility Issue in Mg Batteries. *The Journal of Physical Chemistry C* **2018,** *122* (1), 398-405.
68. Sun, X.; Bonnick, P.; Nazar, L. F., Layered TiS2 Positive Electrode for Mg Batteries. *ACS Energy Letters* **2016,** *1* (1), 297-301.
69. Sun, X.; Bonnick, P.; Duffort, V.; Liu, M.; Rong, Z.; Persson, K. A.; Ceder, G.; Nazar, L. F., A high capacity thiospinel cathode for Mg batteries. *Energy & Environmental Science* **2016,** *9* (7), 2273-2277.
70. Li, Z.; Mu, X.; Zhao-Karger, Z.; Diemant, T.; Behm, R. J.; Kübel, C.; Fichtner, M., Fast kinetics of multivalent intercalation chemistry enabled by solvated magnesium-ions into self-established metallic layered materials. *Nature Communications* **2018,** *9* (1), 5115.
71. Bonnick, P.; Blanc, L.; Vajargah, S. H.; Lee, C.-W.; Sun, X.; Balasubramanian, M.; Nazar, L. F., Insights into Mg2+ Intercalation in a Zero-Strain Material: Thiospinel MgxZr2S4. *Chemistry of Materials* **2018,** *30* (14), 4683-4693.

72. Mao, M.; Ji, X.; Hou, S.; Gao, T.; Wang, F.; Chen, L.; Fan, X.; Chen, J.; Ma, J.; Wang, C., Tuning Anionic Chemistry To Improve Kinetics of Mg Intercalation. *Chemistry of Materials* **2019,** *31* (9), 3183-3191.
73. Canepa, P.; Sai Gautam, G.; Hannah, D. C.; Malik, R.; Liu, M.; Gallagher, K. G.; Persson, K. A.; Ceder, G., Odyssey of Multivalent Cathode Materials: Open Questions and Future Challenges. *Chemical Reviews* **2017,** *117* (5), 4287-4341.
74. Novák, P.; Desilvestro, J., Electrochemical Insertion of Magnesium in Metal Oxides and Sulfides from Aprotic Electrolytes. *Journal of The Electrochemical Society* **1993,** *140* (1), 140-144.
75. Song, J.; Noked, M.; Gillette, E.; Duay, J.; Rubloff, G.; Lee, S. B., Activation of a MnO2 cathode by water-stimulated Mg2+ insertion for a magnesium ion battery. *Physical Chemistry Chemical Physics* **2015,** *17* (7), 5256-5264.
76. Sun, X.; Duffort, V.; Mehdi, B. L.; Browning, N. D.; Nazar, L. F., Investigation of the Mechanism of Mg Insertion in Birnessite in Nonaqueous and Aqueous Rechargeable Mg-Ion Batteries. *Chemistry of Materials* **2016,** *28* (2), 534-542.
77. Yin, J.; Brady, A. B.; Takeuchi, E. S.; Marschilok, A. C.; Takeuchi, K. J., Magnesium-ion battery-relevant electrochemistry of MgMn2O4: crystallite size effects and the notable role of electrolyte water content. *Chemical Communications* **2017,** *53* (26), 3665-3668.
78. Wang, F.; Sun, W.; Shadike, Z.; Hu, E.; Ji, X.; Gao, T.; Yang, X.-Q.; Xu, K.; Wang, C., How Water Accelerates Bivalent Ion Diffusion at the Electrolyte/Electrode Interface. *Angewandte Chemie International Edition* **2018,** *57* (37), 11978-11981.
79. Ji, X.; Chen, J.; Wang, F.; Sun, W.; Ruan, Y.; Miao, L.; Jiang, J.; Wang, C., Water-Activated VOPO4 for Magnesium Ion Batteries. *Nano Letters* **2018,** *18* (10), 6441-6448.
80. Lee Hyeon, J.; Shin, J.; Choi Jang, W., Intercalated Water and Organic Molecules for Electrode Materials of Rechargeable Batteries. *Advanced Materials* **2018,** *0* (0), 1705851.
81. Mitchell, J. B.; Lo, W. C.; Genc, A.; LeBeau, J.; Augustyn, V., Transition from Battery to Pseudocapacitor Behavior via Structural Water in Tungsten Oxide. *Chemistry of Materials* **2017,** *29* (9), 3928-3937.
82. Wang, R.; Chung, C.-C.; Liu, Y.; Jones, J. L.; Augustyn, V., Electrochemical Intercalation of Mg2+ into Anhydrous and Hydrated Crystalline Tungsten Oxides. *Langmuir* **2017,** *33* (37), 9314-9323.
83. Attias, R.; Salama, M.; Hirsch, B.; Pant, R.; Gofer, Y.; Aurbach, D., Anion Effects on Cathode Electrochemical Activity in Rechargeable Magnesium Batteries: A Case Study of V2O5. *ACS Energy Letters* **2019,** *4* (1), 209-214.
84. Attias, R.; Salama, M.; Hirsch, B.; Gofer, Y.; Aurbach, D., Solvent Effects on the Reversible Intercalation of Magnesium-Ions into V2O5 Electrodes. *ChemElectroChem* **2018,** *5* (22), 3514-3524.
85. Parija, A.; Prendergast, D.; Banerjee, S., Evaluation of Multivalent Cation Insertion in Single- and Double-Layered Polymorphs of V2O5. *ACS Applied Materials & Interfaces* **2017,** *9* (28), 23756-23765.

86. Wang, Z.; Su, Q.; Deng, H., Single-layered V2O5 a promising cathode material for rechargeable Li and Mg ion batteries: an ab initio study. *Physical Chemistry Chemical Physics* **2013,** *15* (22), 8705-8709.
87. Gautam, G. S.; Canepa, P.; Malik, R.; Liu, M.; Persson, K.; Ceder, G., First-principles evaluation of multi-valent cation insertion into orthorhombic V2O5. *Chemical Communications* **2015,** *51* (71), 13619-13622.
88. Dudney, N. J.; Jang, Y.-I., Analysis of thin-film lithium batteries with cathodes of 50 nm to 4 μm thick LiCoO2. *Journal of Power Sources* **2003,** *119-121*, 300-304.
89. Gershinsky, G.; Yoo, H. D.; Gofer, Y.; Aurbach, D., Electrochemical and Spectroscopic Analysis of Mg2+ Intercalation into Thin Film Electrodes of Layered Oxides: V2O5 and MoO3. *Langmuir* **2013,** *29* (34), 10964-10972.
90. Liu, R.; Duay, J.; Lee, S. B., Heterogeneous nanostructured electrode materials for electrochemical energy storage. *Chemical Communications* **2011,** *47* (5), 1384-1404.
91. Song, J. Investigation of Magnesium Ion Charge Storage Mechanism in Manganese Dioxide. University of Maryland, 2016.
92. Thackeray, M. M., Manganese oxides for lithium batteries. *Progress in Solid State Chemistry* **1997,** *25* (1–2), 1-71.
93. Nam, K. W.; Kim, H.; Choi, J. H.; Choi, J. W., Crystal water for high performance layered manganese oxide cathodes in aqueous rechargeable zinc batteries. *Energy & Environmental Science* **2019,** *12* (6), 1999-2009.
94. Han, S.-D.; Kim, S.; Li, D.; Petkov, V.; Yoo, H. D.; Phillips, P. J.; Wang, H.; Kim, J. J.; More, K. L.; Key, B.; Klie, R. F.; Cabana, J.; Stamenkovic, V. R.; Fister, T. T.; Markovic, N. M.; Burrell, A. K.; Tepavcevic, S.; Vaughey, J. T., Mechanism of Zn Insertion into Nanostructured δ-MnO2: A Nonaqueous Rechargeable Zn Metal Battery. *Chemistry of Materials* **2017,** *29* (11), 4874-4884.
95. Julien, C.; Massot, M.; Baddour-Hadjean, R.; Franger, S.; Bach, S.; Pereira-Ramos, J. P., Raman spectra of birnessite manganese dioxides. *Solid State Ionics* **2003,** *159* (3–4), 345-356.
96. Pang, S.-C.; Anderson, M. A.; Chapman, T. W., Novel Electrode Materials for Thin-Film Ultracapacitors: Comparison of Electrochemical Properties of Sol-Gel-Derived and Electrodeposited Manganese Dioxide. *Journal of The Electrochemical Society* **2000,** *147* (2), 444.
97. Yin, B.; Zhang, S.; Jiang, H.; Qu, F.; Wu, X., Phase-controlled synthesis of polymorphic MnO2 structures for electrochemical energy storage. *Journal of Materials Chemistry A* **2015,** *3* (10), 5722-5729.
98. Chang, J.-K.; Tsai, W.-T., Material Characterization and Electrochemical Performance of Hydrous Manganese Oxide Electrodes for Use in Electrochemical Pseudocapacitors. *Journal of The Electrochemical Society* **2003,** *150* (10), A1333.
99. Kitchaev, D. A.; Dacek, S. T.; Sun, W.; Ceder, G., Thermodynamics of Phase Selection in MnO2 Framework Structures through Alkali Intercalation and Hydration. *Journal of the American Chemical Society* **2017,** *139* (7), 2672-2681.
100. Ling, C.; Zhang, R.; Mizuno, F., Quantitatively Predict the Potential of MnO2 Polymorphs as Magnesium Battery Cathodes. *ACS Applied Materials & Interfaces* **2016,** *8* (7), 4508-4515.

101. Le, M.; Liu, Y.; Wang, H.; Dutta, R. K.; Yan, W.; Hemminger, J. C.; Wu, R. Q.; Penner, R. M., In Situ Electrical Conductivity of LixMnO2 Nanowires as a Function of x and Size. *Chemistry of Materials* **2015,** *27* (9), 3494-3504.
102. Song, J.; Duay, J.; Gillette, E.; Lee, S. B., The reversible anomalous high lithium capacity of MnO2 nanowires. *Chemical Communications* **2014,** *50* (55), 7352-7355.
103. Duay, J.; Sherrill, S. A.; Gui, Z.; Gillette, E.; Lee, S. B., Self-Limiting Electrodeposition of Hierarchical MnO2 and M(OH)2/MnO2 Nanofibril/Nanowires: Mechanism and Supercapacitor Properties. *ACS Nano* **2013,** *7* (2), 1200-1214.
104. Liu, R.; Duay, J.; Lee, S. B., Electrochemical Formation Mechanism for the Controlled Synthesis of Heterogeneous MnO2/Poly(3,4-ethylenedioxythiophene) Nanowires. *ACS Nano* **2011,** *5* (7), 5608-5619.
105. Gillette, E. I.; Kim, N.; Rubloff, G. W.; Lee, S. B., Interconnected mesoporous V2O5 electrode: impact on lithium ion insertion rate. *Physical Chemistry Chemical Physics* **2016,** *18* (44), 30605-30611.
106. Juran, T. R.; Young, J.; Smeu, M., Density Functional Theory Modeling of MnO2 Polymorphs as Cathodes for Multivalent Ion Batteries. *The Journal of Physical Chemistry C* **2018,** *122* (16), 8788-8795.
107. Ling, C.; Zhang, R.; Arthur, T. S.; Mizuno, F., How General is the Conversion Reaction in Mg Battery Cathode: A Case Study of the Magnesiation of α-MnO2. *Chemistry of Materials* **2015,** *27* (16), 5799-5807.
108. Arthur, T. S.; Zhang, R.; Ling, C.; Glans, P.-A.; Fan, X.; Guo, J.; Mizuno, F., Understanding the Electrochemical Mechanism of K-αMnO2 for Magnesium Battery Cathodes. *ACS Applied Materials & Interfaces* **2014,** *6* (10), 7004-7008.
109. Nam, K. W.; Kim, S.; Lee, S.; Salama, M.; Shterenberg, I.; Gofer, Y.; Kim, J.-S.; Yang, E.; Park, C. S.; Kim, J.-S.; Lee, S.-S.; Chang, W.-S.; S-G., D.; Jo, Y. N.; Jung, Y.; Aurbach, D.; Choi, J. W., The High Performance of Crystal Water Containing Manganese Birnessite Cathodes for Magnesium Batteries. *Nano Letters* **2015,** *15* (6), 4071-4079.
110. Shirley, D. A., High-Resolution X-Ray Photoemission Spectrum of the Valence Bands of Gold. *Phys. Rev. B* **1972,** *5* (12), 4709-4714.
111. Weng, Y.-T.; Pan, H.-A.; Lee, R.-C.; Huang, T.-Y.; Chu, Y.; Lee, J.-F.; Sheu, H.-S.; Wu, N.-L., Spatially Confined MnO2 Nanostructure Enabling Consecutive Reversible Charge Transfer from Mn(IV) to Mn(II) in a Mixed Pseudocapacitor-Battery Electrode. *Advanced Energy Materials* **2015,** *5* (18), 1500772.
112. Nesbitt, H. W.; Banerjee, D., Interpretation of XPS Mn(2p) spectra of Mn oxyhydroxides and constraints on the mechanism of MnO_2 precipitation. *American Mineralogist* **1998,** *83* (3-4), 305-315.
113. Briggs, D.; Beamson, G., XPS studies of the oxygen 1s and 2s levels in a wide range of functional polymers. *Analytical Chemistry* **1993,** *65* (11), 1517-1523.
114. Ramstedt, M.; Shchukarev, A. V.; Sjöberg, S., Characterization of hydrous manganite (γ-MnOOH) surfaces—an XPS study. *Surface and Interface Analysis* **2002,** *34* (1), 632--636.
115. Silversmit, G.; Depla, D.; Poelman, H.; Marin, G. B.; De Gryse, R., Determination of the V2p XPS binding energies for different vanadium oxidation states (V5+ to

V0+). *Journal of Electron Spectroscopy and Related Phenomena* **2004,** *135* (2), 167-175.
116. Chen, W.; Zhan, X.; Luo, B.; Ou, Z.; Shih, P.-C.; Yao, L.; Pidaparthy, S.; Patra, A.; An, H.; Braun, P. V.; Stephens, R. M.; Yang, H.; Zuo, J.-M.; Chen, Q., Effects of Particle Size on Mg2+ Ion Intercalation into λ-MnO2 Cathode Materials. *Nano Letters* **2019,** *19* (7), 4712-4720.
117. De Guzman, R. N.; Awaluddin, A.; Shen, Y.-F.; Tian, Z. R.; Suib, S. L.; Ching, S.; O'Young, C.-L., Electrical Resistivity Measurements on Manganese Oxides with Layer and Tunnel Structures: Birnessites, Todorokites, and Cryptomelanes. *Chemistry of Materials* **1995,** *7* (7), 1286-1292.
118. Mao, L.; Zhang, K.; On Chan, H. S.; Wu, J., Nanostructured MnO2/graphene composites for supercapacitor electrodes: the effect of morphology, crystallinity and composition. *Journal of Materials Chemistry* **2012,** *22* (5), 1845-1851.
119. Kim, N.; Sahadeo, E.; Liu, C.; Rose, O.; Rubloff, G.; Lee, S. B., Impact of pore size, interconnections, and dynamic conductivity on the electrochemistry of vanadium pentoxide in well defined porous structures. *Physical Chemistry Chemical Physics* **2018,** *20* (47), 29708-29716.
120. Bhandari, A.; Bhattacharya, J., Review—Manganese Dissolution from Spinel Cathode: Few Unanswered Questions. *Journal of The Electrochemical Society* **2016,** *164* (2), A106-A127.
121. Liu, R.; Lee, S. B., MnO2/Poly(3,4-ethylenedioxythiophene) Coaxial Nanowires by One-Step Coelectrodeposition for Electrochemical Energy Storage. *Journal of the American Chemical Society* **2008,** *130* (10), 2942-2943.
122. Xiao, R.; Cho, S. I.; Liu, R.; Lee, S. B., Controlled Electrochemical Synthesis of Conductive Polymer Nanotube Structures. *Journal of the American Chemical Society* **2007,** *129* (14), 4483-4489.
123. Ardizzone, S.; Fregonara, G.; Trasatti, S., "Inner" and "outer" active surface of RuO2 electrodes. *Electrochimica Acta* **1990,** *35* (1), 263-267.
124. Wang, J.; Polleux, J.; Lim, J.; Dunn, B., Pseudocapacitive Contributions to Electrochemical Energy Storage in TiO2 (Anatase) Nanoparticles. *The Journal of Physical Chemistry C* **2007,** *111* (40), 14925-14931.
125. Huang, Z.-H.; Song, Y.; Feng, D.-Y.; Sun, Z.; Sun, X.; Liu, X.-X., High Mass Loading MnO2 with Hierarchical Nanostructures for Supercapacitors. *ACS Nano* **2018,** *12* (4), 3557-3567.
126. Gogotsi, Y.; Penner, R. M., Energy Storage in Nanomaterials – Capacitive, Pseudocapacitive, or Battery-like? *ACS Nano* **2018,** *12* (3), 2081-2083.
127. Bard, A. J.; Faulkner, L. R., *Electrochemical Methods: Fundamentals and Applications, 2nd Edition*. Wiley: New York, 2000.
128. Liu, T. C.; Pell, W. G.; Conway, B. E.; Roberson, S. L., Behavior of Molybdenum Nitrides as Materials for Electrochemical Capacitors: Comparison with Ruthenium Oxide. *Journal of The Electrochemical Society* **1998,** *145* (6), 1882-1888.
129. Liu, T.; Dai, A.; Lu, J.; Yuan, Y.; Xiao, Y.; Yu, L.; Li, M.; Gim, J.; Ma, L.; Liu, J.; Zhan, C.; Li, L.; Zheng, J.; Ren, Y.; Wu, T.; Shahbazian-Yassar, R.; Wen, J.; Pan, F.; Amine, K., Correlation between manganese dissolution and dynamic phase

stability in spinel-based lithium-ion battery. *Nature Communications* **2019,** *10* (1), 4721.
130. Wang, Y.; Sahadeo, E.; Rubloff, G.; Lin, C.-F.; Lee, S. B., High-capacity lithium sulfur battery and beyond: a review of metal anode protection layers and perspective of solid-state electrolytes. *Journal of Materials Science* **2019,** *54* (5), 3671-3693.
131. Lin, C.-F.; Qi, Y.; Gregorczyk, K.; Lee, S. B.; Rubloff, G. W., Nanoscale Protection Layers To Mitigate Degradation in High-Energy Electrochemical Energy Storage Systems. *Accounts of Chemical Research* **2018,** *51* (1), 97-106.
132. Luo, W.; Lin, C.-F.; Zhao, O.; Noked, M.; Zhang, Y.; Rubloff, G. W.; Hu, L., Ultrathin Surface Coating Enables the Stable Sodium Metal Anode. *Advanced Energy Materials* **2017,** *7* (2), 1601526--n/a.
133. George, S. M., Atomic Layer Deposition: An Overview. *Chemical Reviews* **2010,** *110* (1), 111-131.
134. Kozen, A. C.; Lin, C.-F.; Pearse, A. J.; Schroeder, M. A.; Han, X.; Hu, L.; Lee, S.-B.; Rubloff, G. W.; Noked, M., Next-Generation Lithium Metal Anode Engineering via Atomic Layer Deposition. *ACS Nano* **2015,** *9* (6), 5884-5892.
135. Chen, T.; Ceder, G.; Sai Gautam, G.; Canepa, P., Evaluation of Mg Compounds as Coating Materials in Mg Batteries. *Frontiers in Chemistry* **2019,** *7*, 24.
136. Chen, T.; Sai Gautam, G.; Canepa, P., Ionic Transport in Potential Coating Materials for Mg Batteries. *Chemistry of Materials* **2019,** *31* (19), 8087-8099.
137. Jay, R.; Tomich, A. W.; Zhang, J.; Zhao, Y.; De Gorostiza, A.; Lavallo, V.; Guo, J., Comparative Study of Mg(CB11H12)2 and Mg(TFSI)2 at the Magnesium/Electrolyte Interface. *ACS Applied Materials & Interfaces* **2019,** *11* (12), 11414-11420.
138. Meng, Z.; Foix, D.; Brun, N.; Dedryvère, R.; Stievano, L.; Morcrette, M.; Berthelot, R., Alloys to Replace Mg Anodes in Efficient and Practical Mg-Ion/Sulfur Batteries. *ACS Energy Letters* **2019,** *4* (9), 2040-2044.
139. Tilinin, I. S., Mean escape depth of signal photoelectrons ejected from solids by polarized x rays. *Physical Review B* **1996,** *53* (2), 547-555.
140. Chen, K.-H.; Wood, K. N.; Kazyak, E.; LePage, W. S.; Davis, A. L.; Sanchez, A. J.; Dasgupta, N. P., Dead lithium: mass transport effects on voltage, capacity, and failure of lithium metal anodes. *Journal of Materials Chemistry A* **2017,** *5* (23), 11671-11681.
141. Muldoon, J.; Bucur, C. B.; Boaretto, N.; Gregory, T.; di Noto, V., Polymers: Opening Doors to Future Batteries. *Polymer Reviews* **2015,** *55* (2), 208-246.
142. Kalhoff, J.; Eshetu, G. G.; Bresser, D.; Passerini, S., Safer Electrolytes for Lithium-Ion Batteries: State of the Art and Perspectives. *ChemSusChem* **2015,** *8* (13), 2154-2175.
143. Cho, Y.-G.; Hwang, C.; Cheong, D. S.; Kim, Y.-S.; Song, H.-K., Gel/Solid Polymer Electrolytes Characterized by In Situ Gelation or Polymerization for Electrochemical Energy Systems. *Advanced Materials* **2019,** *31* (20), 1804909.
144. Zhang, H.; Li, C.; Piszcz, M.; Coya, E.; Rojo, T.; Rodriguez-Martinez, L. M.; Armand, M.; Zhou, Z., Single lithium-ion conducting solid polymer electrolytes: advances and perspectives. *Chemical Society Reviews* **2017,** *46* (3), 797-815.

145. Saha, P.; Datta, M. K.; Velikokhatnyi, O. I.; Manivannan, A.; Alman, D.; Kumta, P. N., Rechargeable magnesium battery: Current status and key challenges for the future. *Progress in Materials Science* **2014,** *66*, 1-86.
146. Deivanayagam, R.; Ingram, B. J.; Shahbazian-Yassar, R., Progress in development of electrolytes for magnesium batteries. *Energy Storage Materials* **2019,** *21*, 136-153.
147. Zhao, Q.; Liu, X.; Stalin, S.; Khan, K.; Archer, L. A., Solid-state polymer electrolytes with in-built fast interfacial transport for secondary lithium batteries. *Nature Energy* **2019,** *4* (5), 365-373.
148. Zhong, H.; Wang, C.; Xu, Z.; Ding, F.; Liu, X., A novel quasi-solid state electrolyte with highly effective polysulfide diffusion inhibition for lithium-sulfur batteries. *Scientific Reports* **2016,** *6* (1), 25484.
149. Liu, F.-Q.; Wang, W.-P.; Yin, Y.-X.; Zhang, S.-F.; Shi, J.-L.; Wang, L.; Zhang, X.-D.; Zheng, Y.; Zhou, J.-J.; Li, L.; Guo, Y.-G., Upgrading traditional liquid electrolyte via in situ gelation for future lithium metal batteries. *Science Advances* **2018,** *4* (10), eaat5383.
150. Aurbach, D.; Gizbar, H.; Schechter, A.; Chusid, O.; Gottlieb, H. E.; Gofer, Y.; Goldberg, I., Electrolyte Solutions for Rechargeable Magnesium Batteries Based on Organomagnesium Chloroaluminate Complexes. *Journal of The Electrochemical Society* **2002,** *149* (2), A115-A121.
151. Bevilacqua, S. C.; Pham, K. H.; See, K. A., Effect of the Electrolyte Solvent on Redox Processes in Mg–S Batteries. *Inorganic Chemistry* **2019,** *58* (16), 10472-10482.
152. Salama, M.; Attias, R.; Hirsch, B.; Yemini, R.; Gofer, Y.; Noked, M.; Aurbach, D., On the Feasibility of Practical Mg–S Batteries: Practical Limitations Associated with Metallic Magnesium Anodes. *ACS Applied Materials & Interfaces* **2018,** *10* (43), 36910-36917.
153. Antoniotti, S.; Dalla, V.; Duñach, E., Metal Triflimidates: Better than Metal Triflates as Catalysts in Organic Synthesis—The Effect of a Highly Delocalized Counteranion. *Angewandte Chemie International Edition* **2010,** *49* (43), 7860-7888.
154. Gal, J.-F.; Iacobucci, C.; Monfardini, I.; Massi, L.; Duñach, E.; Olivero, S., Metal triflates and triflimides as Lewis "superacids": preparation, synthetic application and affinity tests by mass spectrometry. *Journal of Physical Organic Chemistry* **2013,** *26* (2), 87-97.
155. Greb, L., Lewis Superacids: Classifications, Candidates, and Applications. *Chemistry* **2018,** *24*.
156. Qiu, H.; Yang, Z.; Köhler, M.; Ling, J.; Schacher, F. H., Synthesis and Solution Self-Assembly of Poly(1,3-dioxolane). *Macromolecules* **2019,** *52* (9), 3359-3366.
157. Riddlestone, I. M.; Kraft, A.; Schaefer, J.; Krossing, I., Taming the Cationic Beast: Novel Developments in the Synthesis and Application of Weakly Coordinating Anions. *Angewandte Chemie International Edition* **2018,** *57* (43), 13982-14024.
158. Sa, N.; Pan, B.; Saha-Shah, A.; Hubaud, A. A.; Vaughey, J. T.; Baker, L. A.; Liao, C.; Burrell, A. K., Role of Chloride for a Simple, Non-Grignard Mg Electrolyte in Ether-Based Solvents. *ACS Applied Materials & Interfaces* **2016,** *8* (25), 16002-16008.

159. Salama, M.; Shterenberg, I.; Gizbar, H.; Eliaz, N. N.; Kosa, M.; Keinan-Adamsky, K.; Afri, M.; Shimon, L. J. W.; Gottlieb, H. E.; Major, D. T.; Gofer, Y.; Aurbach, D., Unique Behavior of Dimethoxyethane (DME)/Mg(N(SO2CF3)2)2 Solutions. *The Journal of Physical Chemistry C* **2016,** *120* (35), 19586-19594.